University of Strathclyde

Institute of Photonics

Diamond and GaN Waveguides and Microstructures for Integrated Quantum Photonics

by

Yanfeng Zhang

A thesis presented in fulfilment of the requirements for the degree of Doctor of Philosophy in Physics at the University of Strathclyde in Glasgow

2012

Frontispiece

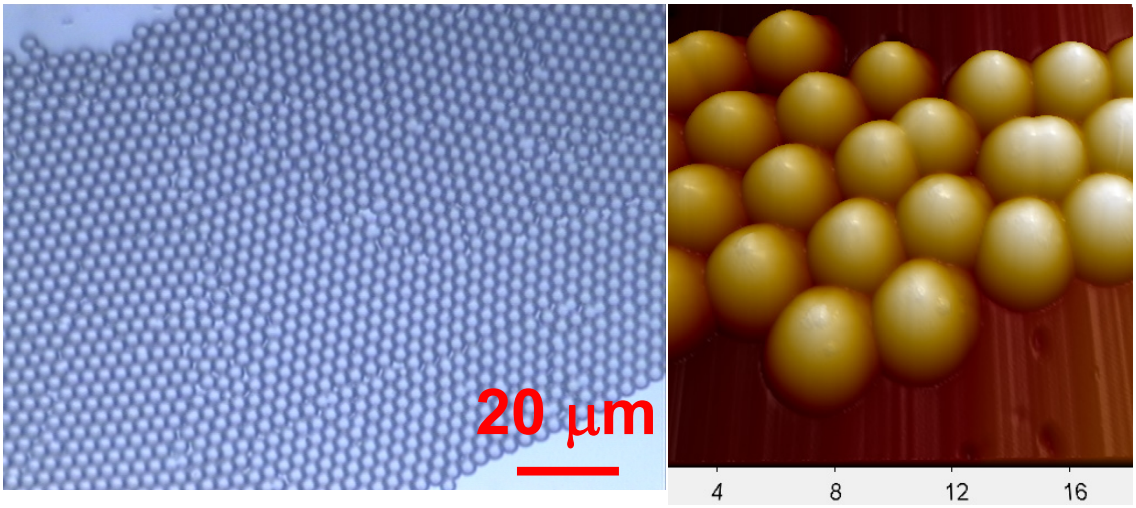

Diamond microlens arrays were fabricated by etching SiO_2 microspheres.

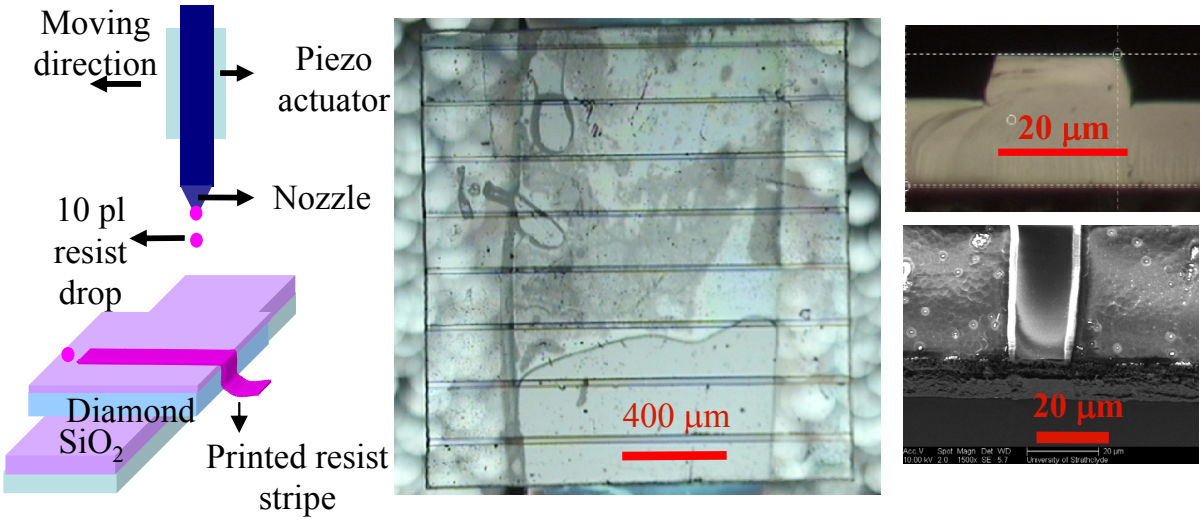

Edge coupled diamond large cross section rib waveguides were fabricated by inkjet printing photoresist and photolithography.

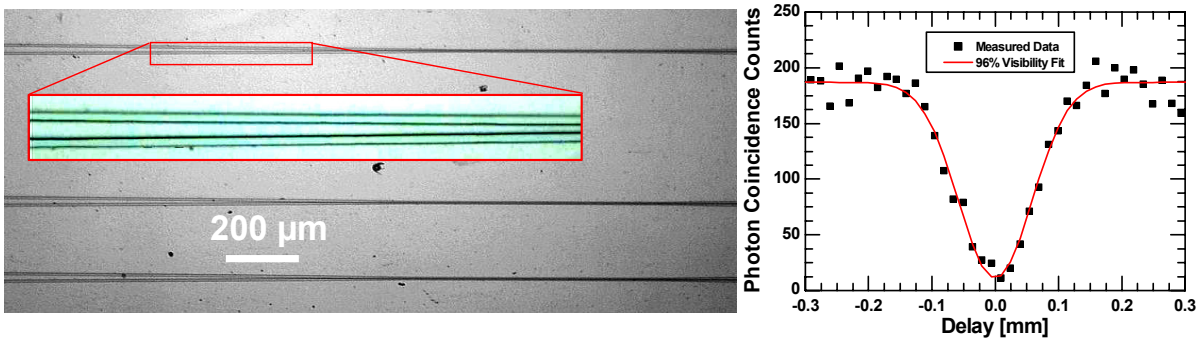

GaN directional couplers were fabricated and Hong-Ou-Mandel two-photon interference was demonstrated with a visibility of 96%.

Copyright statement

Signed: Date:

Acknowledgments

This thesis is the outcome of years of research that has been done since I joined Prof. Martin. D. Dawson's group in the Institute of Photonics, University of Strathclyde. It is a huge pleasure to express my thanks to the people who helped a lot in the completion of this thesis. Without them, this thesis would not have been possible.

First of all, I would like to thank my supervisor, Dr. Erdan Gu. He interviewed me in Beijing in March 2008 and has helped me ever since with literally everything from visa application, literature reading, experiment design to paper/thesis writing. I particularly thank him for his enormous patience and encouragement throughout my PhD study.

I gratefully acknowledge Prof. Martin D. Dawson for all his guidance and support for my research. It was him who saw the great potential of diamond and GaN waveguides for integrated quantum photonics and encouraged me to choose this direction. I'm very grateful that I followed his passion on this amazing topic.

I want to thank my collaborators. First are Dr. Stephane Calvez and Loyd J. McKnight. Their expertise on waveguide design and characterization was been my strongest backup in the last few years. Dr. Ian M. Watson provided GaN sample growth. Dr. Paul Edwards and Prof. Rob Martin kindly allowed me to use the SEM in the Physics department. Dr. Min Wu taught me the use of inkjet printer. Dr. Benoit Guilhabert helped on the μLED writing. I also want to thank Erman Engin, Dr. Martin J. Cryan, Dr. Mark G. Thompson and Prof. Jeremy L. OBrien for the two-photon interference measurement on the GaN directional coupler undertaken at the University of Bristol.

I want to thank all the people I worked with in the clean-room. Jim Sweeney for his management and maintenance of the clean-room; Dr. Chang Xiong and Dr. Zheng Gong who gave me the initial training and patient guidance; Dr. Zhizhong Chen for teaching many aspects of research and technology; Enyuan Xie, Lei Wang, Ningyang Liu, Yuebin Tao, Pengfei Tian and Dr. David Massoubre for being there when I needed to work overtime.

I want to thank Paul Hynd, Sharon Kelly, Lisa Flanagan and Sharon Vetter for accompanying me in my best Scottish summer rowing on the river Clyde, Shuailong Zhang, Hainan Xie and IKEA friends for many happy memories of hiking in Scotland.

I had a great time in Glasgow, I would like to thank all the people I met, in particularly those I'm not afraid to ask for help and happy to talk to:

> Lynda McLaughlin, Tim Holt, Alan Kemp, Nicolas Laurand, Jennifer Hastie, Ewan Mulhern, Alicja Zarowna, Jonathan McKendry, Rolf Birch, Johannes Herrnsdorf, Peter Roth, Peter Schlosser, Caroline Mullenbroich.

I want to thank all the greatest minds in history, you made physics such an amazing subject and led to the modern development of the computer and Internet which made knowledge widely accessible.

At the end, but by no means the least, I want to thank my parents, sisters, brothers, and cousins in Pingxiang, Hebei province, China. I know most of you won't read my thesis, still I am sorry that I can't name you all here. You are the ones who gave me the encouragement and support since I can remember. You fed me when I was little, borrowed/bought books for me when I was eager to read, supported me emotionally and financially when I was in need. Without you, I would not be the person I am today, not to mention writing this thesis.

I still have one person I'm in debt to, Yujie Chen, who is my colleague, classmate, roommate, best friend, husband and best find in this world.

Abstract

Quantum optics has been a frontier of physics in the last few decades. Integrated quantum photonics which prompts the concept of realizing quantum optics operation on a chip is crucial for any potential applications beyond the optical bench. This thesis focuses on two important material systems (diamond and GaN) which both have the potential for integration of single photon sources and detectors with integrated quantum circuits and at the same time can minimize the footprint of the integrated quantum circuits due to their high refractive index.

We have proposed and realized two new masking methods to fabricating higher aspect ratio diamond microlenses through plasma etching. We have also proposed and demonstrated a new approach to fabricating large cross-section edge-coupled rib waveguides on free-standing thin diamond substrates by combining inkjet printing of photoresist with photolithographic patterning technique. Single-mode GaN directional couplers with transmission varying between 0.1:0.9 and 0.55:0.45 have been studied and two-photon interference was demonstrated in a 0.55:0.45 GaN directional coupler. This is the first demonstration of two-photon interference realized on a compound semiconductor chip.

Our work opens up a new way to achieve sophisticated integrated quantum photonic circuits based on GaN and other suitable compound semiconductors. Integrated quantum photonics is a widespread research topic, currently undergoing explosive developments. Future options including an all-diamond platform, III-V semiconductors or a hybrid system between diamond and III-V semiconductors are discussed as perspectives.

Contents

Copyright i

Acknowledgments ii

Abstract iv

Table of Contents v

List of Figures viii

List of Tables xiv

1 Introduction 1

1.1 Quantum optics: a brief history 2

1.2 Single photon sources 4

1.2.1 What is a single photon? 4

1.2.2 How to produce a single photons? 6

1.3 Integrated quantum circuits 12

1.3.1 History of integrated optics 13

1.3.2 Development of integrated quantum circuits 14

1.4 Single photon detectors 16

1.5 Outline of this thesis 17

2 Fabrication techniques for developing photonic microstructures 19

2.1 Pattern definition 19

2.1.1 Photolithography 19

2.1.2 Maskless pattern writing 30

2.2 Pattern transfer 35

2.2.1 Dry etching 36

2.2.2 Wet etching 39

2.3 Summary 40

3 Diamond microstructures: microlenses and micropillars 41
3.1 Overview of diamond material 42
3.1.1 Natural diamond 42
3.1.2 Synthesis diamond 42
3.2 Background on diamond lenses 43
3.2.1 History of diamond lenses 44
3.2.2 Physics of diamond lenses 46
3.3 Diamond microlens fabrication and dual-mask method 50
3.3.1 Photoresist reflow/etching to make microlenses 50
3.3.2 Dual-mask method 54
3.4 Diamond microlens array 58
3.4.1 SiO_2 microsphere deposition 58
3.4.2 ICP Ar/Cl_2 plasma etching 59
3.5 Diamond micropillars 61
3.5.1 Estimated light extraction efficiency using FDTD 62
3.5.2 Fabrication of diamond micropillars 62
3.6 Summary 64

4 Diamond waveguides 65
4.1 Diamond photonic structures 65
4.1.1 Literature review 66
4.1.2 Diamond rib waveguide design 71
4.2 Microcrystalline diamond waveguide 73
4.2.1 Fabrication process 73
4.2.2 Challenges and issues using conventional process 74
4.3 Fabrication of single crystalline diamond waveguides 77
4.3.1 Photoresist deposition using an inkjet printer 78
4.3.2 Diamond waveguide fabrication 79
4.4 Optical characterization of the waveguides 81
4.4.1 Optical characterization setup 81
4.4.2 Optical characterization result 83
4.5 Conclusion 83

5 GaN waveguides and directional couplers 85
5.1 GaN material growth 86
5.1.1 MOCVD 86
5.1.2 GaN growth 86
5.1.3 The Aixtron 200/4 RF-S MOCVD reactor 87

5.2 Review of GaN waveguide structures . . . 89
5.3 GaN rib waveguides . . . 89
5.3.1 Design details . . . 89
5.3.2 Waveguide fabrication . . . 91
5.3.3 Characterization . . . 92
5.4 GaN directional couplers . . . 93
5.4.1 Design and optimization . . . 94
5.4.2 Fabrication and structural inspection . . . 96
5.4.3 Optical characterization . . . 98
5.4.4 Two-photon interference in GaN DCs . . . 98
5.5 Conclusion . . . 100

6 Summary and perspectives **101**
6.1 Summary . . . 101
6.2 Future works . . . 102
6.2.1 All-diamond platform . . . 102
6.2.2 A III-V semiconductor platform . . . 103
6.2.3 A hybrid integrated quantum circuit . . . 103
6.3 Final remark . . . 103

Bibliography **105**

Publications **136**

List of Figures

1.1 Google books' Ngram view result of 'quantum optics' from 1900 to 2008. 2
1.2 Schematic illustration of a linear optics quantum computation circuit. 4
1.3 Probability distribution of the number of photons for three sources [(a) thermal source; (b) Coherent source and (c) Single photon source] with an average photon number $n = 1$. 5
1.4 Schematic diagram of Hanbury-Brown−Twiss (HBT) experimental setup. 5
1.5 Illustration of photon streams for (a) bunched light, (b) coherent light and (c) antibunched light. 6
1.6 (a) A custom built scanning confocal microscope; (b) Structure diagram of a NV single; (c) A 1x1 μ m image showing fluorescence from a single NV centre in diamond. Images courtesy: Jason Smith. 8
1.7 Illustration of the 'photon splitting' process when a pump photon goes through a nonlinear crystal. 10
1.8 (a) Schematic setup and (b) photograph of type-I SPDC. 10
1.9 (a) Schematic setup and (b) photograph of type-II SPDC taken by Michael Reck. 11
1.10 Schematic of two photons meeting at a beam splitter. 12
1.11 Illustration of (a) fibre, (b) planar, (c) channel and (d) rib waveguides. 14

2.1 Illustration of photolithography and the difference between positive and negative resists. 20
2.2 Image of a Karl Suss MA 6 Mask Aligner used for the work of this thesis. 21
2.3 Emission spectrum of a Mercury high pressure short-arc lamp. . . 22
2.4 Diagram of the chemical reaction of a typical positive resist DNQ in the exposure and development process. 23

2.5 Illustration of chemical reaction of a typical negative resist in the exposure process: (a) photon reaction; (b) crosslinking process. . . 24
2.6 Absorption spectrum of positive resist S1813 and negative resist maN-1400. 25
2.7 Spin speed curves of photoresists used in this work (a) S1800 series and maN-1400 series; (b) SPR220 series with different wafer sizes and a image of spin coater inset. Data is extracted from SHIPLEY and Micro Resist technology GmbH. Image courtesy: Ian W. Watson. 26
2.8 Illustration of (a) edge bead formation and influence on contact lithography without edge bead (b) and with edge bead (c). 27
2.9 (a) Edge bead size measurement from the literature; (b) spin coated photoresist and (c) exposed/developed photoresist pattern on a 4-mm diamond disk. 28
2.10 Exposed pattern of small sample with severe edge bead with inset is an optical microscopy image of 3 mm × 3 mm square diamond sample with spin-coated resist: (a) mask pattern; and (b) exposed resist pattern. 29
2.11 (a) Image and (b) schematic of a home-built CMOS-driven μLED wrting setup. 30
2.12 The spectrum overlap between emission of μLED (blue) and absorption of photoresist (orange). 31
2.13 Image of the inkjet printer with insets showing a cartridge installed in the printer (top) and an unused one (bottom). 32
2.14 Stroboscopic images of single photoresist droplet formation taken from the drop watch window. 33
2.15 Print patterns of photoresist with different drop distance of (a) 50 μm and (b) 30 μm. 33
2.16 (a) Diagram of contact angles and optical sideview images of 1 μl photoresist S1805 droplets on as-grown (b) and silane-treated (c) PECVD SiO_2 34
2.17 Optical images and the corresponding stylus profilemeter measurements of photoresist S1805 stripes printed on (a) an as-grown and (b) silane-treated SiO_2 surfaces. 35
2.18 (a) Diagram and (b) Image of an RIE chamber. Process chamber is highlighted in blue circle. Image courtesy: Ian W. Watson. . . . 36

2.19 (a) Schematic diagram and (b) image of ICP chamber. Process chamber is highlighted in yellow circle. Image courtesy: Ian W. Watson. 37
2.20 Schematics of the two basic plasma etching processes: (a) physical sputtering; and (b) chemical etching. 38
2.21 Image of wet bench in cleanroom. Image courtesy: Ian W. Watson. 39

3.1 Illustration of total reflection between the interface of diamond and air (a) flat surface and (b) with a diamond hemispherical lens. . . 46
3.2 Diagram of a diamond NV center inside a diamond hemispherical lens with arbitrary position. 47
3.3 Numerical calculations of diamond NV emission pattern with six different position inside a hemispherical lens; diamond NV centre coordinates are displayed in subplot (a-f). Blue rays are total reflections where $\delta > 24.6^o$. Red rays are emission in the top cone where $\phi > 0^o$. Yellow rays are emissions in the bottom cone where $\phi < 0^o$. 48
3.4 Diamond microlens fabrication process. 51
3.5 Etching rate of diamond (red curve) and the etching selectivity between diamond and photoresist SPR220 7.0 (blue curve) vs ICP coil power. Other parameters are platen power: 300 W; gas pressure: 5 mTorr; Ar/O_2 gas flows:15/40 sccm 52
3.6 SEM images of diamond lenses with two different magnifications. 53
3.7 Optical microscopy images of photoresist lenses with thicker initial resist layer. 53
3.8 Surface profile of two photoresist microlenses with thicker initial resist layer. 54
3.9 Dual-mask diamond microlens fabrication process. 55
3.10 Calculated profiles of reflowed resist lens, SiO_2 lens and diamond lens. 56
3.11 Optical microscopy images of SiO_2 lenses at different fabrication stages: (a) Photoresist after thermal reflow; (b-c-d) 10-20-30 min after ICP etching. 56
3.12 (a) Optical mircoscopy and (b) SEM images of diamond microlenses after being transfered from SiO_2 microlenses. 57
3.13 Optical microscopy image of monodispersed 3 μm SiO_2 microspheres. 59
3.14 Diamond microlenses transferred from 3 μm SiO_2 microspheres. . 60

3.15 (a) AFM image of a diamond microlens array transferred from 3 μm SiO_2 microspheres and (b) a line scan profile along the blue dash line in (a) 61
3.16 (a) Diagram of a diamond micropillar and (b) Light exaction efficiency vs. diameter and height of diamond pillars by 2D FDTD method. 62
3.17 (a) Optical microscopy images of μLED written photoresist dots with exposure time ranges from 0.6 s to 2 s and (b) the enlarged image of a group of four photoresist dots using 4 μLEDs under 0.6 s exposure. 63
3.18 μLED written photoresist dots: average diameter vs exposure time. The error bars are shown in the figure. 64

4.1 Process flow of diamond membrane made by ion implantation. . . 67
4.2 Process flow of diamond membrane made by ion implantation and post CVD diamond growth. 67
4.3 Diamond waveguide design schematic. Parameters of a, b and r are used in Equation 4.1. λ is the free space wavelength of light. n_0, n_1 and n_2 are refractive indices of air, diamond and silica, respectively. 72
4.4 FEA simulation of large cross-section diamond rib waveguide . . . 72
4.5 Fabrication process of microcrystalline diamond rib waveguides. . 73
4.6 Images of microcrystalline diamond rib waveguides during the fabrication process. (a) photolithographic resist lines on SiO_2/diamond/SiO_2/Si, (b) SiO_2 lines on diamond/SiO_2/Si after RIE etching and residual resist stripping with an enlarged image as inset, and (c) microcrystalline diamond lines on diamond/SiO_2/Si after ICP etching with an enlarged image inset. 75
4.7 SEM images of microcrystalline diamond rib waveguides after the fabrication process: (a) small and (b) large magnifications. 75
4.8 SEM images of single crystalline diamond rib waveguides after the fabrication process: (a) small and (b) large magnifications. 76
4.9 SEM images showing edge effect for single crystal thin plate diamond rib waveguides. 76
4.10 The fabrication process flow of the thin (20 μm) diamond waveguides. 77
4.11 A schematic diagram of the inkjet printing setup. The piezo actuator controlled inkjet printing nozzle generated 10-pl resist drops one by one to form a continuous stripe on the PECVD grown SiO_2 mask. 78

4.12 The surface profilometer measurements of the cross-section of four samples with 1 to 4 layers of printing photoresist. 79
4.13 Optical microscopy plan-view pictures of (a) the printed resist stripes and (b) the corresponding photolithographic resist lines. . 80
4.14 Optical microscopy plan-view pictures of diamond waveguide fabrication after (a) RIE and (b) ICP etching. 80
4.15 (a) Surface profile of fabricated diamond waveguide and inset is a SEM image of the resulted sample. (b) A high magnification SEM image of diamond rib waveguide highlighted the etching trench. . 81
4.16 Diamond waveguide samples on Al slide (edge view). Two samples are highlighted in red circles in the image. 81
4.17 A schematic diagram of the diamond waveguide light coupling setup. 82
4.18 Photograph of the waveguide coupling setup. The sample holder with the diamond waveguide sample is highlighted in the yellow circle. 82
4.19 Light intensity of the output profile of (a) the guided fundamental mode in the diamond rib waveguides, and (b) the unguided planar mode from the diamond slab. The white line shows the ideal structural outline of the diamond waveguide. 83

5.1 Image of the AIX 200/4 RF-S MOCVD system. Image courtesy: Ian W. Watson. 88
5.2 Schematic modular representation of the AIX 200/4 RF-S MOCVD reactor. 88
5.3 Schematic of rib waveguide design using GaN on sapphire with air cladding. The ordinary index of GaN is used due to the restriction to TE operation. 89
5.4 Process flow of the GaN rib waveguide fabrication. 91
5.5 Optical images of the output facet (a) without and (b) with an overlay of the measured intensity profile (using false colour) of the guided mode. 92
5.6 Measured F-P fringe and fitted data of GaN rib waveguide. 93
5.7 Plan view BPM simulation of GaN DC design with a 2-μm gap . 94
5.8 Device length optimization when changing rib width in the coupling region. It shows the minimum device length required to connect a 3.8-μm wide rib waveguide to the coupling region with a rib width between 1.4 and 2.6 μm for a 0.05 dB taper loss. 95

5.9 (a) Optical plan view micrograph of GaN DCs with (inset) high magnification image of coupling region; (b) optical image of cleaved GaN DC facet. 96
5.10 Oblique SEM image of cleaved facet with (inset) inferred facet etch profile. 97
5.11 SEM plan view image of coupling region. Black regions indicate the waveguides. The coupler gap and waveguide sidewalls are clearly visible. 97
5.12 Optical setup for GaN DC measurement. 97
5.13 Measured transmission for fabricated GaN DCs with varying coupling length. The curve is a BPM simulation of the transmission using the parameters shown in Fig. 5.7(c) at a wavelength of 800 nm. 98
5.14 The setup of Hong-Ou-Mandel quantum interference 99
5.15 The Hong-Ou-Mandel dip observed for a 45:55 GaN rib waveguide DC, the signature of quantum interference between two degenerate photons. The fitted visibility is 96%. 99

List of Tables

1.1 List of reported integrated quantum photonic circuits in the literature. 15

2.1 Wavelength of light sources for optical lithography and the corresponding resolution and DOF. 23
2.2 Viscosity of applied photoresists (Unit: mPa·s) 25
2.3 Etching gases of commonly used materials in this thesis 39

3.1 List of reported diamond lens in literature. 45
3.2 Total extraction efficiency of 6 typical NV centre positions. 49
3.3 PECVD recipe for SiO_2 deposition. 55
3.4 ICP etching recipe for SiO_2 microlens fabrication. 55
3.5 ICP etching recipe for diamond microlens fabrication using SiO_2 microspheres. 60

4.1 Summary of changing refractive index of diamond by ion implantation. 66
4.2 Summary of photonic structures made on diamond membrane ion implantation. 68
4.3 Summary of photonic structures on thin diamond membrane made by ion implantation and CVD diamond post growth. 69
4.4 Summary of photonic structures on commercial thin diamond platelet. 70
4.5 Summary of photonic structures made by 3D FIB milling and heteroepitaxial growth. 71
4.6 RIE recipe for SiO_2 etching and etching rate of SiO_2/S1805. . . . 74
4.7 ICP recipe for diamond rib waveguide and etching rate of diamond/SiO_2 74

5.1 Summary of GaN waveguides in literature. 90
5.2 ICP recipe for GaN etching and etching rate of GaN and SiO_2. . . 92

Chapter 1

Introduction

This work focuses on the development of novel micro-photonic structures and components such as microlenses and waveguides for integrated quantum photonics. With the application of integrated quantum photonics in mind, these structures and components were made from diamond and GaN materials. A basic understanding of integrated quantum photonics is crucial for designing and achieving such photonic components. In this chapter, I will give a brief introduction to this topic and provide an overview of building integrated waveguide circuits on different substrates.

Quantum optics will be reviewed very briefly in section 1.1 of this chapter. The understanding of light as a 'quanta' leads not only to the development of the theory of quantum mechanics, but also to potential applications like quantum computation. One particularly interesting protocol for quantum computation is linear optical quantum computing which involves only single photon sources, linear photonic circuits and single photon detectors [1].

In section 1.2, I will introduce the concept of the single photon and review the literature on various single photon sources. The integration potential and performance of single photon sources are also commented on briefly.

It is difficult or even impossible to build complex photonic circuits by using bulk optical components, so the developments of miniature and integrated circuits are needed. In section 1.3, the history and development of integrated optics will be reviewed, followed by a summary of recent reports on integrated quantum photonic circuits. A short introduction on single photon detectors will be presented in section 1.4.

In section 1.5 of this chapter, I will describe why we need to search for new material systems (e.g. diamond and GaN in this work) to develop integrated quantum photonics rather than to stick to the conventional silica-based materials.

Finally, I will give the outline of this thesis.

1.1 Quantum optics: a brief history

Quantum optics is a relatively new subject. Figure 1.1 is the Google books' Ngram viewer result of a 2-gram phrase *quantum optics* during 1900-2008 [2]. This graph shows how the phrase *quantum optics* has occurred in a corpus of books. As we can see, this clearly shows the historical development trend of quantum optics. Its appearance has gradually increased during the second half of the 20th century.

A few remarkable papers paved the way of quantum optics. It was Max Planck who first had the quantum hypothesis in 1900 in order to explain the black-body radiation and this gave birth to quantum theory [3, 4]. In 1905, Albert Einstein proposed that light can be considered as particles, and offered a successful explanation of the photoelectric effect observed by Heinrich Hertz and Philipp Lenard [5].

As Mark Fox pointed out in his introductory book on quantum optics [6], Planck and Einstein pioneered the quantum theories of light and atoms, but there is no direct experimental evidence of the quantum nature of light. Einstein made a prediction that the maximum energy of the electrons emitted in the photoelectric effect must vary linearly with the frequency of the incident light. This prediction was confirmed experimentally to high precision ten years later by Millikan [7]. This is one of the most convincing confirmations of the idea of quanta [8]. In 1923, Arthur Holly Compton observed an effect in which the scattered radiation from a high energy photon colliding with a target has a wavelength shift which

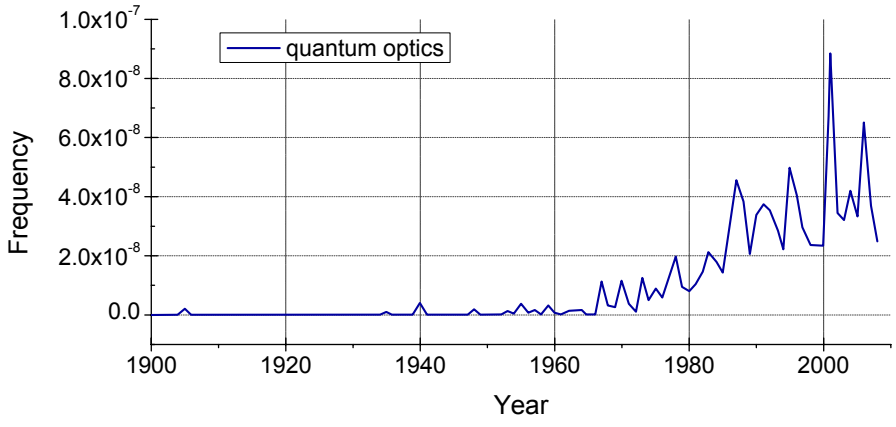

Figure 1.1: Google books' Ngram view result of 'quantum optics' from 1900 to 2008.

also confirmed the quantum nature of light [9].

Later on, more modern experiments have been carried out in quantum optics. In 1956, Robert Hanbury-Brown and Richard Q. Twiss published their experimental results on the intensity interferometer [10]. They discovered photon bunching in light emitted from a filtered Hg arc lamp and this experiment opened up the development of modern quantum optics. In 1960, the laser was invented [11] and it later became an important tool for quantum optics. In 1963, Roy J. Glauber gave a description of quantum states of light which have different statistical properties compared to those of classical light [12, 13]. Photon antibunching was demonstrated in an experiment by H. Jeff Kimble, Mario Dagenais, and Leonard Mandel in 1977 [14]. The antibunching experiment provides direct evidence for the existence of optical photons. In 1987, Chung Ki Hong, Zhe-Yu Jeff Ou and Leonard Mandel reported a two-photon interference experiment [15].

The development of quantum computing as a subsection of quantum optics starts in 1982 when Richard Feynman first came up with the idea of a 'quantum computer' [16]. David Deutsch published his seminal paper on the universal quantum computer in 1985 [17]. Peter Shor then proposed an algorithm of discrete logarithms and factoring for quantum computation [18]. Another famous algorithm was proposed by Lov K. Grover [19, 20]. A review of quantum algorithms can be found in papers [21, 22].

Motivated by these promising algorithms, several groups around the world have been racing to create a practical quantum computer. Isaac L. Chuang *et al.* reported an experimental realization of a Deutsch-Jozsa quantum algorithm using a nuclear magnetic resonance (NMR) technique in 1998 [23]. In the same year, Jonathan A. Jones *et al.* reported the implementation of Grover's quantum search algorithm on an NMR quantum computer [24]. Since then, quantum computers have been tested on several systems including photons, NMR, trapped atoms, quantum dots and dopants in solids, superconductors, and others [25].

Among these, photons are particularly appealing for quantum computing especially after the breakthrough made by Emanuel Knill, Raymond Laflamme and Gerard J. Milburn [1]. The Knill-Laflamme-Milburn (KLM) scheme shows that efficient linear optics quantum computation (LOQC) is possible using only beam splitters, phase shifters, single photon sources and photodetectors. These basic components (single photon sources, linear optical networks and photodetectors) of the KLM protocol are readily accessible for experimental investigation and practical realizations have been demonstrated [26–28].

Figure 1.2 shows a brief scheme of LOQC. Prior to 2008, optical quantum

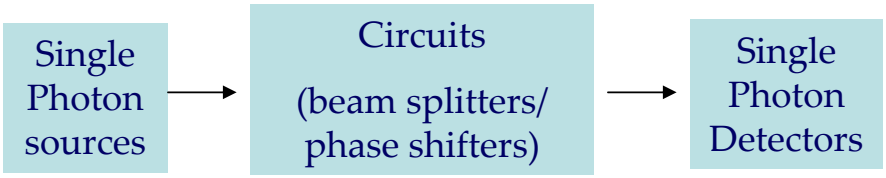

Figure 1.2: Schematic illustration of a linear optics quantum computation circuit.

computing structures comprised bulk optical components, leading to severe limitations in miniaturization, scalability and stability. In the following section, I will review the recent developments towards integrated quantum photonics in the sequence of single photon sources, linear photonic circuits and single photon detectors.

1.2 Single photon sources

A single photon source is a crucial part of LOQC as shown in the previous section. It is also an essential element for quantum cryptography [29]. In this section, I will look back into the literature and present my understanding of single photon sources from the points of view of what is a single photon and how to produce single photons.

1.2.1 What is a single photon?

The term 'single photon' refers to isolated single light quanta. A single photon source emits one photon at a time and thus has a non-classical distribution. The probability distributions of the number of photons for three light sources, i.e. a thermal source, a coherent light source and a single photon source are shown in Figure 1.3. The average number of photons in these modes is one. The thermal source shown in Figure 1.3(a) presents the Bose-Einstein statistics of black-body radiation. The coherent light source in Figure 1.3(b) presents a Poisson distribution, narrower than that of a thermal source. The probability distribution of an ideal single photon source is shown in Figure 1.3(c).

The photon statistics of a light source can be studied via the normalized second-order correlation function $g^{(2)}(\tau)$ [30]. This can be defined by:

$$g^{(2)}(\tau) = \frac{< I(t)I(t+\tau) >}{< I(t) >< I(t+\tau) >} \tag{1.1}$$

where $\langle I(t) \rangle$ indicates that the time averaged light intensity is computed by in-

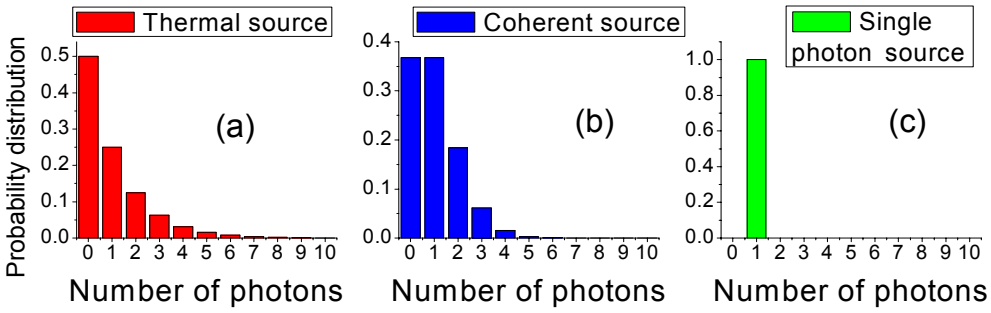

Figure 1.3: Probability distribution of the number of photons for three sources [(a) thermal source; (b) Coherent source and (c) Single photon source] with an average photon number $n = 1$.

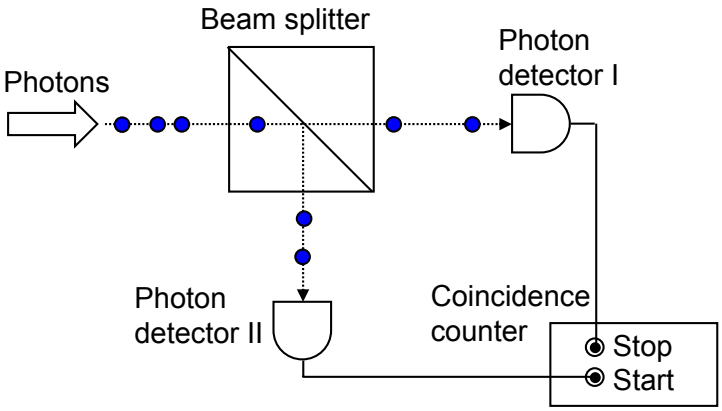

Figure 1.4: Schematic diagram of Hanbury-Brown−Twiss (HBT) experimental setup.

tegrating over a long time period. The formula shows the existence of the next photon coming after the time delay τ. For zero time delay, the function $g^{(2)}(0)$ means how much coincidence of two photons occurs. Different light sources will have different $g^{(2)}(0)$.

Second-order correlation function can be measured by the famous Hanbury-Brown−Twiss (HBT) experiment [14]. The HBT setup is shown in Figure 1.4. A photon stream is incident on a beam splitter and the outputs from the two photon detectors are feed into a coincidence counter.

Based on the value of $g^{(2)}(0)$, a threefold classification is made. When $g^{(2)}(0) > 1$, we use the phrase *bunched* light. As illustrated in Figure 1.5(a), there is an enhanced probability of two photons being emitted within a short time delay. When $g^{(2)}(0) = 1$, we use the phrase *coherent* light, in which the photons are mostly random distributed, as illustrated in Figure 1.5(b). When $g^{(2)}(0) < 1$, we use the term *antibunched* light, as illustrated in Figure 1.5(c), where photon number is regularly distributed.

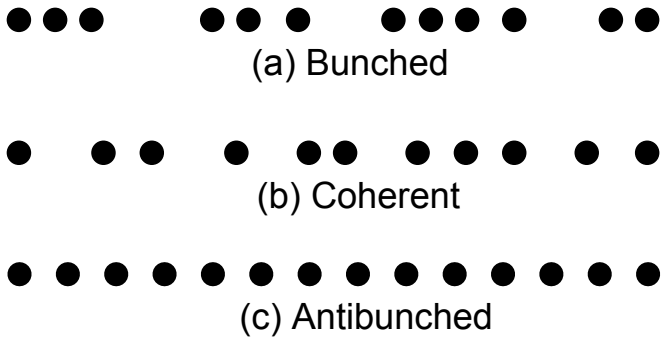

Figure 1.5: Illustration of photon streams for (a) bunched light, (b) coherent light and (c) antibunched light.

1.2.2 How to produce a single photons?

Reference [31] is a recent review paper on single photon sources (quantum emitters) by M. D. Eisaman *et al.*. The first antibunching single photon source was an sodium atom from a report in 1977 by H. Jeff Kimble, Mario Dagenais, and Leonard Mandel [14]. Since then, a variety of single quantum emitters have been used for single photon generation. The resonance fluorescence of a single atomic ion stored in a radio-frequency trap was found to be antibunching in 1987 by Frank Diedrich and Herbert Walther [32]. Fluorescence photons emitted by an optically pumped single molecule of pentacene in a *p*-terphenyl host showed antibunching [33]. These single photon sources are normally operated at low temperature and are thus very bulky. Achieving a compact solid state single photon source is quite demanding. Quantum dots (QDs) and impurities/defects in solid are both atom-like and have been proposed as solid-state single photon sources. In the next two subsections, we give a brief introduction on these two single photon sources.

Quantum dots

The idea to use solid-state QD for single photon generation was proposed as early as 1994 by Atac Imamoglu and Yoshihisa Yamamoto [34]. A review paper on QDs as a single photon source can be found in reference [35]. In general, there are three different types of QDs used for single photon generation, namely colloidal QDs (synthesized from solution based precursor compounds), self-assembled QDs (grown using molecularbeam epitaxy(MBE) or metal organic chemical vapor deposition (MOCVD)) and lithographically defined QDs (plasma etching to two-dimensional semiconductor layers through lithographic defined masks).

Colloidal QDs can be synthesized by high-temperature organometallic methods [36, 37]. The first quantum dot (QDs) antibunching experiment was reported by Peter Michler *et al.* from Atac Imamoglu's group [38]. In that experiment, CdSe/ZnS core/shell colloidal QDs were used. Recent advances on single photon sources based on single colloidal nanocrystals can be found in a review paper [39].

Photon antibunching of self-assembly QDs was reported by Atac Imamoglu's group in 2000 [40], C. Becher *et.al.* in 2001 [41] and Yoshihisa Yamamoto's group in 2001 [42].

In 2011, photon antibunching from a single lithographically defined InGaAs/GaAs quantum dot was demonstrated by Varun Verma *et al.* in National Institute of Standards and Technology, USA [43]. This method could provide a way of positioning the QD emitters accurately.

The QDs mentioned above are all optically pumped. In 2002, Zhiliang Yuan *et al.* at the Toshiba Research Europe Limited, Cambridge Research Laboratory reported single photon emission from a single quantum dot within the intrinsic region of an electrically driven $p-i-n$ junction [44]. Such a device provides advantages for single photon source on chip integration.

QDs have also been tested through two photon quantum interference. Charles Santori *et al.* tested the indistinguishability of photons emitted by a semiconductor quantum dot in a microcavity through a Hong-Ou-Mandel type two-photon interference experiment and confirmed that photons emitted from QDs are identical [45]. The use of QDs for photon pair generation was reported by the Toshiba Cambridge research laboratory in 2006 [46] and was further improved in terms of brightness [47].

Because QDs are artificial atoms which are not identical in practice, they show different emission wavelengths. Quantum interference between photons emitted by different QDs is hard to realize and limiting the application of QDs. However, progress has been made in recent years. Post-selective two-photon interference from two spots of an electrical pumped single photon LED has been studied by Andrew J. Shield's group in 2008 [48]. Yoshihisa Yamamoto's group reported their experiments on the indistinguishable photons from independent semiconductor nanostructures which were ZnSe/ZnMgSe quantum wells (QWs) with a fluorine donor [49]. Interference of single photons from two separate low density strain-induced InAs QDs has been reported by Glenn S. Solomon's group in 2010 [50].

One of our motivations for working on GaN as a platform for integrated quantum photonics is the potential to integrate a GaN QD single photon source on chip. GaN QDs were demonstrated to be able to emit single photons at 200 K by

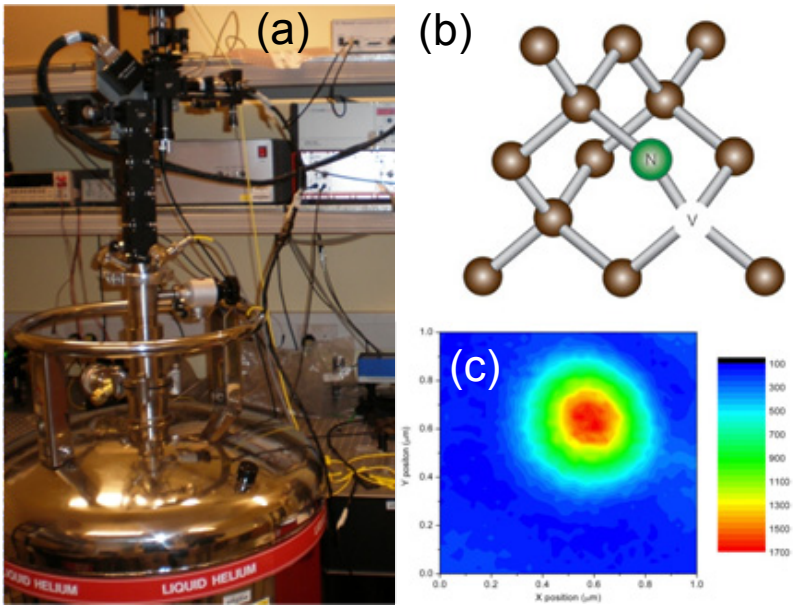

Figure 1.6: (a) A custom built scanning confocal microscope; (b) Structure diagram of a NV single; (c) A 1x1 μ m image showing fluorescence from a single NV centre in diamond. Images courtesy: Jason Smith.

Satoshi Kako *et al.* in 2006 [51]. A summary of Nitride-based quantum dots for single photon source applications can be found in the Jarjour review paper [52]. Recently, progress has been made to achieve an electrically driven single photon source based on GaN QDs [53].

Although impressive progress have been made on single photon generation from QDs, the operation of such QDs sources often requires low temperature which is a major drawback. This makes the diamond colour (NV) centre quite promising because it can be operated at room temperature.

Diamond colour centre

Diamond has more than 500 types of luminescent centre and there are numerous reports of single photon emission from nitrogen-vacancy (NV) centres, nickel-related colour centres, silicon-related colour centres, chromium-related colour centres, etc. Diamond-based single photon emitters from different colour centres and microfabrication techniques are summarized in a recent review article from Igor Aharonovich *et al.* [54].

NV centre is one of the most intensively studied colour centres in diamond. Figure 1.6 shows a example of scanning cofocal microscope, atom structure diagram and fluorescence of a single NV center. Single photon emission has been observed from both bulk and nanocrystalline diamond. Philippe Grangier's group

reported that photon antibunching in 2-MeV electron irradiated single crystals of synthetic **Ib** diamond from Drukker International [55]. In the same year, Harald Weinfurter's group also observed that fluorescence light, emitted from a single nitrogen-vacancy centre in a type **Ib** untreated diamond crystal, exhibits strong photon antibunching [56]. In 2001, Philippe Grangier's group reported photon antibunching phenomena in diamond nanocrystals with a typical size of 40 nm containing a single NV centre [57].

Single photon generation from diamond colour centres is an active research area and great progress has been made on electrical pumping and fine tuning. In 2011, a diamond-based light-emitting diode for visible single-photon emission at room temperature was reported [58]. Similar to QDs, the drawback of diamond colour centres is that they are not identical. Interference between the photons from two diamond colour centres is very hard to achieve despite much effort. Recently, two groups have just reported their two-photon quantum interference between two separated diamond colour centres [59] and even from two remote diamond samples [60]. This major breakthrough makes diamond even more attractive as a quantum photonics platform.

Parametric down conversion

Since the above mentioned single photon sources are not yet readily available, a spontaneous parametric down conversion (SPDC) source is so far the most used photon source in quantum optics experiments. In this work, we used SPDC to generate photon pairs for two-photon quantum interference in our GaN directional couplers as shown in Chapter 5. Thus, the background and principle of SPDC are presented in this subsection.

It is noted that William Henry Louisell, Amnon Yariv and Anthony E. Siegman predicted SPDC in 1961 [61]. Then, Boris Ya. Zel'dovich and David Nikolaevich Klyshko proposed SPDC could be used as nonclassical light [62]. A SPDC experiment was demonstrated by David C. Burnham and Donald L. Weinberg in 1970 [63]. SPDC is a second order nonlinear process [64] as illustrated in Figure 1.7. A pump photon is converted into two down-converted photons named the signal photon and the idler photon. When applying energy and momentum conservation laws, we have:

$$\omega_{pump} = \omega_{signal} + \omega_{idler} \tag{1.2}$$

$$k_{pump} = k_{signal} + k_{idler} \tag{1.3}$$

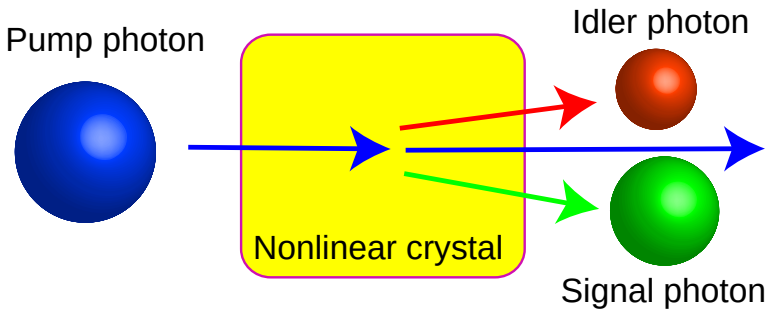

Figure 1.7: Illustration of the 'photon splitting' process when a pump photon goes through a nonlinear crystal.

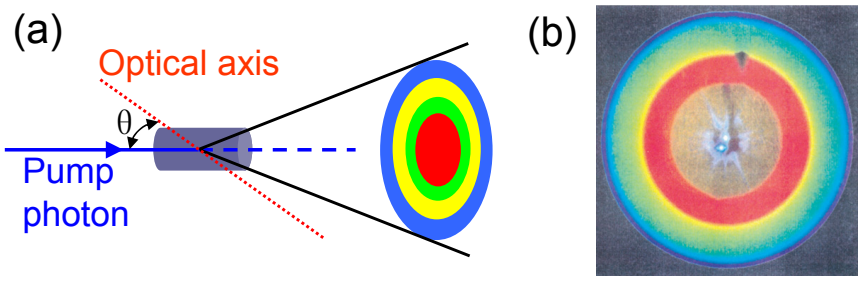

Figure 1.8: (a) Schematic setup and (b) photograph of type-I SPDC. After [65].

where, ω represents angular frequency and k is the wave vector of pump/signal/idler photon. If $\omega_{signal} = \omega_{idler} = 0.5\omega_{pump}$ the process is said to be degenerate, and nondegenerate otherwise.

Satisfying these two equations at the same time is called phase matching. There are multiple solutions of frequencies and wave vectors that can be phase matched. Dispersion in a nonlinear crystal (i.e. refractive index varies with the frequency) makes it not possible to satisfy phase matching under the normal conditions.

One method to compensate this dispersion is by utilizing a birefringent crystal. Birefringence occurs in uniaxial crystals in which light with different polarizations has different refractive indices. The ordinary refractive index, n_e, is obtained for light polarized along the crystalline optic axis direction and the extraordinary refractive index, n_o, refers to light polarized perpendicular to the optic axis direction. Birefringence and dispersion cancel each other out and allow two different types of phase matching.

In type-I phase matching, two down-converted photons have parallel polarization and are orthogonal to that of the pump photon. Down-converted photons form a cone of multi-spectral light as shown in Figure 1.8.

In type-II phase matching, two down-converted photons have orthogonal po-

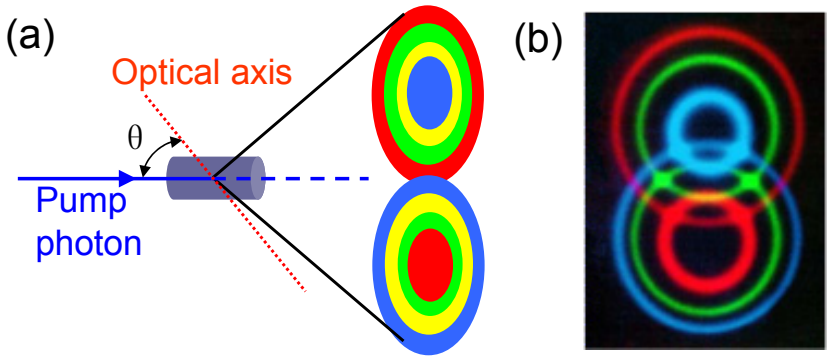

Figure 1.9: (a) Schematic setup and (b) photograph of type-II SPDC taken by Michael Reck. After [67].

larizations and one of them is parallel to the polarization of the pump photon. The two down converted photons are in two cones as shown in Figure 1.9 [67].

Such birefringent optical materials used for SPDC include potassium dideuterium phosphate (KDP, KD_2PO_4), Beta barium borate (BBO, β-BaB_2O_4), Lithium Niobate ($LiNbO_3$), *etc.* David N. Nikogosyan recently summarized the development of various nonlinear crystals in his book [69]. Among all these nonlinear crystals, BBO is now widely used for SPDC and was first synthesized by Chuangtian Chen in 1985 [70]. Early nonlinear applications of BBO crystal were summarized in a review paper in 1991 [71]. In our work undertaken in collaboration with the University of Bristol, a type-I BBO crystal was used to generate photon pairs for two-photon interference measurements.

Besides using birefringent materials for phase matching, there is another technique named quasi-phase matching. Quasi-phase matching was first propsoed 50 years ago by J. A. Armstrong and Nicolaas Bloembergen *et al.* [72]. Implementation of quasi-phase matching requires a fabrication method that can achieve uniform microscale periodic structures while preserving the material's transparency, nonlinearity, and power handling capability [73].

Fabrication methods of periodic nonlinear crystals for quasi-phase matching have been developed including chemical diffusion [74], guided-wave quasi phase matching [75], crystal growth processes [76, 77], orientation-patterned gallium arsenide [78–80] and ferroelectric domain reversal by an external electric field [81]. Periodically poled $LiNbO_3$ (PPLN) has been used as an integrated PPLN SPDC photon pairs source and in waveguide circuits for quantum interference [82] and quantum walks [83]. Furthermore, counterpropagating twin photons generated by a pump beam impinging on top of a nonlinear waveguide have also been used for a two-photon interference demonstration [84–86].

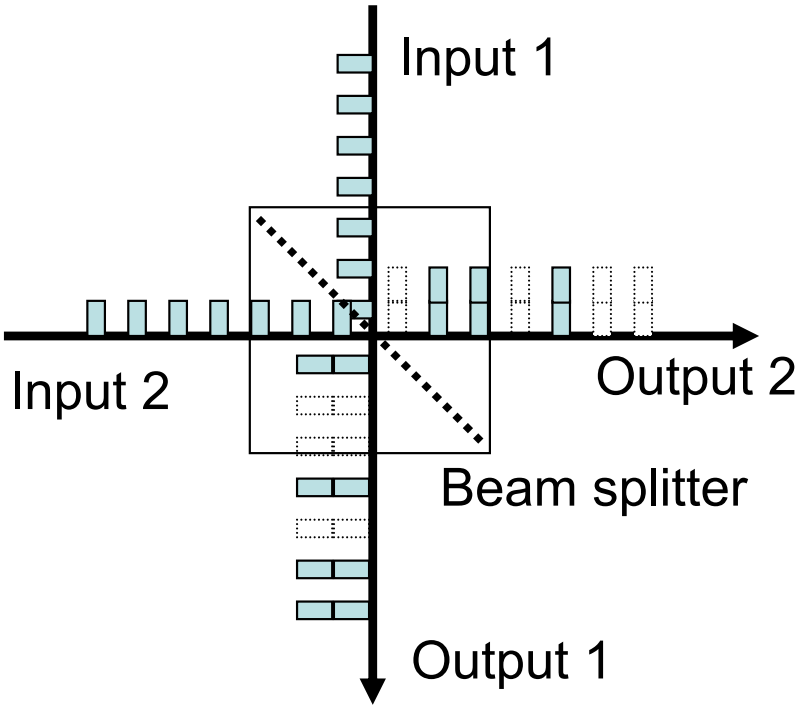

Figure 1.10: Schematic of two photons meeting at a beam splitter. After [87].

1.3 Integrated quantum circuits

Quantum gates, such as the Controlled NOT (CNOT) gate, can be constructed with conventional linear optics using two-photon interference [15]. As shown in Figure 1.10, two photons impinging on a beam splitter via input1/2 may leave the beam splitter with three possibilities:

(1) One photon from output 1, One photon from output 2;

(2) Two photon from output 1, none from output 2;

(3) none from output 1, Two photon from output 2.

This can be written in the form [88]:

$$|\psi\rangle = (|R|^2 - |T|^2)|1\rangle_1|1\rangle_2 + \sqrt{2}i[|2\rangle_1|0\rangle_2 + |0\rangle_1|2\rangle_2] \tag{1.4}$$

where R and T are respectively the reflectivity and transmissivity of the beam splitter. For a 50/50 beam splitter, the first term is zero. This implies that indistinguishable photons will 'stick together' and leave the beam splitter through the same output.

Bulk optical components are widely used in quantum optics experiments and hence easily take up a large optical table. The applications of integrated optics components to replace these bulk optical components has opened up the age of

chip-based optical quantum computation, namely integrated quantum circuits. In this section, I will review the history of integrated optics first then go on to the recent development of integrated quantum photonic circuits.

1.3.1 History of integrated optics

The classical theory to treat light waveguiding uses total internal reflection (TIR). TIR occurs when light propagates in a medium of higher refractive index than its surroundings, thus light can be confined in the higher index medium. Light guiding in a water jet was demonstrate by Jean-Daniel Colladon in 1842 [89, 90], which is a vivid demonstration showing the light waveguiding effect.

Integrated optics emerged in the 1960s [91–93] and the word "integrated optics" was coined by Stewart E. Miller in 1969 [94]. In his paper, Miller proposed that optical wave circuits could be fabricated in dielectric thin films. Compared to the configuration with freely propagating light beams, integrated optical circuits are small, stable and reproducible. The resulting light confinement in these integrated circuits could facilitate the achievement of desirable nonlinear effects at lower power levels [94]. This seminal paper had been cited 136 times from 1969 to 1976 [95] indicating the fast development of integrated optics during the 1970s, given that there were no computer and internet search engines during that time. The first meeting on integrated optics was held in Las Vegas between 7-10 February, 1972. In that conference, fibre optics together with thin film material related integrated optics were discussed [96]. Since then, much progress has been made in this area and several types of waveguide structures of the integrated optics family were demonstrated in a wide variety of materials, from glass to crystals and semiconductors as shown in Figures 1.11(a-d). Optical fibres are now well developed and have wide applications forming a well-separated subject. 2D/3D waveguides and various functional devices combining several waveguides together have been demonstrated in lithium niobate, indium phosphide, gallium arsenide, silica on silicon, polymer, silicon, etc [97]. One of the key techniques for integrated optics is to manipulate the refractive indices of materials in order to fabricate optical components, for example, waveguides. There are various ways of making waveguides [97]. Thin film technology including the combination of film growth, selective etching and regrowth processes is arguably the most important method. For example, there is a large refractive index contrast between the compound semiconductor films grown with different compositions or SiO_2 films with different dopants. Other material refractive index modification methods include ion diffusion [98], ion exchange [99], ion implantation [100] and laser writing

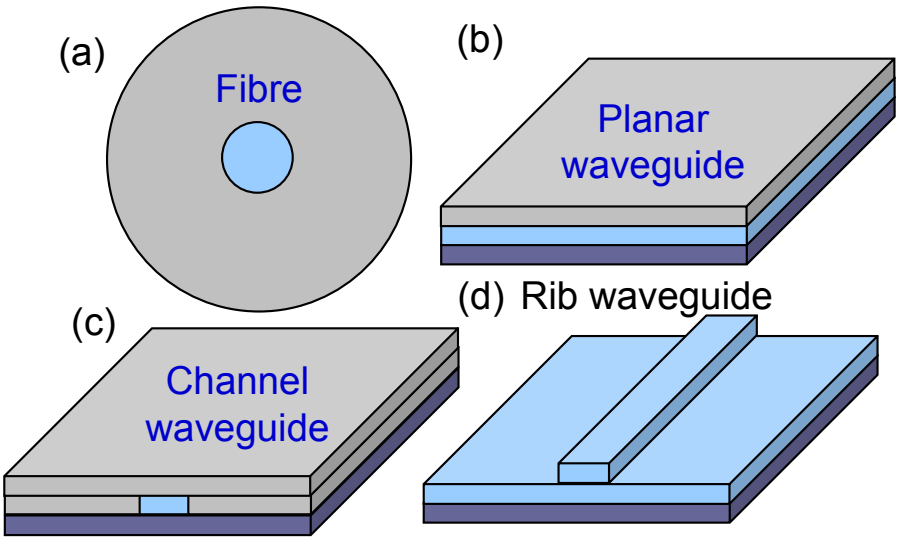

Figure 1.11: Illustration of (a) fibre, (b) planar, (c) channel and (d) rib waveguides.

[101, 102].

This work will concentrate on rib waveguides [Figures 1.11(d)] and associated directional couplers. Rib waveguides on barium silicate glass were first reported by J. E. Goell in 1973 [103]. The advantages of this rib structure are the relaxed requirement for resolution and edge smoothness in the fabrication process since only a portion of the guided energy touches the etched sidewall. A directional coupler consisting of a rib waveguide is reported in the same paper [103]. The principle of a directional coupler is that modes in close proximity waveguides could be coupled by their evanescent fields. Thus a directional coupler can be used to replace the beam splitter which is widely used in traditional optics laboratories. These integrated optical components could help minimize the size of quantum circuits and their application in quantum circuits will be summarized in the next subsection.

1.3.2 Development of integrated quantum circuits

The ability to manipulate nonclassical light on a chip was first demonstrated by Jeremy O'Brien's group at the University of Bristol in 2008 [104]. Since then, several other groups have set out to develop integrated quantum photonic circuits. Table 3.1 summarizes a list of reported work on integrated quantum photonic circuits from 2008 to 2012.

Progress in this area is very encouraging; however, it is still far away from a full integration of single photon sources, circuits and detectors. So far, most

Table 1.1: List of reported integrated quantum photonic circuits in the literature.

Year	Groups	Institution	Material systems	Fabrication techniques	Devices and references
2008-2012	J. L. O'Brien	University of Bristol	CVD-grown silica with different dopant	Channel waveguides patterned by photolithography	MZI and CNOT gate [104], NOON gate [105], MMI [106], reconfigurable gates [107]
2009	G. D. Marshall	Macquarie University	High purity fused silica glass	Femtosecond laser direct writing	Directional couplers [108, 109]
2009	I. A. Walmsley	University of Oxford	CVD-grown silica with different dopant	244 nm UV laser direct writing	X-couplers MZI [110, 111]
2009-2011	P. Mataloni	Sapienza Universit di Roma	Borosilicate glass	Femtosecond laser direct writing	Directional couplers [112], CNOT gate [113], waveguide array [114]
2010	J. L. O'Brien	University of Bristol	PECVD grown SiO_xN_y on thermal SiO_2	Photolithography and RIE	Array of continuously evanescently coupled waveguides [115]
2011	A. White	University of Queensland	High purity fused silica glass	Femtosecond laser direct writing	3D elliptic waveguide arrays for quantum walk [116]
2011	J. L. O'Brien	University of Bristol	Lithium niobate	Titanium diffusion	MZI [117]
2011	M. D. Dawson	University of Strathclyde	GaN on sapphire	Rib waveguide defined by photolithography and dry etching	Directional coupler [118]
2012	J. L. O'Brien	University of Bristol	SOI substrate	Channel waveguide defined by lithography and dry etching	MMI and MZI [119]
2012	S. Tanzilli	Laboratoire de Physique de la Matire Condense	Lithium niobate	Channel waveguide integrated on periodically poled lithium niobate	Quantum relay chip [120]

reported integrated quantum photonic circuits are based on different types of silica with a minor refractive index change. This leads to the large footprint per logic gate (e.g. 1 cm per logic gate for a current silica waveguide circuit [104]). The circuit size can be reduced using photonic materials with a higher refractive index contrast [25]. There has been a preprint on photonic circuits for quantum computation on SOI substrate in February, 2012 from the group at University of Bristol [119]. This is one of our motivations of working on diamond- and/or GaN-based platform, both of which have a high refractive index (both n$\sim$ 2.4 at visible wavelength).

1.4 Single photon detectors

An ideal single photon detector would have high detection efficiency, low dark-count rate, and minimum dead time and timing jitter. If we categorise photon detectors according to their material systems, there are three main types, photomultiplier tubes (PMTs), single photon avalanche photodiodes (SPADs), and superconducting single photon detectors [31].

The PMT is so far the most used photon-counting technology. A PMT is a vacuum device combining two physics effects, the photoelectric effect [121] and secondary electron emission [122]. In a PMT, first an incident photon knocks an electron out of a photocathode made of a low work function material. Then the electron is multiplied by a cascade of secondary electron emission from dynodes, resulting in a current large enough to be detected. Single photon counting in PMTs was demonstrated as early as 1949 by a research group in RCA [123]. Commercial PMT units are now widely available and there are continued efforts to improve the performance of PMT devices [124]. The drawback of the PMT is the high cost of operation (cooling of the photocathode). Furthermore, a PMT is a vacuum tube, which makes it difficult to integrate a PMT with other components to realize integrated quantum photonics.

A SPAD is a semiconductor-based photodetector (photodiode). In a SPAD, an incident photon creates an electron-hole pair instead of an electron as in the case of PMT. The electron-hole pair will then be accelerated in a strong electrical field and then an avalanche process occurs. Many semiconductor materials have been used for making SPADs with different specifications. For example, a silicon SPAD can work in the visible and near-infrared regions, while a Ge-based SPAD can detect photons with a wavelength up to 1.7 μm. InGaAs together with InP can operate in the wavelength range between 0.9 and 1.7 μm. GaN SPADs can

operate in the UV region. The SPAD is now widely used in quantum optics and quantum information experiments [124].

Recent development of single photon detectors such as superconducting nanowire single photon detectors (SNSPDs) [125] and transition-edge sensors [126] are also very promising and might have the potential of integration with semiconductor photonic circuits to make an all integrated quantum photonic circuits.

1.5 Outline of this thesis

So far, I have reviewed the topics of integrated quantum photonics relevant to this thesis. Integrated quantum photonics is still in its infancy and the material choice is still widely open. In this work, we have investigated the high refractive index materials (Diamond and GaN) that are suitable for developing quantum circuits with small footprints. The objective of this thesis work is to develop novel diamond- and GaN-based photonic micro-structures and components including diamond micro-lenses and micro-pillars, diamond and GaN rib waveguides and GaN directional couplers, which could be the building blocks of new and/or hybrid integrated quantum photonic circuits.

To fabricate these novel photonic structures, semiconductor fabrication technology was used and further technology development was also carried out. Chapter 2 is a general overview of the semiconductor fabrication processes including pattern definition and pattern transfer. Less common fabrication methods like inkjet printing for photoresist deposition and μLED writing are also introduced because they were also used in this work.

Chapters 3 and 4 present investigations and results on diamond photonic structures. As mentioned above, diamond is a promising material candidate for making a room temperature solid-state single photon source. However, as diamond has a refractive index of 2.4, the collection efficiency of single photon emission from a planar diamond is quite low. Many efforts have been made in developing diamond microlenses, nanowires and photonic crystals so as to improve light extraction. I will present my work on the fabrication of diamond microlenses and micropillars in Chapter 3.

The use of diamond as a platform for quantum photonics has been proposed. However, as diamond is very hard and chemically inert, the processing of diamond to make waveguides and other photonic structures is very challenging despite much related effort. In this work, I have made progress on fabricating end-

coupled diamond rib waveguides and these diamond waveguides were also fully characterised [127]. These results will be presented in Chapter 4.

The results on GaN rib waveguides and directional couplers are presented in Chapter 5. We first proposed and demonstrated GaN-based structures as being attractive for such photonic applications. GaN has a high refractive index which enables compact photonic circuits. It also benefits from mature, versatile and scalable epitaxial technology which makes the GaN material readily accessible.

Finally, Chapter 6 will give a summary of this thesis and discuss some perspectives of future research on this topic of integrated quantum photonics.

Chapter 2

Fabrication techniques for developing photonic microstructures

The task of this research was to develop the desired photonic structures such as microlenses, micropillars and rib waveguides in diamond and GaN. In this chapter, the microfabrication techniques will be reviewed and commented on, especially those techniques applied in this work. There are two main sections in this chapter: pattern definition and pattern transfer.

2.1 Pattern definition

In microfabrication, a number of templates or masks are often needed in order to make micro-patterns and thereafter transfer the pattern to a substrate. There are various ways of making transferable patterns on a substrate, such as photolithography, laser/μLED writing, e-beam writing, focused ion beam (FIB), inkjet printing and dip-pen writing. In the following section, photolithography is introduced first since it is commonly used in microfabrication processes. Two maskless patterning methods (μLED writing and photoresist inkjet printing) are introduced in the second subsection.

2.1.1 Photolithography

Traditional lithography is a method that uses masks (patterns on a flat surface like stone, polymer, wax, metal, etc.) to create replicas of these patterns on the mask or their complementary patterns by applying ink on a sheet of paper

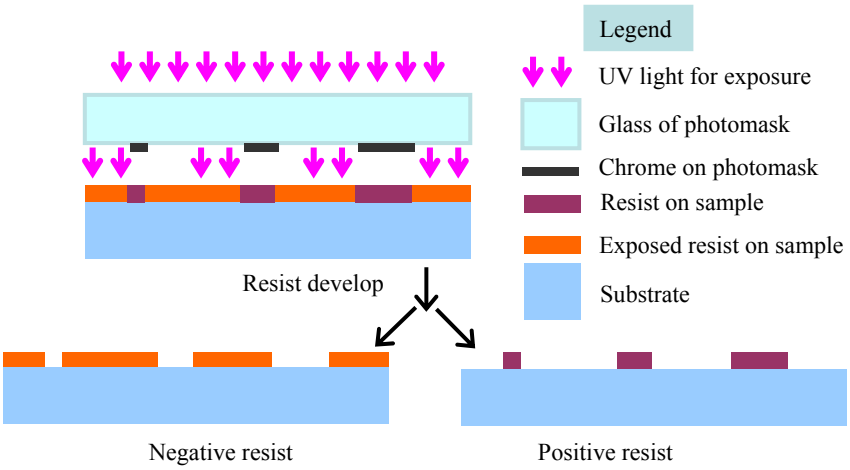

Figure 2.1: Illustration of photolithography and the difference between positive and negative resists.

or cloth. In the modern semiconductor industry, a widely used technique is named photolithography which usually involves the use of a photo-mask (Chrome pattern on glass) and an ink (photoresist). Unlike the replication process in the traditional lithography methods, the photo-mask pattern is there replicated into the photoresist by light exposure. Exposure refers to the process that a light beam reaches the surface of the photoresist and a chemical reaction occurs. A subsequent development process will then remove the undesired material and realise the replicated or complementary pattern of the photomask.

Photolithography developed along with the integrated circuit (IC) industry. The basic process of photolithography is shown in Figure 2.1. A light beam shines through a photomask and causes a reaction in the photoresist film. Depending on the properties of the photoresist, the developed resist pattern will be either the replica of the photomask (positive resist) or the complementary pattern to the photomask (negative resist). In this photolithography section, I shall first give a brief introduction on the mask aligner used for photolithography, and then move on to the resolution achieved in the last several decades. Finally, the many aspects of photoresists will be introduced including the absorption spectrum and advantages and disadvantages of the photoresist spin coating process.

Mask aligner

In this work, the photolithography process has been conducted on a Karl Suss MA6 Mask Aligner (Figure 2.2) in our laboratories. A typical mask aligner consists of three main parts: lamp housing, alignment stage and microscope. The lamp housing accommodates the exposure light source, including the high pres-

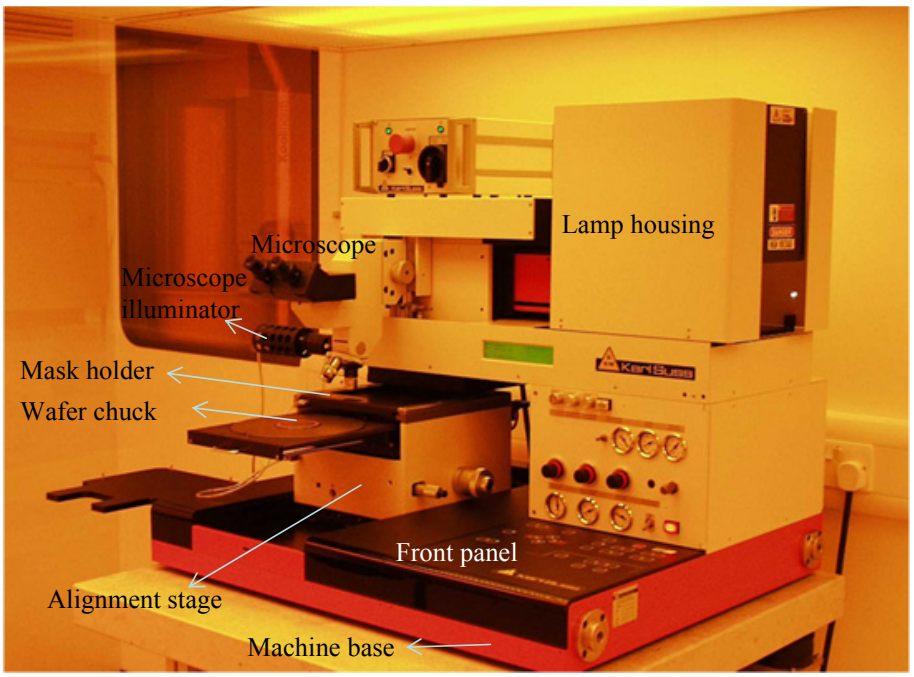

Figure 2.2: Image of a Karl Suss MA 6 Mask Aligner used for the work of this thesis.

sure mercury arc lamp and corresponding electrical circuit which will be explained in detail in the following paragraph. The microscope is indicated in Figure 2.2 and is mainly used for observing and achieving the alignment between the photomask and the sample before the exposure. The wafer chuck and mask holder are also shown in the same figure. During the alignment, there is a certain gap (i.e. 50 μm, depending individual setup) between the mask and wafer, allowing the x-y and angle adjustments.

There are three different exposure modes: soft contact, hard contact and vacuum contact. Among these exposure modes, vacuum contact has the minimum possible gap and gives best resolution, while soft contact gives the worst. However, in soft contact mode, a gentle pressure is applied thus giving a better protection for both the sample and mask. To get better balance between safety and resolution, a standard hard contact mode is usually recommended.

In our MA6 mask aligner, the lamp housing model is UV400. It consists of an HBO®350 W/S Mercury high pressure short-arc lamp and the emission wavelength is mainly between 350 and 450 nm. Figure 2.3 is an emission spectrum of a typical Mercury high pressure short arc lamp. HBO is from the Germany system of nomenclature used to identify different kind of mercury lamps. 'H' represents 'Hg (Mercury)', 'B' represents 'quartz short-arc' and 'O' means 'optical projection'.

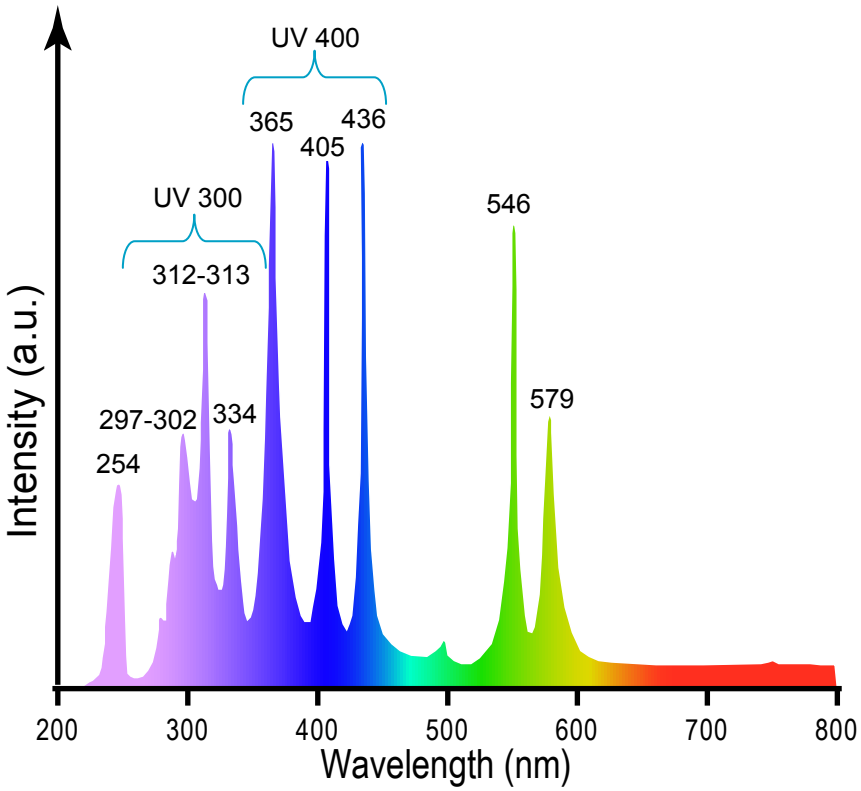

Figure 2.3: Emission spectrum of a Mercury high pressure short-arc lamp.

Resolution

The ideal resolution (R) and depth of focus (DOF) of an optical system is determined by the Rayleigh criterion:

$$R = k_1 \frac{\lambda}{NA} \tag{2.1}$$

$$DOF = k_2 \frac{\lambda}{(NA)^2} \tag{2.2}$$

When the numerical aperture (NA) is high enough,

$$DOF = k_3 \frac{\lambda}{2(1 - \sqrt{1 - (NA)^2})} \tag{2.3}$$

where the numerical aperture $NA = nsin\theta$ and the factors k_1, k_2 and k_3 are process-dependent constants. From this formula, we can see that in order to decrease the feature size, we need to reduce the wavelength and increase the numerical aperture. Table 2.1 shows the wavelength of light sources for optical lithography and the corresponding resolution and DOF. The light sources used

Table 2.1: Wavelength of light sources for optical lithography and the corresponding resolution and DOF. k_1=0.3 and k_3=1 for R and DOF calculations. Assuming NA=0.9 for all wavelengths except extreme ultraviolet (EUV), for which NA=0.25. After [130].

light source	$\lambda(nm)$	R (nm)	DOF (nm)
Hg arc lamp (g-line)	436	145	386
Hg arc lamp (i-line)	365	122	324
KrF	248.3	83	220
ArF	193.4	64	171
F_2	157.6	53	140
EUV	13.5	16	213

for high resolution optical lithography have evolved from the Hg arc lamp (typical wavelength: 436, 365 and 248 nm) to an excimer laser (typical wavelength 193 nm). As a result, the resolution has been improved dramatically (for example, down to 45 nm in *Intel Co.* [128]). So far, the world's smallest dense patterning with 16 nm resolution is achieved by the SEMATECH Berkeley Microfield Exposure Tool (MET) in February 2010 [129].

Photoresist types

There are two basic types of photoresists, namely positive and negative photoresists and the differences between them are illustrated in Figure 2.1.

A typical positive resist is based on Diazoquinones (DQ) or Diazonaphthoquinone (DNQ). When exposed to specific light (UV usually), its nitrogen bond will be broken so as to form an unstable molecule. In the developer solution, an OH group will attach to the molecule and form an acid and eventually be dissolved into the developer. This chemical reaction is shown in Figure 2.4.

Figure 2.5 shows the crosslinking process of a typical two-component negative resist. During exposure, the sensitizer bisazide reacts with photons and produces nitrine and nitrogen as shown in Figure 2.5(a), forming polymer linkages as in

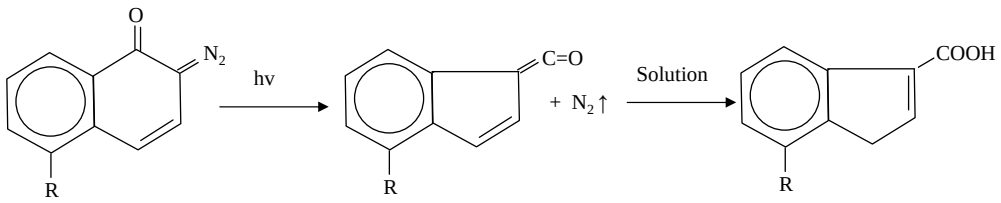

Figure 2.4: Diagram of the chemical reaction of a typical positive resist DNQ in the exposure and development process.

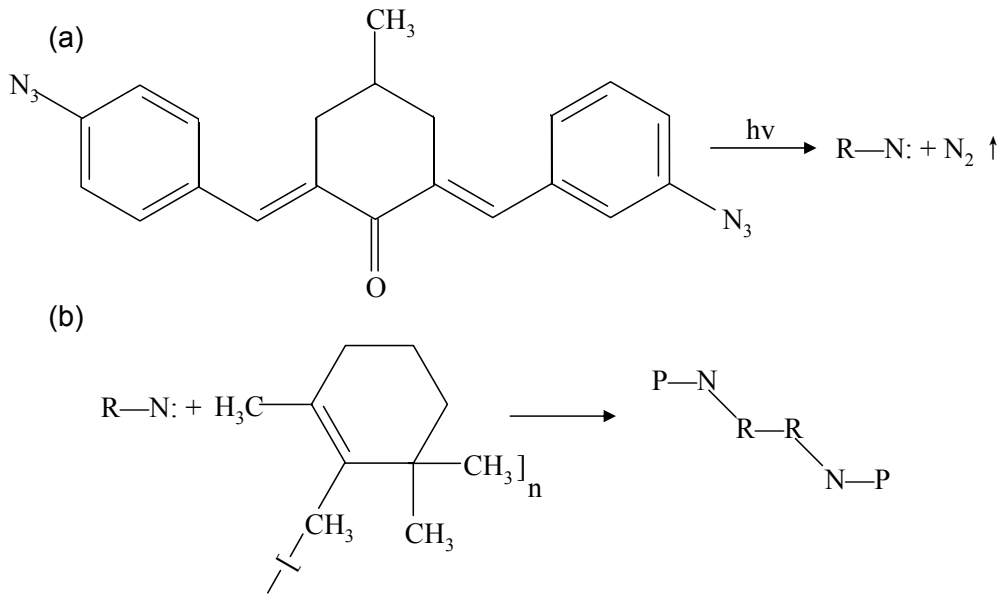

Figure 2.5: Illustration of chemical reaction of a typical negative resist in the exposure process: (a) photon reaction; (b) crosslinking process.

Figure 2.5(b). Thus the exposed area is less soluble when developed.

Photoresist absorption

The optical absorption of photoresist needs to match the emission of the HBO®350 W/S Mercury high pressure short arc lamp. In this work, three positive photoresists (S1805, SPR220-4.5 and SPR220-7.0) were used which were all from *Shipley Co.*; two negative photoresists (ma-N1405 and ma-N1410) used were from *Micro Resist Technology GmbH.* Figure 2.6 shows the absorption spectrum of a typical positive resist S1813 and negative resist ma-N1400. There is a clear overlap between the emission of HBO®350 Mercury high pressure short arc lamp and the absorption spectrum of these two photoresists. The photoresist exposure time is determined by the type of photoresist, thickness of the photoresist film and the reflectivity of the substrate.

Resist spin coating

The most common way to form a photoresist film on a substrate is by spin-coating. There are four stages used to describe a spin coating process. First, photoresist was drop cast on a clean substrate. The second step is spin-up, when the substrate is accelerated to a desired speed. At the third step named spin-off, the resist film reaches an even thickness. And at the final step, the solvent of the

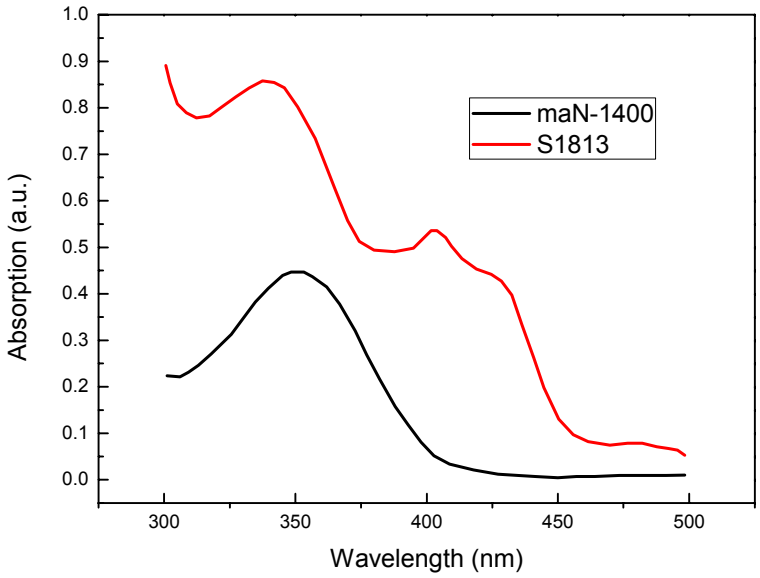

Figure 2.6: Absorption spectrum of positive resist S1813 and negative resist maN-1400.

Table 2.2: Viscosity of applied photoresists (Unit: mPa·s)

Resist	S1805	S1813	S1818	ma-N1405	ma-N1410	SPR220 4.5	SPR220 7.0
Viscosity	5.3	25	39.4	4.3	6.0	124	390

photoresist is evaporated. However, evaporation happens throughout the whole process.

There are several theoretical models predicting the thickness of the resulting photoresist film. The most commonly used model is from Meyerhofer [131]. The film thickness depends on the spin speed ω and the initial concentration c_0, viscosity v and evaporation rate e of the photoresist. The relationship is given by the following equation:

$$h_f = (\frac{3}{2})^{1/3} c_0 (1 - c_0)^{-1/3} \omega^{-2/3} v^{1/3} e^{1/3} \tag{2.4}$$

All the photoresists applied in this work are commercially available. Figure 2.7(a) shows the spin curves (the photoresist thickness as a function of the spin speed) of photoresist S1800 G2 series, ma-N1405 and ma-N1410. Figure 2.7(b) shows spin curves of SPR220-4.5 on a 4" wafer and SPR220-7.0 on 4" and 8" wafers. One can use these spin curves to choose a particular photoresist that fits the individual requirements. The advantage of the spin coating process is its good reproducibility; however, disadvantages are the waste of resist and the edge bead effect as elaborated in the following.

Table 2.2 presents the viscosity of photoresist S1800 G2 and ma-N1400 series.

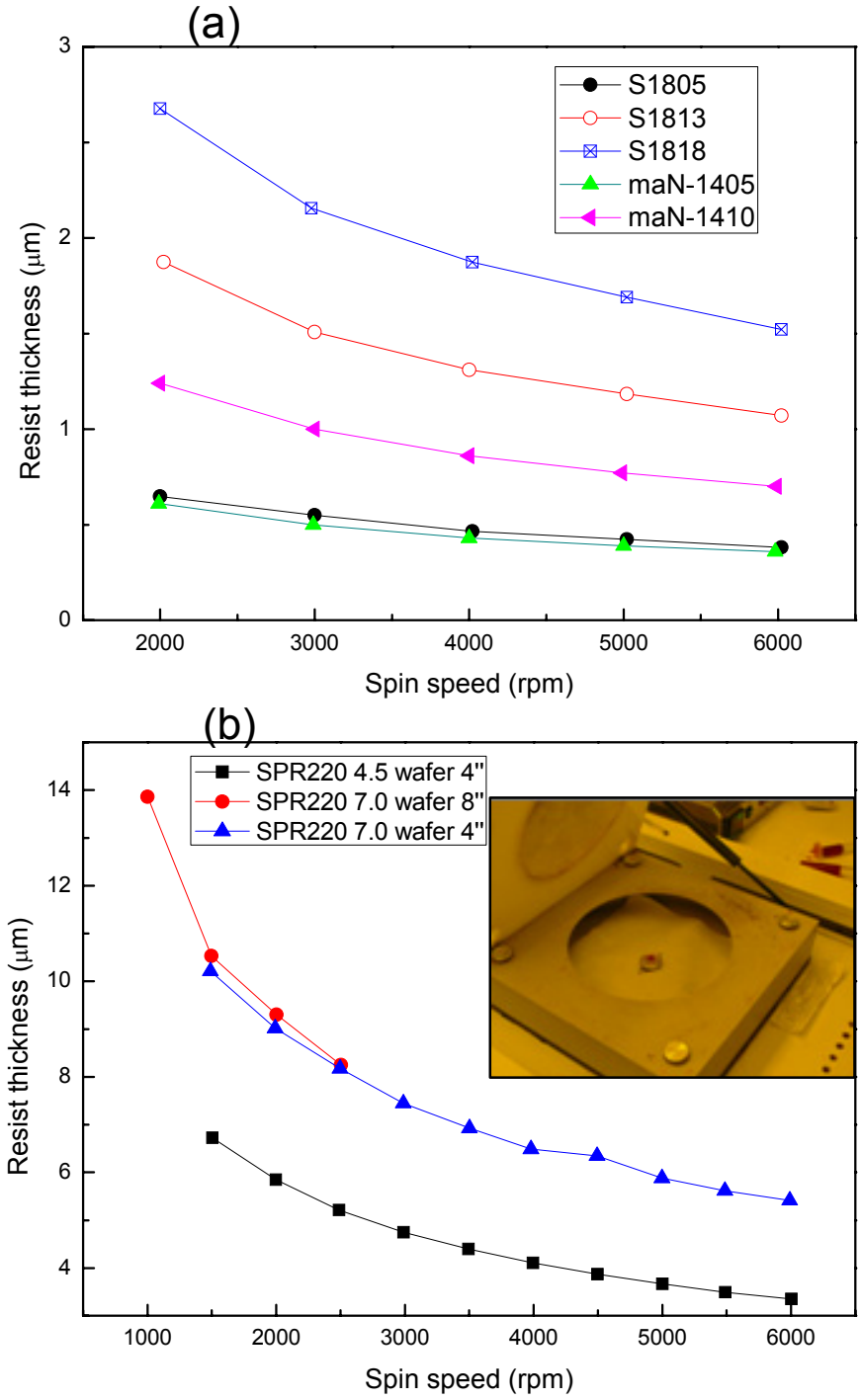

Figure 2.7: Spin speed curves of photoresists used in this work (a) S1800 series and maN-1400 series; (b) SPR220 series with different wafer sizes and a image of spin coater inset. Data is extracted from SHIPLEY and Micro Resist technology GmbH. Image courtesy: Ian W. Watson.

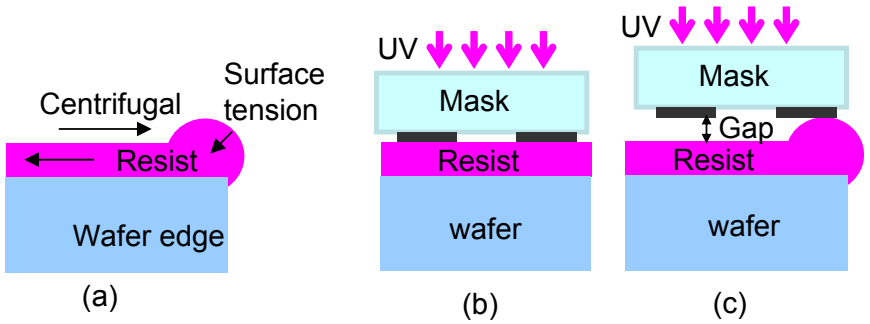

Figure 2.8: Illustration of (a) edge bead formation and influence on contact lithography without edge bead (b) and with edge bead (c).

Viscosity is the quantity that describes a fluid's resistance to flow. The standard unit of viscosity is Pa·s. Water at 20 ^{o}C has a viscosity of 0.001002 Pa·s. As shown in Table 2.2, the smaller the viscosity, the thinner the photoresist. Among the three types of photoresist from the S1800 series, S1805 provides the thinnest photoresist film and S1818 provides the thickest. This is reflected in their spin curves shown in Figure 2.7(a). The same rule could be verified in the ma-N 1400 series whereas ma-N 1405 has a smaller viscosity and thus has a thinner film thickness. The last two digits of a photoresist name represent the thickness of a particular resist film thickness under stardard spin conditions (4000 or 3000 rpm), i.e. S1805-0.5 μm and S1818-1.8 μm. Viscosity is also an important parameter for forming photoresist patterns by inkjet printing (see below) as a suitable viscosity is required to ensure that the photoresist droplets can be jetted out from a micro-sized nozzle.

Edge effect and edge bead

It is usually hard to get uniform spin coating when dealing with quite large (i.e. 450 mm, the next generation industry standard for Si wafers [132, 133]) or very small samples (typically a few mm in diameter, a common size in research labs). The edge bead is formed during the spin coating process and is caused by surface tension as shown in Figure 2.8(a). This will cause an undesired artificial gap between the mask and resist during photolithography as illustrated in Figures 2.8(b) and 2.8(c).

This edge effect becomes very severe when dealing with small samples e.g. <5 mm. However, so far there has been very little research on the edge effect dependence on substrate size and shape. To avoid the edge effect, several resist deposition methods like spray coating and inkjet printing have been developed. The latter method has been adapted here for edge-coupled diamond waveguide

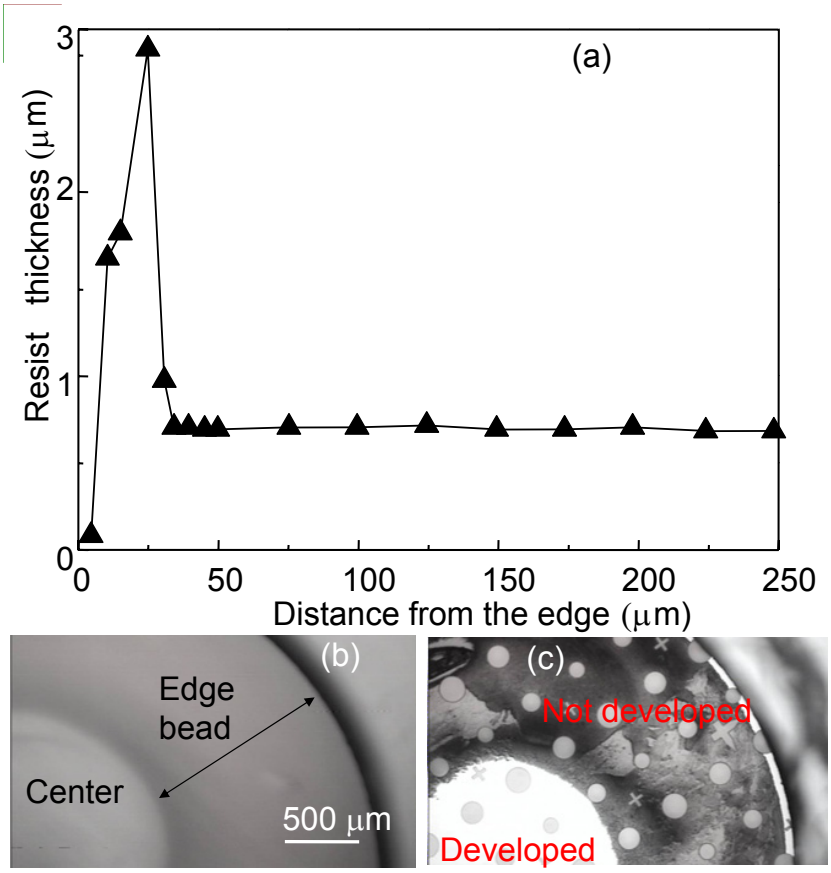

Figure 2.9: (a) Edge bead size measurement from the literature [134]; (b) spin coated photoresist and (c) exposed/developed photoresist pattern on a 4-mm diamond disk. The photoresist is well developed in the centre and incomplete developed on the edge bead as highlighted in (c).

applications and will be presented in a later chapter in this thesis.

The early work on the edge bead effect was done by M. Chan[134] in 1970s. He investigated the resist thickness change from the substrate edge to centre. Figure 2.9(a) shows the result of his measurement. The edge bead is about 3 μm thick for a resist film of a mean thickness of 0.5 μm. Figure 2.9(b) shows the thick edge bead on a diamond sample (diameter: 4 mm). The thick edge bead is visible. Figure 2.9(c) is an image of exposed and developed photoresist pattern of the sample in Figure 2.9(b). As we expected, the features on thick edge bead cannot be well developed. Due to the edge bead, the majority of small substrates (as in our case, diamond) cannot be used.

The edge effect also makes it difficult or impossible to achieve high resolution patterning by contact lithography. In contact lithography, the mask and sample are brought into contact during exposure. Due to the edge bead, there is an air gap between the sample and mask as shown in Figures 2.8(b) and 2.8 (c). Light

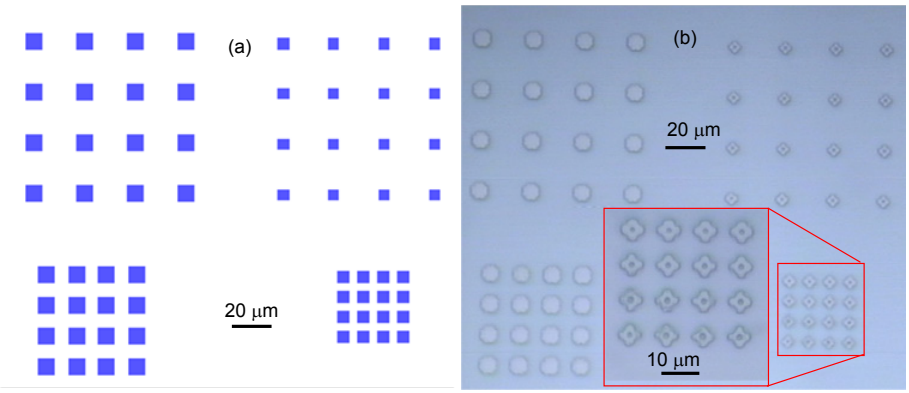

Figure 2.10: Exposed pattern of small sample with severe edge bead with inset is an optical microscopy image of 3 mm × 3 mm square diamond sample with spin-coated resist: (a) mask pattern; and (b) exposed resist pattern.

diffraction will then occur and the high definition pattern cannot be reproduced. Figure 2.10 shows this effect. The exposed resist pattern [Figure 2.10(a)] looks round-shaped because the corners of the square patterns on the original mask [Figure 2.10(a)] have been truncated. Also, it can be seen that in the exposed resist pattern [inset of Figure 2.10(b)], there is a hole in each small photoresist disk. This was induced by the light diffraction and may have some applications to make nano structures [135]. However, it is not desired in most cases.

Resist bake

After spin coating, a hot plate is used to bake the photoresist so as to remove residual solvent. The typical parameters used for the S1805 and ma-N1405 baking in the hot plate are a temperature of 115 ^{o}C for 1 min. For the SPR220 resist, 90 ^{o}C for 1 min is used if a reflow process is required afterwards. The exposure time has been discussed in the previous paragraph. After exposure, the sample is placed in the developer solution for 40 seconds. The developer for all the positive resists is the same: Photoresist developer (MicroDev from Microchem) and DI (Distilled) water in a 1:1 ratio. When fully developed, the sample is rinsed under running DI water for several minutes and then a nitrogen gun is used to dry the sample. The sample is examined under a microscope and can be measured by a surface profile meter (Dektak3) in order to check the overall results. A photoresist reflow process has been used for microlens fabrication process (see Chapter 3). In this process, the sample with exposed and developed SPR220 resist disks is placed on a hot plate at 125 ^{o}C for 2 min. Hard bake is preferred before the dry etching or wet etching process in order to harden the resist film. Dry etching and wet etching processes will be discussed in the following sections.

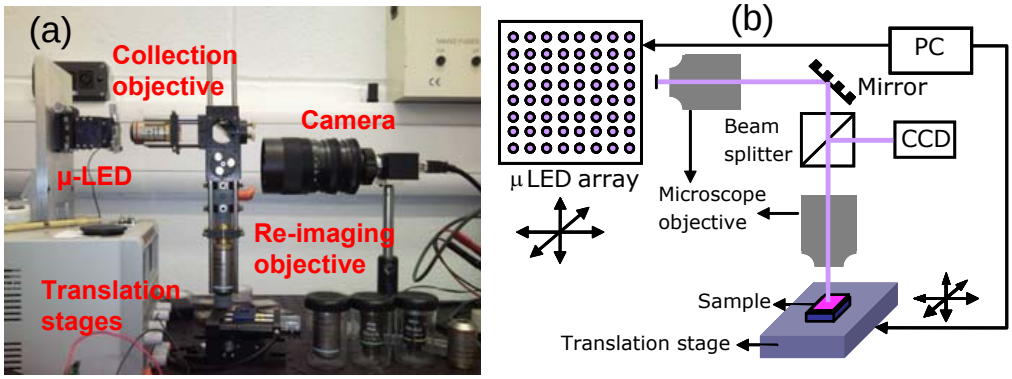

Figure 2.11: (a) Image and (b) schematic of a home-built CMOS-driven μLED wrting setup.

2.1.2 Maskless pattern writing

The photolithography method has many advantages and is commonly used in both industry and academic research laboratories. Photomasks are required in photolithography, however, the photomasks are expensive especially for test-and-trial work in academia. Thus a maskless lithographic method can have advantages. In all maskless lithographic techniques, a beam (ions, electrons or photons, etc.) is focused on the resist and by appropriately moving the beam, in principle any pattern can be written. In this work, two maskless pattern writing methods are used, one is μLED writing and the other is inkjet printing.

μLED writing

The idea of μLED writing comes from laser direct writing [136]. The concept of laser writing emerged from the 1980s by using an UV excimer laser to create small features [137]. With two photon or multiphoton absorption, the advantages of maskless laser writing became clearer [138]. 3D structures such photonic crystals have thus been demonstrated on transparent polymer for example [139]. Direct laser writing has been applied to waveguide and other integrated optical components in polymers and SiO_2, etc. [140, 141]. By using pattern-programmable arrays of gallium nitride (GaN) μ-LEDs to replace the laser, we can reduce the cost greatly and achieve multiple beam writing. In this work, a home-built μLED writing system [142] has been applied to diamond micropillar writing.

Figure 2.11 shows our home-built complementary metal-oxide-semiconductor (CMOS) driven μLED writing setup. An 8×8 UV (365 nm) μLED array was used as the exposure light source. The UV μLED array is bonded and controlled

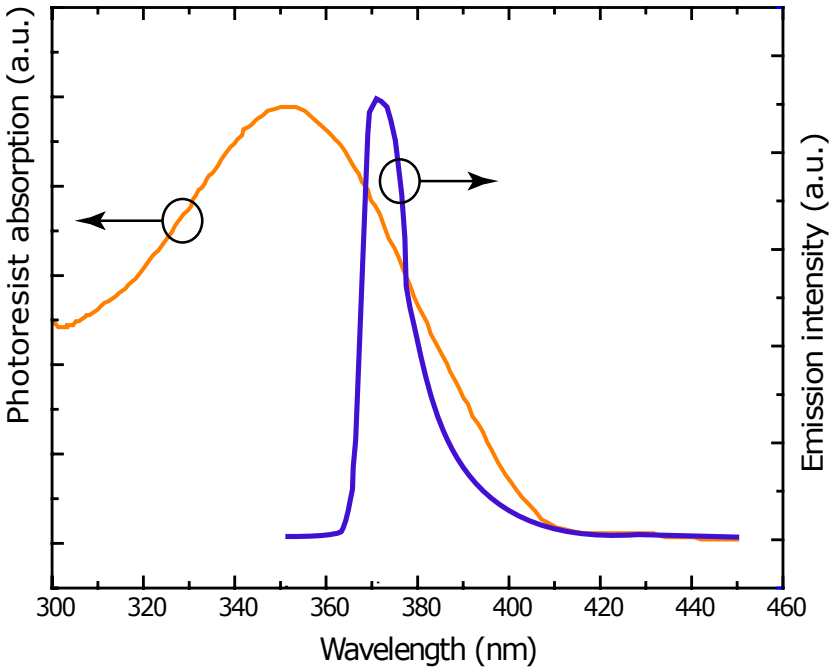

Figure 2.12: The spectrum overlap between emission of μLED (blue) and absorption of photoresist (orange).

by CMOS electronics hence we can accurately control the pulse duration and exposure intervals. A 4X collective micro objective is used to collect the light from the UV μLED array. The focus micro objective is 40X, hence there is a 10:1 demagnification. There is also a beam splitter used to image the sample so that we can check and adjust the desired position before LED writing. As shown in Figure 2.12, the absorption spectrum of resist ma-N1400 and emission of the UV μLEDs overlaps well. SiO_2 was used as a hard mask for diamond pillar etching and the resist pattern was transferred to SiO_2. There are several parameters that can affect the exposure pattern size and shape, for instance, the size of μLED pixel, applied voltage and pulse duration and stage (sample) moving speed. Detailed results will be presented in the diamond micropillar work (see Chapter 3).

Inkjet printing

Inkjet printing is a droplet-based deposition method. By using the inkjet printing technique to create photoresist patterns, the edge effect caused by the spin coating process can be eliminated. A commercial inkjet printer (Dimatix DMP-2800) in our laboratory was used in this work. Photographs of this inkjet printer and its cartridge are shown in Figure 2.13. The DMP-2800 series printer allows the

deposition of various fluidic materials including photoresist [127], nano-particles [143], polymers [144] and bio-samples [145] on substrate up to 8 × 11 inch square. This printer can create and define patterns over an area of about 200 × 300 mm and handle substrates up to 25 mm thick with an adjustable height control. It features a disposable MEMS piezo inkjet cartridge and a fiducial camera. To minimize waste of expensive fluids, each cartridge reservoir has a capacity of 1.5 ml. Cartridges can easily be replaced to facilitate printing of a series of fluids. Each cartridge has 16 nozzles linearly spaced at 254 microns with typical drop sizes of 1 and 10 picolitres (pl). The fiducial camera provides substrate rotation alignment using reference marks and also allows positioning of the print origin to match substrate placement. It can also provide measurement of features and image capture of the printed pattern.

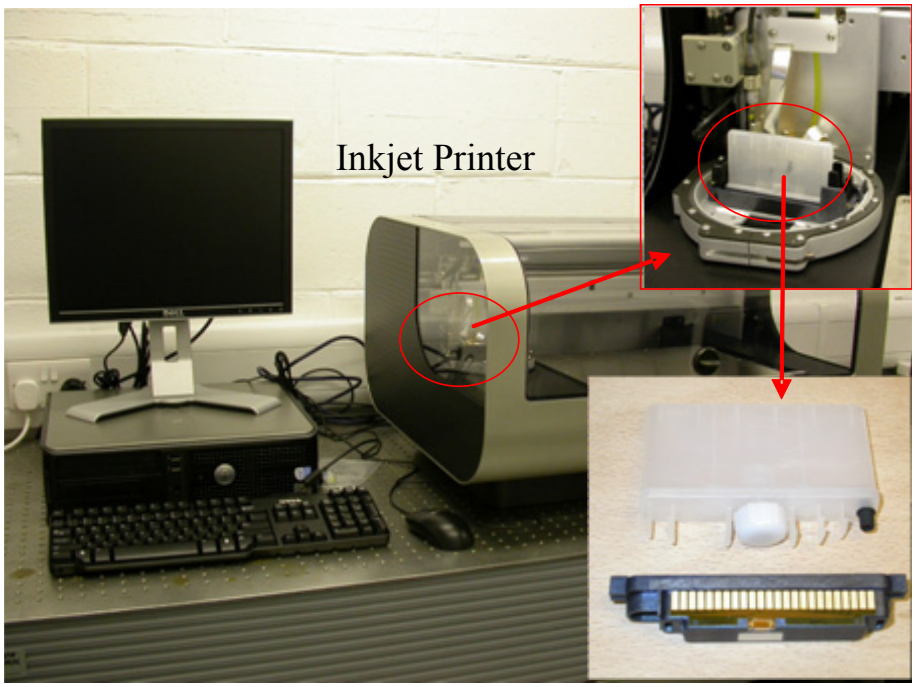

Figure 2.13: Image of the inkjet printer with insets showing a cartridge installed in the printer (top) and an unused one (bottom).

Micro-patterns of various materials can be created onto a substrate by inkjet printing. In this work, uniform photoresist stripes have been successfully printed on small substrates, which are required for photonic waveguide fabrication and very hard to obtain by traditional spin-coating techniques.

To print photoresist patterns, the photoresist S1805 was filled into the cartridge as an ink. During printing, the voltage of piezo actuator was set at 16 V and the print-head's temperature was 30 ^{o}C. We used the 'drop watcher' to take stroboscopic images which show the formation of photoresist droplets from

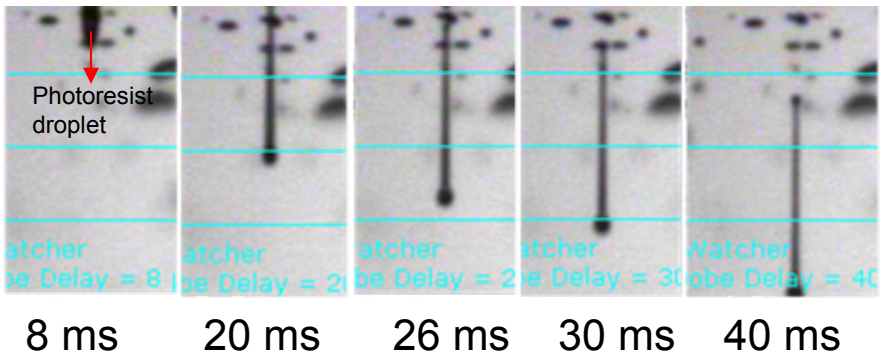

Figure 2.14: Stroboscopic images of single photoresist droplet formation taken from the drop watch window.

the inkjet printer nozzle. The images taken at 8, 20, 26, 30 and 40 ms from the jetting are shown in Figure 2.14.

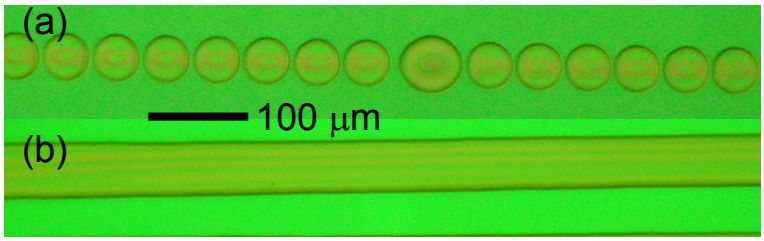

Figure 2.15: Print patterns of photoresist with different drop distance of (a) 50 μm and (b) 30 μm.

In order to print continuous photoresist strip patterns as was required for the work described later in Chapter 4, space between the droplets was carefully adjusted. Figure 2.15 shows two very different patterns which were printed by simply changing the print distance for each drop. When the drop distance (50 μm) is larger than the diameter of the droplets, an individual disk shape pattern was printed as shown in Figure 2.15(a). When the drop space (30 μm) is smaller than the droplet diameter, a continuous strip could be printed as shown in Figure 2.15(b).

The contact angle of a printed droplet is the angle formed at the equilibrium state between a liquid and vapour interface and the solid surface.For a perfectly flat surface, the contact angle θ_C is determined by surface tensions between the liquid/air(gas) γ_{LG}, substrate (solid)/air γ_{SG} and substrate/liquid γ_{SL} as shown in Figure 2.16(a). It is called Young equation $\gamma_{SG} = \gamma_{SL} + \gamma_{LG}cos\theta_C$. In this work, contact angle was measured using a contact angle goniometer FTA32. Figure 2.16(b-c) shows the profiles of 1 μl photoresist S1805 droplets on an as-grown [hydrophilic, as shown in Figure 2.16(b)] and silane (SiH_4) treated [hydrophobic, as

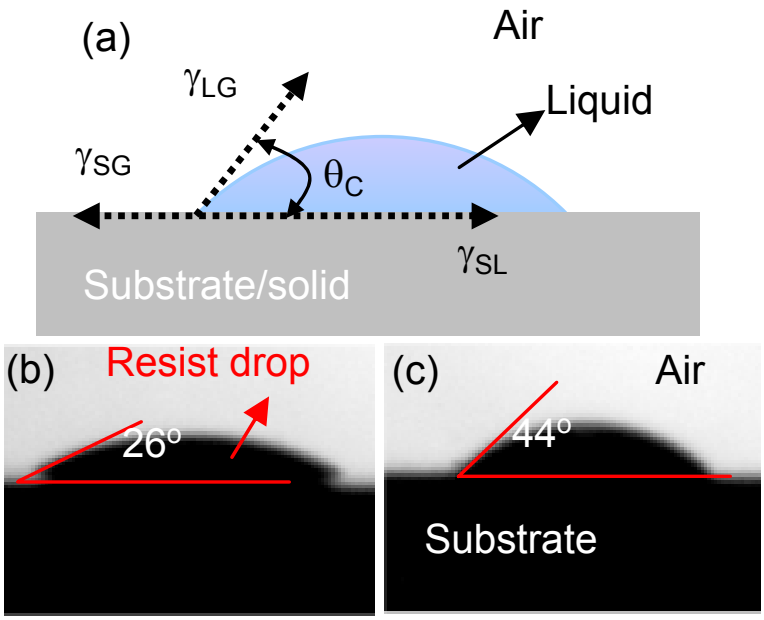

Figure 2.16: (a) Diagram of contact angles and optical sideview images of 1 μl photoresist S1805 droplets on as-grown (b) and silane-treated (c) PECVD SiO_2

shown in Figure 2.16(c)] Plasma-enhanced chemical vapor deposition (PECVD) SiO_2 on silicon substrate. The contact angles of these droplets were measured to be 26^o and 44^o, respectively. This confirms that silane treated SiO_2 surface is indeed hydrophobic and result a higher contact angle.

Figure 2.17 presents a comparison of S1805 photoresist stripe shapes on as-grown and silane treated SiO_2 surfaces. As we can see from the profiles, an S1805 photoresist stripe printed on the as-grown surface [Figure 2.17(a)] is significantly wider than that on a silane-treated surface [Figure 2.17(a)]. These results agrees well with the contact angle measurements of the photoresist S1805 dropets on these two different surfaces. The narrowest stripe we have achieved with a 1 pl cartridge printing is about 20 μm wide. These printed photoresist patterns can be used directly as a mask for further structure fabrication.

We also noted that an S1805 photoresist stripe printed on the as-grown surface has a dip in the middle as shown in Figure 2.17(a). This is caused by 'coffee stain' effect. When a liquid drop dries on a solid surface, it leaves a dense, ring-like deposit along the perimeter. Coffee stain effect has been discussed by R. D. Deegan *et al.* [146]. This effect is also noticeable and discussed for the inkjet printing process. For example, J. C. Batchelor *et al.* reported the coffee stain effect of printed silver ink stripes [147]. Owing to the coffee stain effect, the printed photoresist stripes have a ring-shape with lower height in the centre which is clearly not suitable to act as an etching mask.

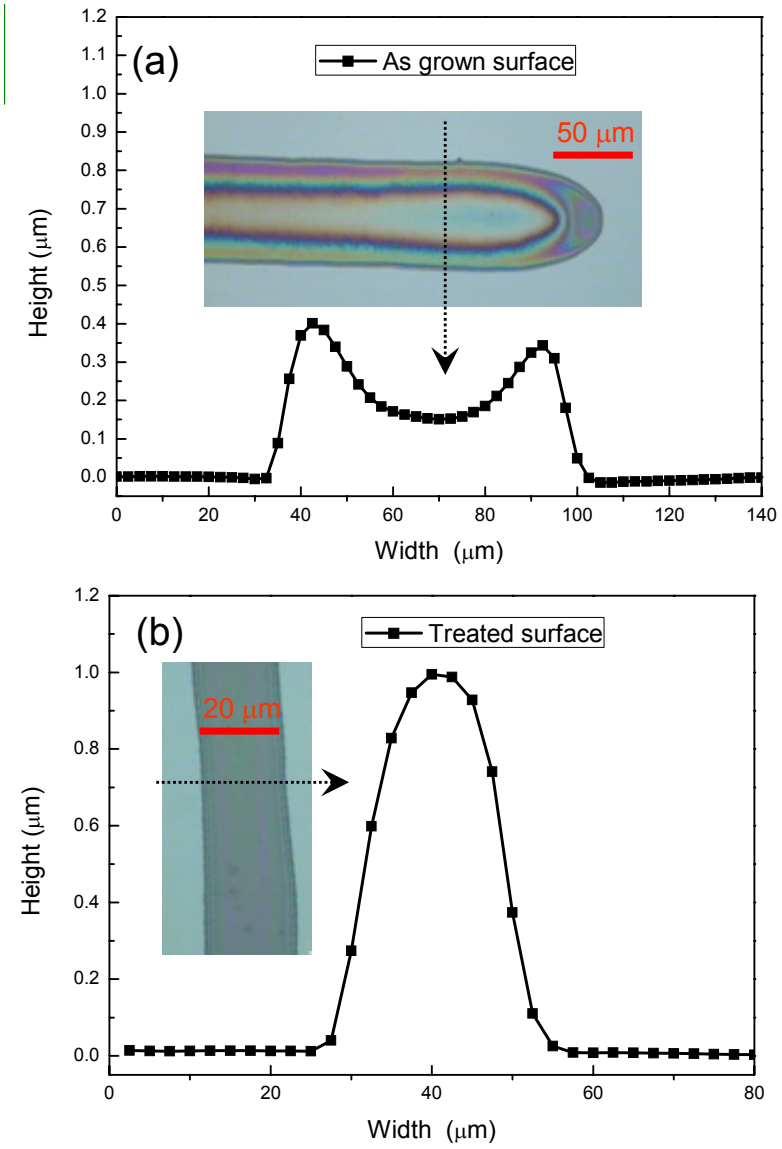

Figure 2.17: Optical images and the corresponding stylus profilemeter measurements of photoresist S1805 stripes printed on (a) an as-grown and (b) silane-treated SiO_2 surfaces.

2.2 Pattern transfer

In microfabrication, the pattern was usually made in soft mask materials such as photoresist. To transfer the pattern to a substrate, etching is needed. There are two major types of etching: dry etching and wet etching.

In contrast to wet etching, in dry etching the material is removed in gas phase instead of by a solvent as in wet etching. There are two different dry etching methods: non-plasma based dry etching and plasma-based dry etching. An example of the non-plasma dry etching is silicon isotropic etching by using

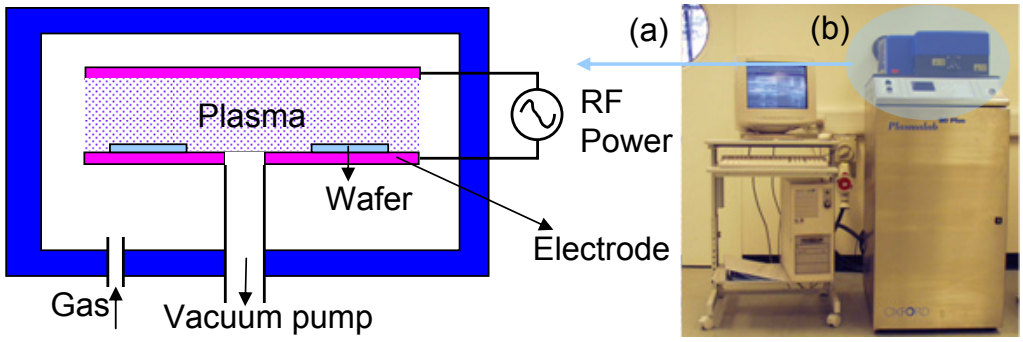

Figure 2.18: (a) Diagram and (b) Image of an RIE chamber. Process chamber is highlighted in blue circle. Image courtesy: Ian W. Watson.

fluorine-containing gases (fluorides or interhalogens). In this work, only plasma-based dry etching was used. Thus, in the following section, plasma dry etching tools, the etching mechanism and the etching parameters are introduced.

2.2.1 Dry etching

Plasma etching tools

A plasma is used to introduce chemically reactive species (atoms, radicals and ions) from inert molecular gas. It is produced in the microfabrication contex by applying a voltage to neutral gases [148]. There are two main dry etching tools used for this work: Reactive Ion Etching (RIE) and Inductively Coupled Plasma (ICP) etch systems. Figure 2.18(a) is a diagram of an RIE chamber. Etching is performed with a radio frequency (RF, 13.56 MHz) induced plasma. Typical process gas pressure in the chamber is between 5 and 150 mtorr and plasma density is about 1 - 5 $\times$ $10^9/cm^3$. The DC bias forms at the substrate electrode. Ion energy (DC bias) is dependent on the applied RF power and gas pressure and ranges from 30 to 1000 eV. The parameters that can be adjusted for different etching process are gas flows, pressure and RF power. Oxford PlasmaLab 80+ RIE System (image of this tool is shown in Figure 2.18(b)) is used for RIE etching for the work in this thesis. The detailed RIE etching recipe will be described for particular structure etching application.

It is worth mentioning here that, hard mask, i. e. SiO_2, is usually used in dry etching to get a better etching selectivity and profile. SiO_2 is deposited using Oxford Plasmalab 80plus PECVD System which is similar to the RIE system in Figure 2.18(b). The basic chemistry of SiO_2 deposition process is:

$$3SiH_4 + 6N_2O = 3SiO_2 + 4NH_3 + 4N_2 \tag{2.5}$$

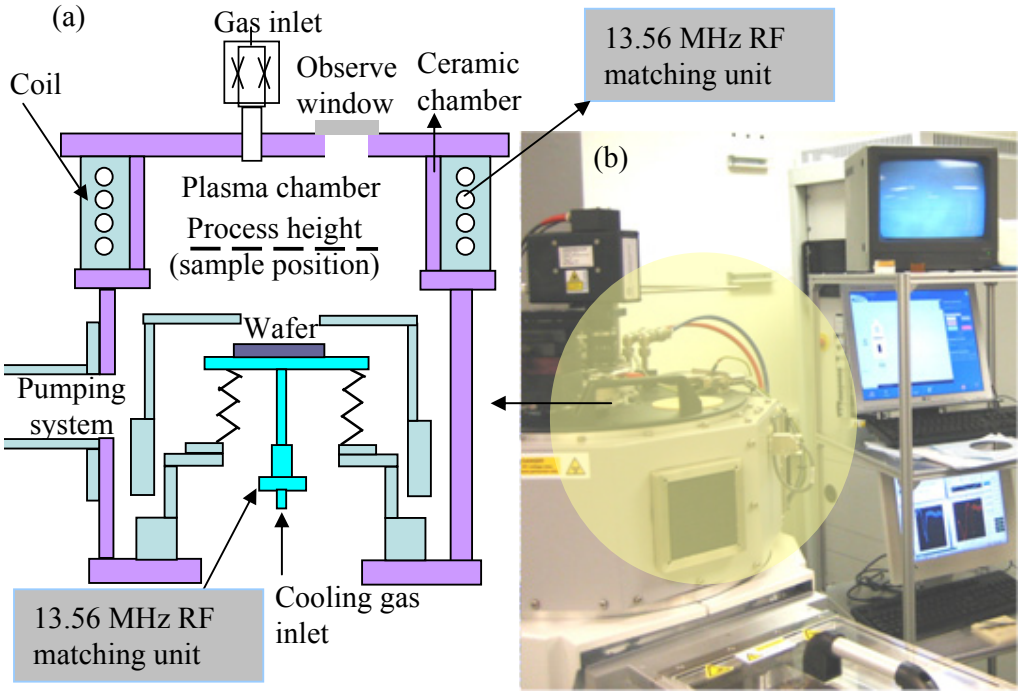

Figure 2.19: (a) Schematic diagram and (b) image of ICP chamber. Process chamber is highlighted in yellow circle. Image courtesy: Ian W. Watson.

Detailed recipe of PECVD process will be shown in later chapters. For diamond and GaN etching, a multiplex ICP etch tool (Surface Technology Systems (STS, now SPTS) shown in Figure 2.19(b)) was used. Figure 2.19(a) is a schematic diagram of an ICP etching tool. An ICP is an RIE with an inductively coupled plasma source. Compared with RIE, ICP has a higher plasma density plasma source which incorporates a coil ICP design. This can provide a higher etch rate. Coil power is used to generate a dense plasma, while the platen power accelerates the ions towards the etching surface. Typical ICP gas process pressure is between 1 to 100 mtorr; plasma density is about 5×10^{11} /cm^3. Ion Energy depends on the platen power and plasma density depends on coil power. Parameters that can be adjusted for different ICP etching process are gas flows, pressure, coil power and platen power. The detailed ICP etching recipe will be described later for particular structure etching application.

General plasma etching mechanisms

There are mainly two basic mechanisms in our plasma etching process and they are shown in Figure 2.20. The first etching mechanism is physical sputtering as shown in Figure 2.20(a). This is a pure mechanical process where the sample surface atoms are removed by particles (usually positive ions) impinging. In this

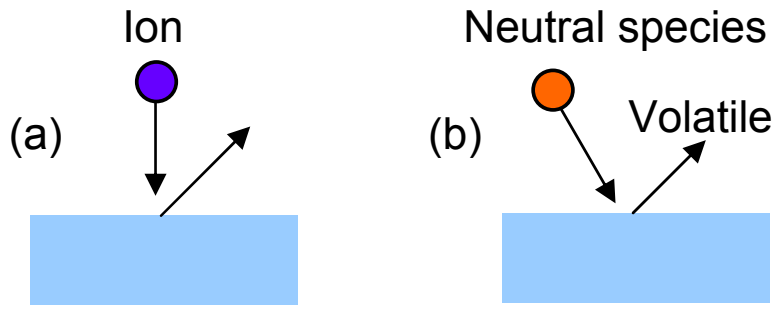

Figure 2.20: Schematics of the two basic plasma etching processes: (a) physical sputtering; and (b) chemical etching.

case, the etching rate is determined by the ion energy of the impinging particles and the chemical bonds of the material.

Figure 2.20(b) shows the pure chemical etching process. This process occurs when active species chemically react with the sample surface layer, forming volatile products. It is essential that the etching products are volatile otherwise non-volatile products would coat the sample surface and no further etching is possible. Pure chemical etching is usually isotropic and highly selective.

Plasma etching variables

A plasma is usually characterized by a set of fundamental parameters such as electron number density and electron temperature. However, these parameters are not generally useful in the semiconductor industry for many reasons [149]. The commonly used instrumental parameters include reactor pressure, RF frequency, power, sample process temperature, gas flow rate, feed gas composition, reactor geometry and materials of construction. These parameters are measurable and thus can be used to define the plasma etching process.

The most-used RF excitation frequency today is 13.56 MHz which is an FCC (US Federal Communication Commission) licensed industrial frequency. At this frequency, the RF generator is readily available and a high radiation level is allowed. Another frequency is microwave at 2450 MHz which is also an FCC industry frequency. The excitation frequency has a key influence on plasma processing. It can change the spatial distribution of species and electrical fields across the discharge. It also influences the minimum voltage that is required to start and operate a plasma. Within the commonly used frequency and pressure (0.05-30 MHz and 1-1000 mTorr), low frequency increases ion energy.

Power refers to the electrical energy applied on the RF electrode. Increasing

Table 2.3: Etching gases of commonly used materials in this thesis

Material	SiO_2	diamond	GaN
Etching gases	CHF_3, O_2	Ar, O_2, Cl_2	Ar, Cl_2

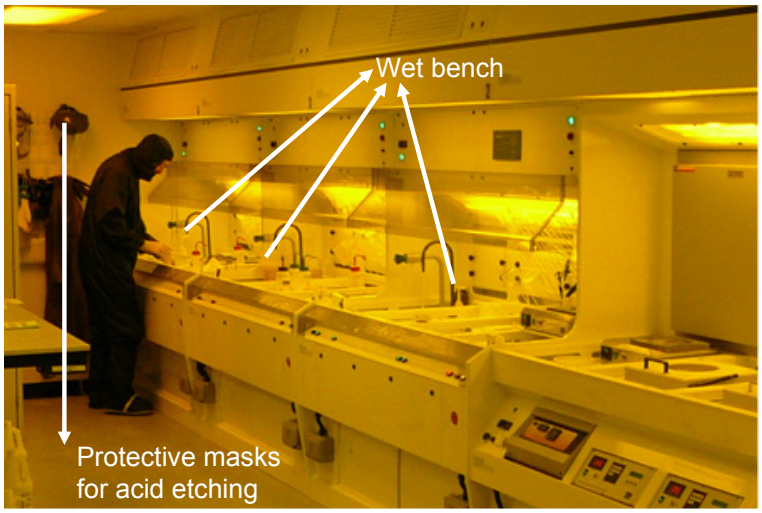

Figure 2.21: Image of wet bench in cleanroom. Image courtesy: Ian W. Watson.

power increases both density and energy of ions and radicals. If the power is too high, surface damage and mask erosion could happen which is undesirable.

The unit of gas flow rate is standard cubic centimeters per minute (SCCM) and gas flow should be large enough to feed the etchant species.

In this work, the most commonly used materials are photoresist, SiO_2, diamond and GaN. Table 2.3 are the corresponding etching gases for these materials. Particular recipes for etching these materials will be presented in later chapters.

2.2.2 Wet etching

Wet etching is a process used to remove material from a substrate. It occurs in a liquid solid interface through chemical reaction universally or selectively. There are several wet etching processes used in this work, such as immersion etching of photoresist in acetone and SiO_2 etching in buffered oxide etch (BOE). All wet etching are carried out in wet bench shown in Figure 2.21.

Resist removal

It is quite often to remove photoresist from the substrate for the subsequent process or to restart the process. This can be done by immersing the sample in a glass beaker containing acetone. Non-crosslinked photoresist is usually quite easily removed. However, acetone has a high vapour pressure and can cause re-

deposition of stripped photoresist onto the substrate because of its fast drying. So a methanol rinse is used after acetone immersion to produce a residual-free surface.

SiO_2 etching

SiO_2 is used as a hard mask for both diamond and GaN etching. Almost all wet etching of SiO_2 is done with hydrofluoric (HF) acid solution. The etching chemistry can be described by the following chemical reaction:

$$SiO_2 + 6HF = H_2SiF_6 + 2H_2O \tag{2.6}$$

Pure HF solution has a very high etching rate. In our lab, SiO_2 etching is done by BOE. It is a buffered solution by mixing in ammonium fluoride (NH_4F). Using BOE has the advantage of controllable etching rate which is about 100 nm/min for PECVD grown SiO_2. As HF reacts with SiO_2 which is the main ingredient of glass, a plastic beaker is used for BOE or any HF solution.

2.3 Summary

In this chapter, the general microfabrication principles and processes including photolithography and plasma etching have been introduced. The edge bead effect in photoresist spin coating process was commented and an inkjet printing method was introduced to overcome this problem. These methods will be applied to diamond and GaN microstructures and waveguides fabrication in the later chapters.

Chapter 3

Diamond microstructures: microlenses and micropillars

In this chapter, I will present my work on diamond micro-optics, especially on diamond microlenses and micropillars, including the development history, physics background and fabrication methodologies. Diamond is a well-known precious material, so the availability of samples is always a concern. In section 3.1, the diamond material availability and development history of natural diamond and synthesis diamond will be reviewed. In section 3.2, I will explain the motivation of making diamond microlenses which can be for example used to increase light extraction efficiency of diamond colour centres, a promising room-temperature single photon source. Such a single photon source is one of the key components to realizing quantum photonic circuits. Geometrical optics and numerical calculations show that a high aspect ratio diamond lens is preferred for such applications. The history of making diamond microlenses is reviewed in section 3.2 as well. We propose two new methods for developing high aspect ratio diamond lenses. The first method is a dual-mask technique which combines resist reflow and two different etching processes as described in section 3.3. The second method for making highly compact diamond lens arrays is to use silica microspheres as a one-step pattern transfer mask. This method is introduced in section 3.4. Atomic force microscopy (AFM) measurement was conducted to access the dimension and smoothness of the resulting diamond lens arrays. In section 3.5, I will present the motivation, simulation and fabrication of diamond micropillars. Two dimensional (2D) Finite-Difference Time-Domain (FDTD) simulation was used to map out the light extraction efficiency versus the dimension of diamond micropillars. In order to fabricate the diamond micropillars, μLED direct writing was used to define photoresist microdots first. This method has the potential to realize in-situ

alignment between a diamond micropillar and a colour centre.

3.1 Overview of diamond material

3.1.1 Natural diamond

The name diamond derives from the ancient Greek $\alpha\delta\alpha\mu\alpha\xi$ (adamas) meaning "invincible" or "untamed" [150]. Diamond's usage in engraving tools dates back to early human history, and diamond has been treasured as a unique gemstone since its use in religious icons in ancient India. Diamond was thought to be first discovered in central India as stated by J. Willard Hershey in his book [151] but the exact date is not clear. Legends tell that diamond was used as jewel around 800 BC. However, recent research conducted by a US-China team suggests that diamond might have been used to polish stone tools by the ancient Chinese in *ca.* 2500 BC [152].

Natural diamond is formed from carbon under enormous temperature (1050 to 1200 ^{o}C) and pressure (45 to 55 kbar) in the earth's mantle ranging from 150 km to 300 km [153] deep. Volcanic explosions forced them upwards and most natural diamond is found in Kimberlite pipes. By investigating the inclusions of diamond, scientists could find the carbon cycle of the earth [154] and thus reveal the mineral formation and evolution of the Earth [155].

Modern natural diamond mining, however, is conducted by large companies which also control the price of diamond. It is notable that the ratio of diamond/treated rock is usually very low. On average, treating 1 ton of stone only produces less than 1 carat (ct, 1 gram=5 ct) of rough diamond. This partially explains why natural diamond is so expensive.

3.1.2 Synthesis diamond

The high price of natural diamond has clearly limited its industrial and scientific applications. At the same time, the high demand for using diamond in various areas has encourages pursuit of synthesis diamond. We all know that diamond is made of carbon. However, it was Antoine Lavoisier who first showed that diamonds are a form of carbon in 1772. Later in 1797, Smithson Tennant repeated and expanded Lavoisier's experiment. By demonstrating that the same amount of gas was released when burning diamond and graphite, he established the chemical equivalence of these substances. His results indicated that diamond could be synthesized from graphite which is literally the same element as diamond [150].

The first claim of man-made diamond was by James Ballantyne Hannay in 1880 [156, 157]. He put hydrocarbons, bone oil and lithium in sealed wrought-iron tubes and heated them. However, his man-made diamond was tested to be natural by modern techniques. Many attempts were undertaken to produce synthesis diamond in the next 70 years but non of the methods is thought to be reproducible [158].

In 1954, F. P. Bundy, H. T. Hall and their co-workers at the General Electric (GE) Corporate Research and Development developed the High Pressure High Temperature (HPHT) apparatus that enabled them to synthesis diamond crystal from graphite. They confirmed that the material obtained was indeed diamond and reported their work subsequently [159, 160]. This was recognized to be the first reproducible diamond synthesis method. Today, this HPHT method is widely used for industrial diamond production. Large gem quality crystals can be grown by the HPHT process, up to 4.6 carats for colourless diamonds, and up to 25 carats (5 g) for yellow ones [161].

Another diamond synthesis method is low pressure chemical vapour deposition (CVD). Several groups including Boris V. Spitsyn from the Soviet Union, and W. G. Eversole [162] and John C. Angus [163] from the US developed this technique independently. More references on diamond CVD synthesis can be found in these two review papers [164, 165]. These efforts significantly increased the availability of diamond materials with controllable properties and lower price [166] for industry and academia. The synthesis diamond has wide applications including diamond tools like diamond drills and abrasive, diamond electrical devices such as diamond detectors to operate in extreme environments and diamond optics such as diamond window for high power lasers and X-rays. In recent years, as described in Chapter 1, diamond has drawn a lot of attention for developing solid state room temperature single photon emitters, one of the important components for integrated quantum photonic circuits.

3.2 Background on diamond lenses

Due to their unique thermal and optical properties, diamond microlenses have a wide range of potential applications. Since the colour (NV) centre is embedded in the diamond bulk crystal, the light extraction efficiency is rather low. We are therefore interested in fabricating diamond lenses for increasing light extraction efficiency, as an important step to achieve a usable diamond single photon source.

3.2.1 History of diamond lenses

Owing to the chemical inertness and hardness of diamond, to fabricate diamond photonic components is technically challenging. The diamond lens fabrication methods reported so far are summarized in Table 3.1. An early attempt to make diamond lenses was made by Andrew Pritchard in 1824 with the intention of developing a diamond lens for a microscope. In the modern age, W. Nelissen *et al.* fabricated and polished a 1 mm diameter diamond solid immersion lens (SIL) with a flatness better than 10 nm from homo-epitaxial CVD diamond [167]. P. Siyushev *et al.* reported they could increase by one order of magnitude the efficiency for the detection of single photon emission by adding this diamond SIL [168]. However, the diamond SIL used in their work is quite large and not readily scalable. A diamond micro-SIL was proposed by J. P. Hadden *et al.*, in which they milled the diamond SIL by making several ring cuts with different diameters with focused ion beam (FIB) [169]. This method could be scalable in principle and has the capability of aligning the lens with the individual colour centre [170]. Ronald Hanson used the similar FIB method to fabricate diamond immersion lenses [59]. With these lenses, two-photon quantum interference from separated NVs and high-fidelity projective read-out of a solid-state spin quantum register have been demonstrated [171]. However, we noted that the FIB milling method is very time consuming because the FIB process is very slow.

The second method for diamond lens fabrication is a bottom-up CVD growth approach reported by E. Woerner [173]. In that case, they deposited diamond onto a structured substrate then lifted off the diamond to form the lenses afterwards. This method can produce diamond lens arrays. However, the diamond grown on such a foreign substrate so far reported can only be polycrystalline.

The third method involves the use of photoresist melting reflow and plasma etching. The plasma etching transfers the lens pattern formed in photoresist to diamond [174, 175]. The microlenses made in this way are usually very shallow (e.g. the maximum height of the diamond lenses reported so far is 2 μm for the lens diameter ranging from 20 μm to 100 μm) due to the poor selectivity of diamond over resist.

In this work, our target is to fabricate diamond microlenses with a high aspect ratio. Combined with photoresist reflow and plasma etching, a dual-mask method was developed to obtain the diamond lenses. This method will be presented in section 3.3.

Table 3.1: List of reported diamond lens in literature.

Year	Groups	Institution	Method	Dimension	Application and references
1842	A. Pritchard	Optician,18 Picket Street, London, England	Grinding and Polishing	0.05 inch focus	Microscopy[172]
2001	E. Woerner	Fraunhofer-Institut für Angewandte Festkörperphysik	CVD-diamond deposited on structured lens template	diameters between 3 and 5 mm and radii of curvature ranging from 4.5 to 7.3 mm	High power laser windows [173]
2003	M. Karlsson	Uppsala University	Photoresist reflowed lens mask and plasma etching	diameter 90 μm, height 2 μm	Diamond optics in high-power laser applications [174]
2004-2012	M. D. Dawson and E. Gu	University of Strathclyde (IoP)	Photoresist reflowed lens mask and plasma etching	diameter 10-100 μm, height smaller 2 μm	Diamond optics in high-power laser applications [175–178]
2006	W. G. M. Nelissen	Element Six	Nd:YAG laser cut and polishing	Hemispherical lens with a few mm in diameter	Near-field optical storage [167, 179]
2010	J. Wrachtrup	Universität Stuttgart	Combination of laser and mechanical processing stages	1 mm diameter SIL	Single photon detection [168]
2010	J. Rarity	University of Bristol	Focused Ion Beam	5 μm diameter SIL	Single photon detection [169]
2011	J. L. O'Brien	University of Bristol	Focused Ion Beam	8 μm diameter SIL	SIL registered to single emitters in diamond [170]
2011	R. Hanson	TU Delft	Focused Ion Beam	10 μm diameter SIL	SIL registered to preselected NV centre in diamond for spin readout [171]
2012	R. Hanson	TU Delft	Focused Ion Beam	10 μm diameter SIL	Two-photon quantum interference from separate NVs [59]

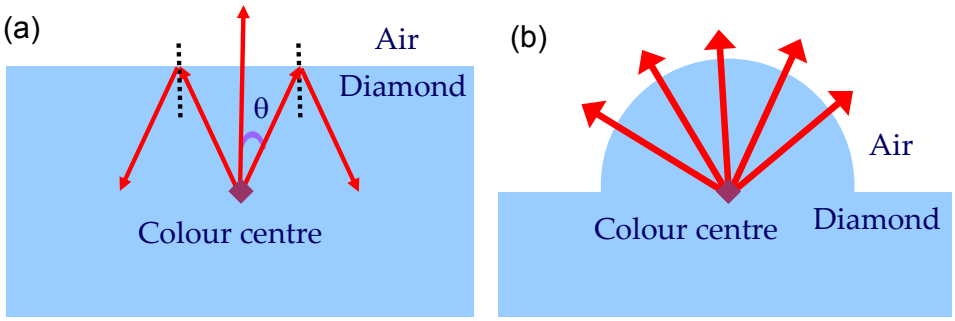

Figure 3.1: Illustration of total reflection between the interface of diamond and air (a) flat surface and (b) with a diamond hemispherical lens.

3.2.2 Physics of diamond lenses

In order to understand how an integrated diamond lens is able to increase the light extraction efficiency of an NV centre (i.e. a single photon emitter), the principle and function of a diamond lens are briefly introduced here.

At the interface between diamond and air, the critical angle θ_c can be calculated using $\theta_c = arcsin\frac{1}{n} = arcsin\frac{1}{2.4} = 24.6^o$, where $n = 2.4$ is the refractive index of diamond. Due to the total internal reflection, the light emission cone from an NV centre is therefore restricted to 24.6^o as shown in Figure 3.1(a). By fabricating a diamond hemispherical lens with a high aspect ratio and integrating it with an NV centre, the emission restriction due to the total internal reflection is removed and thus the photon extraction efficiency increases dramatically as shown in Figure 3.1(b). Two independent groups have presented their detailed calculations using a ray tracing method and their results showed a 7.5-fold enhancement of collection efficiency by use of a diamond hemispherical lens [168, 180]. For a small diamond lens, the geometrical optics assumption may not be valid. By using FDTD simulation, it was shown that a hemispherical diamond lens could even produce an efficiency enhancement in the order of 10 [169].

In practice, the fabricated diamond micro-lens may be misaligned from the NV centre. Stefania Anna Castelletto et al. gave a calculation on the extraction efficiency with the displacement of an NV centre inside a FIB SIL with diameter of 5 μm using FDTD simulation [181]. In what follows, combining geometrical optics analysis with numerical calculation, we examine the general case of extraction efficiency with respect to the displacement of a diamond colour centre inside a hemispherical lens.

As shown in Figure 3.2, we have a hemispherical diamond lens with a radius of R and centre coordinates (0,0). The diamond NV centre is at a position (x_s, y_s).

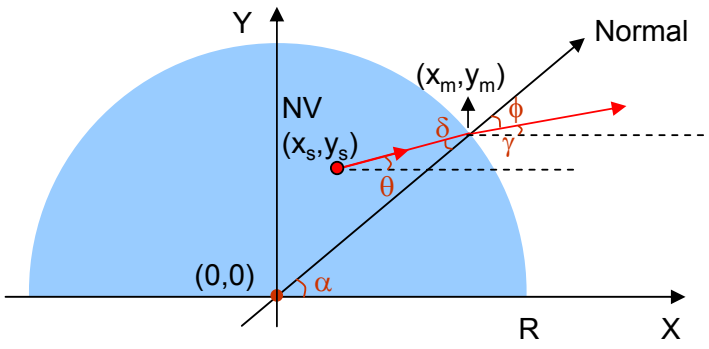

Figure 3.2: Diagram of a diamond NV center inside a diamond hemispherical lens with arbitrary position.

Then for an arbitrary ray emitted from this NV centre with an angle of θ to the horizontal, we can find the point (x_m, y_m) where the emission ray reaches the lens surface. The incident angle δ and refraction angle ϕ, together with the slope angle of refracted ray γ are illustrated in Figure 3.2. We can write down the trigonometric relations between these parameters as:

$$x_m^2 + y_m^2 = R^2 \tag{3.1}$$

$$tan\theta = \frac{y_m - y_s}{x_m - x_s} \tag{3.2}$$

For a given NV position (x_s, y_s) and emission angle θ, we can solve the above two equations and find (x_m, y_m). First, we can work out α for a given (x_m, y_m):

$$\alpha = arctan\frac{y_m}{x_m} \tag{3.3}$$

The incident angle is:

$$\delta = \alpha - \theta \tag{3.4}$$

Due to the total internal reflection, the light can be emitted out of the lens only for $\delta < 24.6^o$ otherwise it will be reflected. Applying Snell's laws of refraction, we can work out the refraction angle ϕ for any $\delta < 24.6^o$, using the relation:

$$n = \frac{sin\delta}{sin\phi} \tag{3.5}$$

Then the slope angle of the refracted ray, γ, is:

$$\gamma = \alpha - \phi \tag{3.6}$$

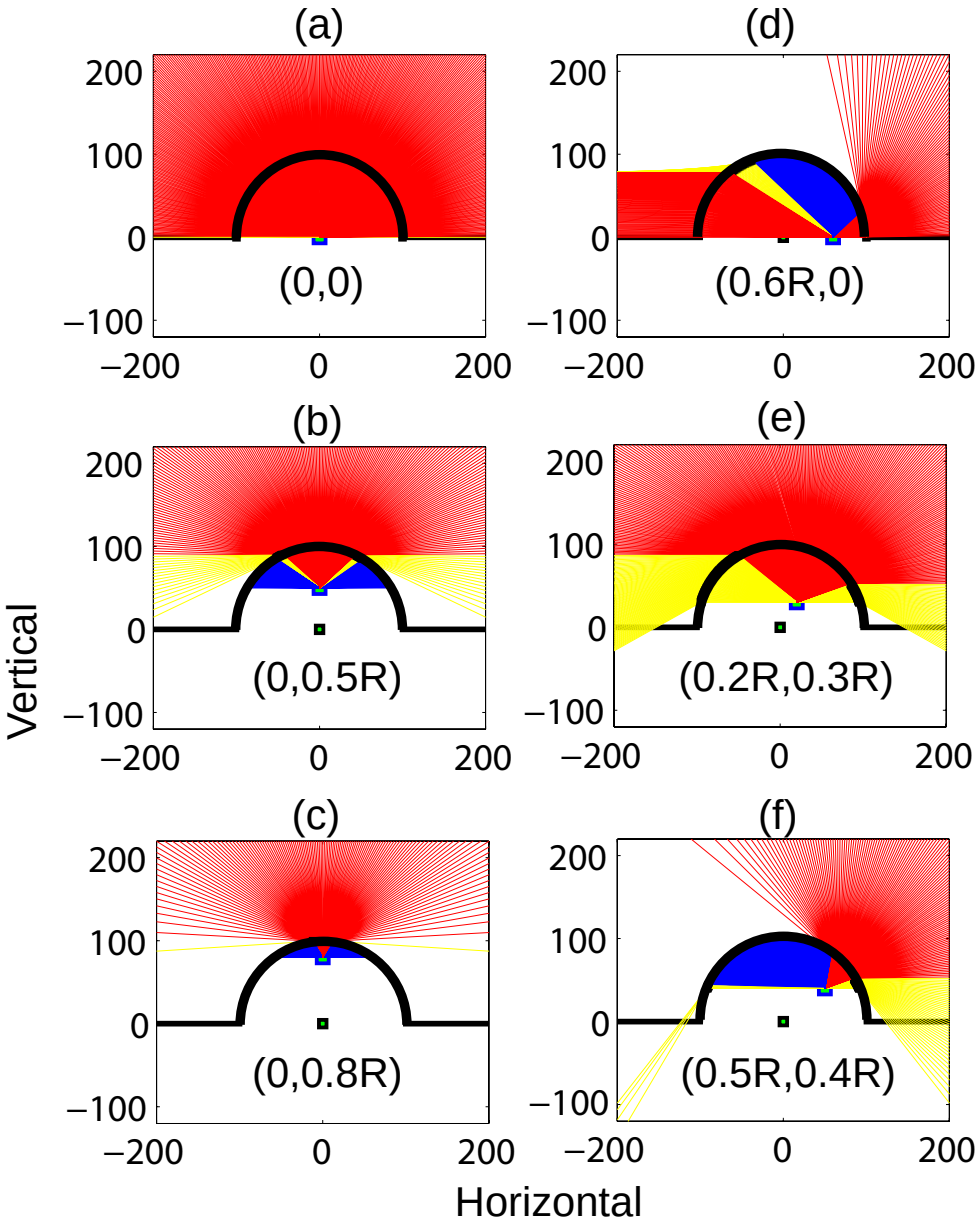

Figure 3.3: Numerical calculations of diamond NV emission pattern with six different position inside a hemispherical lens; diamond NV centre coordinates are displayed in subplot (a-f). Blue rays are total reflections where $\delta > 24.6^o$. Red rays are emission in the top cone where $\phi > 0^o$. Yellow rays are emissions in the bottom cone where $\phi < 0^o$.

To show the effect of the displacement, we choose 6 typical NV centre positions and plot the corresponding emission patterns in Figure 3.3. For these calculations, the radius of the hemispherical lens, R, was set to be 100 arbitrary units. It should be pointed out that inside the diamond hemisphere lens, for simplicity, only one total reflection (i.e. no 2nd/3rd total reflections) was considered. In Figure 3.3,

Table 3.2: Total extraction efficiency of 6 typical NV centre positions.

Source	(0,0)	(0.6R,0)	(0,0.5R)	(0.2R,0.3R)	(0,0.8R)	(0.5R,0.4R)
T_s	41.38%	15.77%	20.15%	25.72%	12.47%	12.46%
T_p	41.38%	18.54%	23.48%	29.68%	15.29%	14.48%

blue rays are those subject to total reflection where $\delta > 24.6^o$. The red rays represent the upward emission where $\gamma > 0^o$. The upward light emission can be readily collected. The yellow rays are downward emissions where $\gamma < 0^o$ which are difficult to collect. As we can see in Figure 3.3(a), when a diamond NV centre coincides with the geometrical centre of the hemispherical lens, the emission angle is maximum. When the diamond NV centre is placed higher as shown in Figures 3.3(b-c), the emission cone becomes smaller and smaller. Figures 3.3(d-f) show three other cases where the NV centre is placed at different positions.

The refracted light intensity can be calculated from Fresnel Equations [182].

For perpendicularly (s-) polarized light, reflection coefficient r_{sm} of a given incident ray is:

$$r_{sm} = \frac{n \cdot cos\delta - cos\phi}{n \cdot cos\delta + cos\phi} \tag{3.7}$$

For parallel (p-) polarized light, reflection coefficient r_{pm} of a given incident ray is:

$$r_{pm} = \frac{n \cdot cos\phi - cos\delta}{n \cdot cos\phi + cos\delta} \tag{3.8}$$

The reflectivity R_{sm} and R_{pm} of s- and p- polarized light is defined as follows:

$$R_{sm} = r_{sm}^2 \tag{3.9}$$

$$R_{pm} = r_{pm}^2 \tag{3.10}$$

We can then work out the transmittance T_{sm} and T_{pm} of s- and p- polarized light:

$$T_{sm} = 1 - R_{sm} \tag{3.11}$$

$$T_{pm} = 1 - R_{pm} \tag{3.12}$$

For each individual light ray emitted from the diamond NV centre through the diamond lens (red rays in Figure 3.3), we can calculate the transmittance T_{sm} and T_{pm}. Adding all transmittance together and normalized, we can have the total extraction efficiency T_s and T_p. Table 3.2 gives the total extraction efficiency of 6 typical NV centre positions corresponding to those shown in Figure 3.3(a-f).

These results show that the emission cones strongly depend on the position

of the NV centre and compared with Figure 3.3(a), the light extractions in these cases are all reduced. Clearly, such effect due to misalignment can be reduced by using the microlenses with a high aspect ratio, preferably hemispherical lenses.

3.3 Diamond microlens fabrication and dual-mask method

In this section, a general overview of photoresist reflow/etching method for microlens fabrication is first reviewed. Then the dual-mask method which can be used to fabricate diamond lenses with a high aspect ratio is introduced.

3.3.1 Photoresist reflow/etching to make microlenses

This method was first proposed by Zoran D. Popovic *et al.* in 1988 [183] and involve the melting of photoresist disks to form lenticular masking features. Later on, by using the reflow method Dan Daly *et al.* developed spherical and square shape resist lenses [184]. Dan Daly also wrote a book on the development of the resist reflow/etching techniques for microlens fabrication [185].

Combining photoresist reflow with plasma etching, the photoresist lens shape can be transferred to substrates to make monolithic microlenses. For silicon-based material systems, in 1991, C. L. Jones *et al.* reported silicon microlenses etched by Ar ion beam from reflowed resist lenses [186]. In 1994, Pekka Savander reported microlens arrays etched into glass and silicon by RIE [187]. Margaret B. Stern also reported several silicon microlens fabrication methods including etching pre-shaped polymers [188, 189]. Martin Eisner and Johannes Schwider demonstrated that RIE can be used to transfer spherical resist microlenses into silicon [190]. These results showed that the form of the lenses in the substrate can be controlled by varying the etching gas compound thus changing the etching rate ratio between the resist and the substrate. In 1999, Marco Severi and Patrick Mottier reported the modification of the transferred lens profile by changing the etching rate ratio of silica and photoresist [191]. In 2001, Ph. Nussbaum and H. P. Herziglow demonstrated low numerical aperture refractive microlenses in fused silica [192]. Reinhard Voelkel *et al.* reported a diffraction-limited optical performance of aspherical microlenses in fused silica and silicon [193]. A 15-μm-diameter solid immersion lens was fabricated and used for scanning near-field optical microscopy by Daniel Fletcher *et al.* [194].

III-V compound semiconductor lenses have been fabricated by photoresist

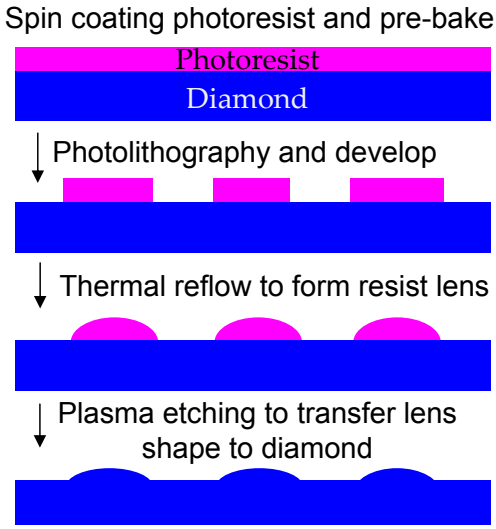

Figure 3.4: Diamond microlens fabrication process.

reflow/etching as well. In 1997, Strzelecka *et al.* demonstrated GaAs and InP microlenses integrated with vertical-cavity laser diodes and photodetectors [195]. Oder *et al.* reported nitride microlens arrays with a lens size as small as 10 μm fabricated by using ICP etching in 2003 [196]. Our group demonstrated GaN negative and bifocal microlenses in 2005 [176]. Young Min Song *et al.* in 2009 reported GaAs lens-like arrays with a high aspect ratio achieved by adjusting the RF power during etching [197]. Jung Woo Leem *et al.* demonstrated parabolic nanostructure on GaAs in 2011 [198]. Wu *et al.* reported the fabrication of a near perfect GaAs hemispheres in 2011 [199].

Chlorine-based ICP etching has been used to fabricate microlenses on mechanically hard and chemically inert materials like sapphire. The first sapphire microlenses were fabricated by Si-Hyun Park *et al.* [200] and such sapphire microlenses were further developed for flip chip LED applications [201, 202].

Diamond microlenses were fabricated and reported by Karlsson *et al.* in 2003 and were further extensively investigated by our group at the Institute of Photonics, University of Strathclyde [174–177]. However, due to the lower etch selectivity between photoresist and diamond, the height of diamond microlenses reproted so far is typically less than 2 μm.

The fabrication process of diamond microlenses by using photoresist reflow/etching is illustrated in Figure 3.4. Firstly, photoresist was spin-coated on a diamond surface and then was exposed and developed to make a photoresist microdisk. An appropriate temperature (120 ^{o}C for photoresist SPR 220) was then applied to melt the photoresist and the spherical lens structures were formed due to the surface tension of the melted resist.

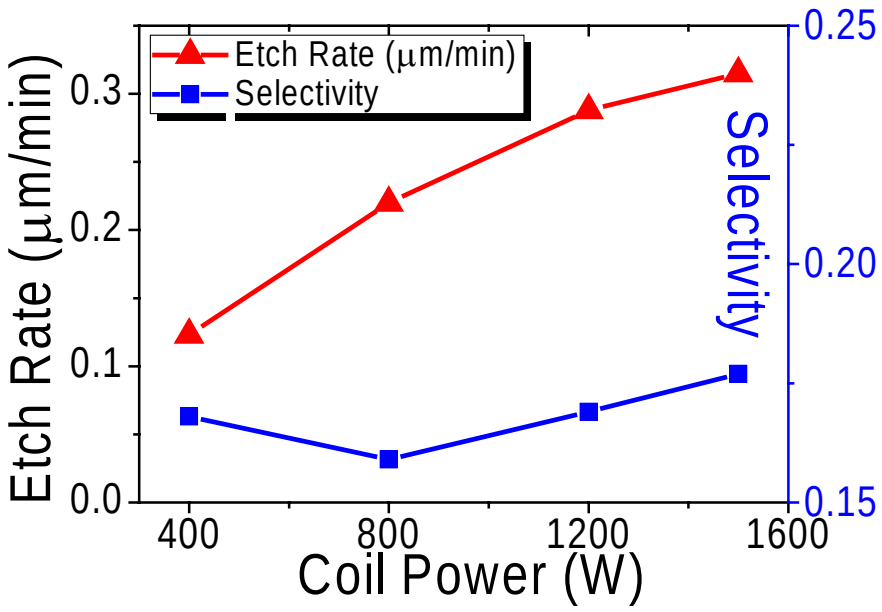

Figure 3.5: Etching rate of diamond (red curve) and the etching selectivity between diamond and photoresist SPR220 7.0 (blue curve) vs ICP coil power. Other parameters are platen power: 300 W; gas pressure: 5 mTorr; Ar/O_2 gas flows:15/40 sccm

Assuming the volume of the resist does not change before and after the thermal reflow process, we can calculate the heights of the reflowed resist lenses with various diameters. With a initial resist thickness of 20 μm, the height of the reflowed lens with a diameter of 50 μm is close to half ($\sim$ 25 μm).

In our work, ICP etching was applied to transfer the reflowed photoresist lenses into the diamond substrate. The maximum diamond etching rate achieved is 300 nm/min under the highest coil power of 1400 W, a platen power of 300 W and a gas pressure of 5 mTorr, with Ar/O_2 gas flows at 15/40 sccm. With a fixed platen power of 300 W, the diamond etch rate versus ICP coil power is shown in Figure 3.6. We found that after ICP plasma etching, the diamond lens height is significantly lower than that of the photoresist lens because of the low etch selectivity between diamond and resist as shown in Figure 3.5. The etch selectivity can be slightly changed by using different coil/platen powers and gas pressures, etc. But the typical selectivity is about 0.16 meaning that the obtained diamond lens height is about 16% of the initial photoresist lens height. Therefore, the diamond microlenses made by direct photoresist pattern transfer have a small lens height of less than 2 μm for an initial photoresist thickness of 7 μm. SEM images of diamond microlenses fabricated by this way are shown in Figure 3.6.

Of course, the diamond lens height can be increased by using a thicker resist

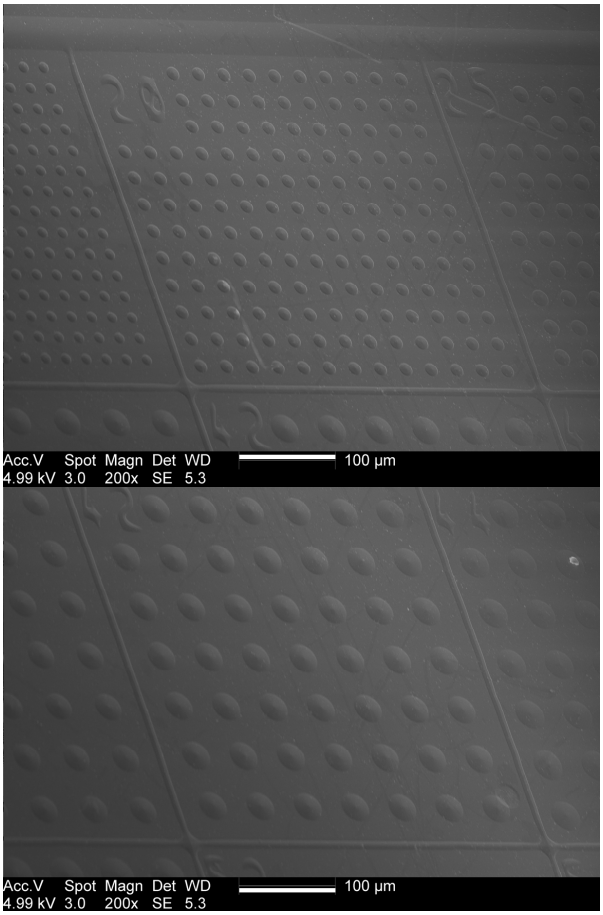

Figure 3.6: SEM images of diamond lenses with two different magnifications.

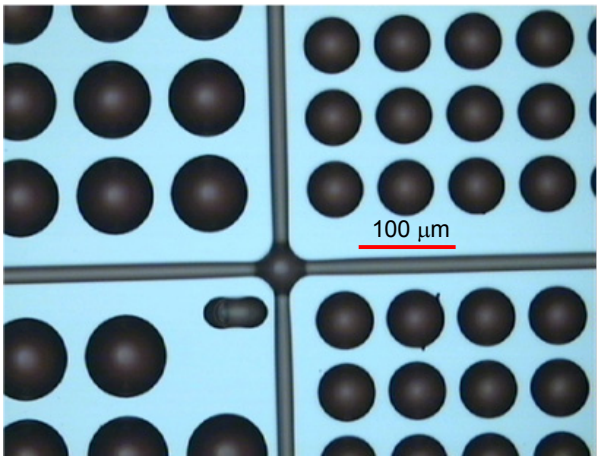

Figure 3.7: Optical microscopy images of photoresist lenses with thicker initial resist layer.

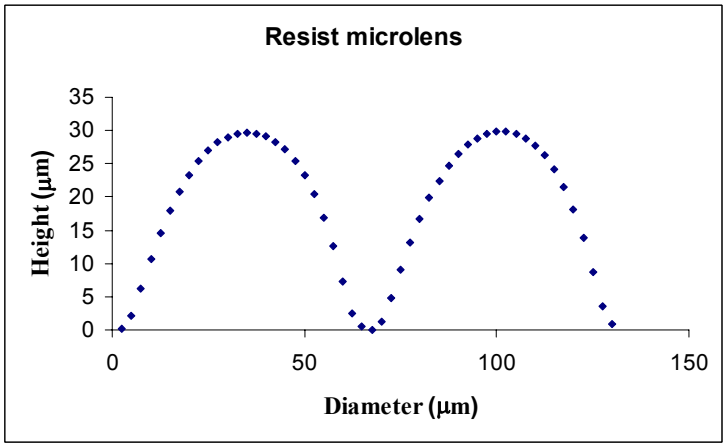

Figure 3.8: Surface profile of two photoresist microlenses with thicker initial resist layer.

layer, e.g. by doubling the resist layer thickness from 7 to 14 μm. The optical microscopy image and surface profile of photoresist microlenes made of a 14 μm thick photoresist layer are shown in Figures 3.7 and 3.8 respectively. For these thick photoresist lenses, the measured and calculated lens profiles are still not hemispherical however. Another issue we would like to point out here is that the edge bead effect is very severe when applying the thick photoresist onto small diamond substrates. Clearly, this photoresist reflow method is not very suitable for fabricating diamond microlenses with a high aspect ratio.

3.3.2 Dual-mask method

Since the limitation of diamond lens height comes from the low etch selectivity between diamond and photoresist, a dual-mask technique was proposed and developed in this work in order to realize hemispherical diamond micro-lenses with a reasonable size. In this technique, a second mask (SiO_2, in this case, although other mask materials can also be used) was introduced and due to the different selectivities of the photoresist and SiO_2 over diamond, this method provide a new approach to achieve diamond micro/nano structures with a high aspect ratio.

The etch selectivity of SiO_2 over photoresist is 0.25 in Ar/Cl_2 etching. For a 12 μm photoresist microlens, the resulting SiO_2 microlens is 3 μm high after Ar/Cl_2 etching.

In this work, by adjusting the etch parameters, we have achieved an etch selectivity of diamond over SiO_2 of about 10 using Ar/O_2 plasma etching. This means, the 3 μm high SiO_2 microlens can produce a 30 μm high diamond microlens.

Thus, we can get a net etch selectivity of 2.5 for diamond over photoresist

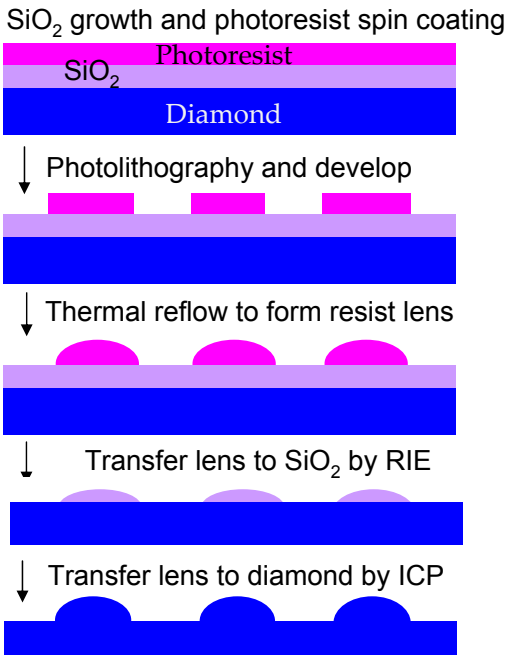

Figure 3.9: Dual-mask diamond microlens fabrication process.

Table 3.3: PECVD recipe for SiO_2 deposition.

Pressure	SiH_4 flow	N_2O flow	Platen power	Temperature	SiO_2 deposition rate
1 Torr	170 sccm	710 sccm	70 W	300 ^oC	33 nm/min

via SiO_2 as a second mask, suggesting that we can make a diamond microlens with a height 2.5 times higher than the height of the initial photoresist microlens structure. For the case of microlens fabrication using this dual-mask method, the fabrication process is shown in Figure 3.9 and the profile of the initial reflowed resist lens and the calculated profiles of the SiO_2 lens and diamond lens after etch transfer are shown in Figure 3.10.

In this work, 3 μm-thick SiO_2 was deposited by plasma-enhanced chemical vapour deposition (PECVD) on the diamond substrate. The recipe is summarized in Table 3.3. Under these conditions, the SiO_2 deposition rate is 33 nm/min. This PECVD recipe was used for SiO_2 deposition throughout this thesis.

The fabrication process of a SiO_2 microlens array (diameter is 60 μm) is similar

Table 3.4: ICP etching recipe for SiO_2 microlens fabrication.

Pressure	Ar flow	Cl_2 flow	Platen power	Coil power	Photoresist etching rate	SiO_2 etching rate
5 mTorr	25 sccm	30 sccm	200 W	600 W	500 nm/min	125 nm/min

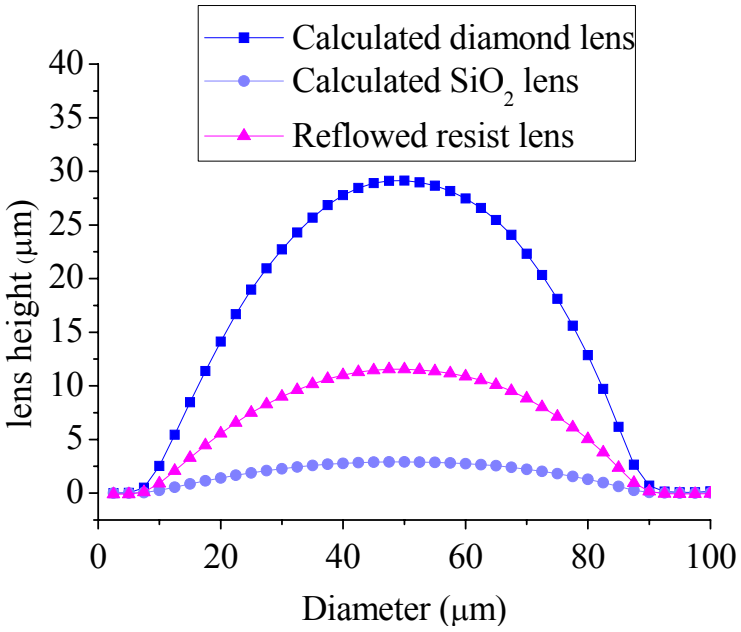

Figure 3.10: Calculated profiles of reflowed resist lens, SiO_2 lens and diamond lens.

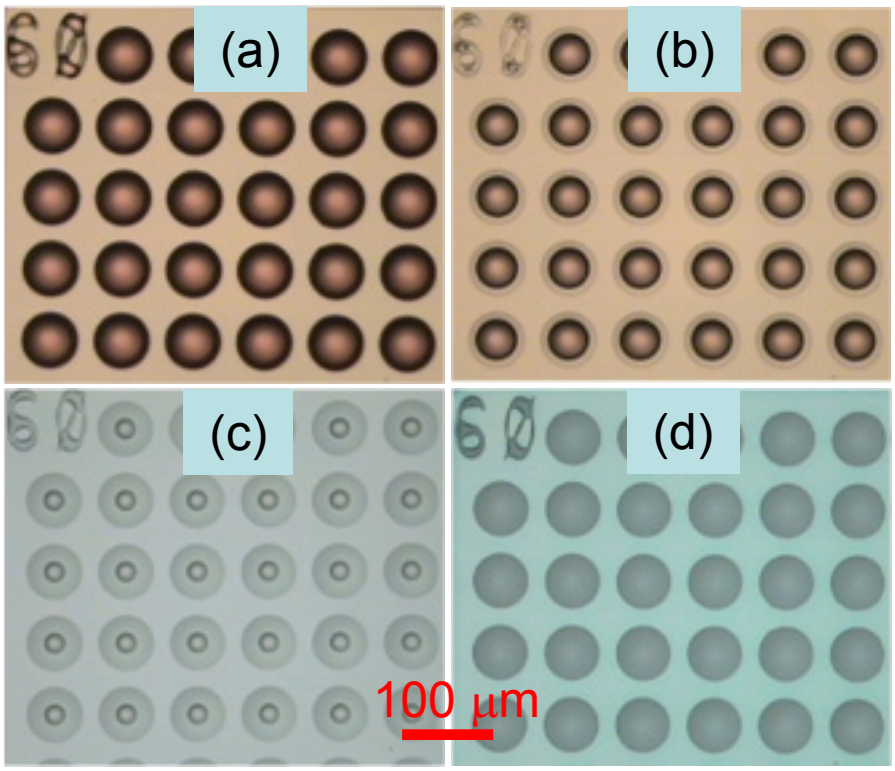

Figure 3.11: Optical microscopy images of SiO_2 lenses at different fabrication stages: (a) Photoresist after thermal reflow; (b-c-d) 10-20-30 min after ICP etching.

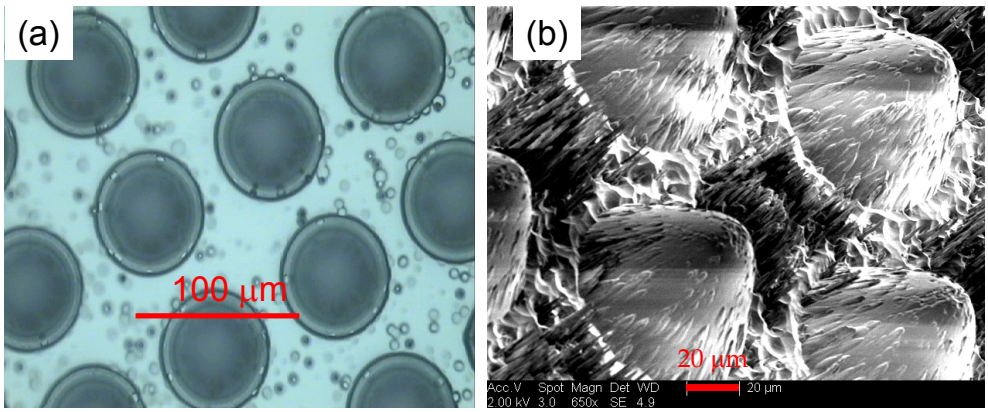

Figure 3.12: (a) Optical mircoscopy and (b) SEM images of diamond microlenses after being transfered from SiO_2 microlenses.

to the process illustrated in Figure 3.4. The reflowed photoresist lenses are shown in Figure 3.11(b). The photoresist lens pattern was transferred to SiO_2 by ICP Ar/Cl_2 etching, using the detailed recipe shown in Table 3.4. Figures 3.11(b-c-d) show the pattern transfer to SiO_2 after 10, 20 and 30 mins ICP Ar/Cl_2 etching, respectively.

These SiO_2 microlenses were further transferred to diamond by ICP Ar/O_2 etching. After the pattern transfer, we inspected the diamond microstructures using an optical microscope and the optical microscopy images are shown in Figure 3.12(a). From this image, some etching pits and damages on the diamond surface were observed. Furthermore, SEM inspection has also been conducted to check the quality of these diamond microstructures (Figure 3.12(b)). These measurements confirmed that the fabricated diamond microlenses have the desired height (30 μm). However, the structures do not have an ideal spherical shape and its surface is rough. The structural deformation may be due to the erosion of the SiO_2 hard mask during the etching process. We believe that such mask erosion may be minimized by choosing proper etching gases and optimizing the ICP powers [203].

As the resulting diamond microstructures have a lens-like shape with the expected high aspect ratio, we conclude that this method is practicable and useful for fabricating thick (or deep) diamond microstructures. However, further optimization must be undertaken especially on selecting the proper etching mask for pattern transfer. In our case, the selectivity between diamond and SiO_2 may be too high, resulting in mask erosion and structure deformation. Based on this investigation, we consider that it may be possible to fabricate smooth diamond lenses with a high aspect ratio by using a SiO_2 lens mask with a high aspect ratio and a lower selectivity etching process. This lead us to look for a SiO_2 mask with

a suitable curvature. For that purpose, colloidal SiO_2 microspheres have been chosen and the results will be presented in section 3.4.

3.4 Diamond microlens array

In this section, we present a one-step plasma etching method to create compact diamond lens arrays. This method uses a SiO_2 microsphere array as the etch mask to transfer the pattern. The monodispersed SiO_2 microspheres used have different diameters of 1, 2 and 3 μm. The methodology of SiO_2 microsphere deposition on diamond surface will be presented, followed by the description on pattern etch transfer and AFM characterization of the fabricated diamond lens array.

3.4.1 SiO_2 microsphere deposition

SiO_2 microspheres/nanospheres are a variety of colloidal particles which have size ranging between several nanometres and several millimetres. Werner Stöber *et al.* first developed a method to control the growth of monodisperse silica spheres in the micron size range in 1968 [204]. Since then, monodispersed silica colloids have been used for various applications, including natural lithography [205–207], fabrication of photonic crystals [208, 209], etc. SiO_2 spheres can form a monolayer by Langmuir-Blodgett deposition [210], spin coating [211], dip coating [212] or roll-to-roll processing [213]. These monolayer SiO_2 spheres can be etch transferred to a substrate to form micro/nano pillars, wires or cones, etc [210]. It was our intention here to use SiO_2 spheres as an each mask with a suitable recipe to fabricate compact diamond lens arrays.

In our experiment, three kinds of SiO_2 microspheres (purchased from *Bangs Laboratories, Inc.*) with diameters of 1, 2 and 3 μm were used. The main reason for choosing these sizes is that these microspheres can be observed under an optical microscope and potentially can be positioned precisely by optical trapping [214]. These SiO_2 microspheres are suspended in aqueous solution at a concentration of 100 mg/ml. The size dispersity is specified to be below 10%. The solutions were further diluted to 10 mg/ml. We used the dip coating method to obtain a monolayer of SiO_2 microspheres. Figure 3.13 shows an optical microscopy image of monodispersed 3 μm SiO_2 microspheres, which is similar to the process for spheres with diameters of 1 and 2 μm. As the excess solvent dried out, the SiO_2 microspheres remained as a monolayer and did not stack together. To achieve this monolayer deposition, we have optimized the concentration of SiO_2 microspheres,

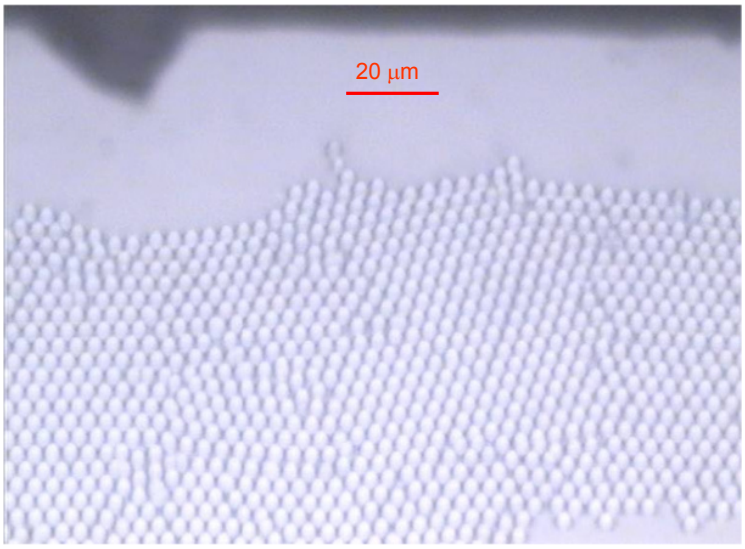

Figure 3.13: Optical microscopy image of monodispersed 3 μm SiO_2 microspheres.

otherwise the so-called rush hour effect would result in a disordered multi-layer stack [215].

3.4.2 ICP Ar/Cl_2 plasma etching

In this work, ICP Ar/Cl_2 plasma etching was used to etch SiO_2 microspheres and diamond so as to transfer the microsphere pattern to diamond. This gas mixture can produce a smooth diamond etched surface as previously demonstrated in our group [178]. First, the etchant is formed in the plasma, as expressed by:

$$e + Cl_2 \rightarrow 2Cl + e \tag{3.13}$$

This is followed with SiO_2 etching in the Ar/Cl_2 plasma [216]:

$$Si + nCl \rightarrow SiCl_x \tag{3.14}$$

and then diamond etching in the Ar/Cl_2 plasma [178]:

$$C + nCl \rightarrow CCl_x \tag{3.15}$$

During these processes, Ar ions are used for sputtering the diamond/SiO_2 surface which also facilitates the chemical reaction between etchant and diamond/SiO_2. The process produces volatile products CCl_x and $SiCl_x$ which are pumped out from the the ICP chamber. The ICP etching recipe for this process is summarized in Table 3.5. We can achieve etching selectivity of 0.5

Table 3.5: ICP etching recipe for diamond microlens fabrication using SiO_2 microspheres.

Pressure	Ar flow	Cl_2 flow	Platen power	Coil power	Diamond etching rate	SiO_2 etching rate
5 mTorr	25 sccm	40 sccm	300 W	400 W	75 nm/min	150 nm/min

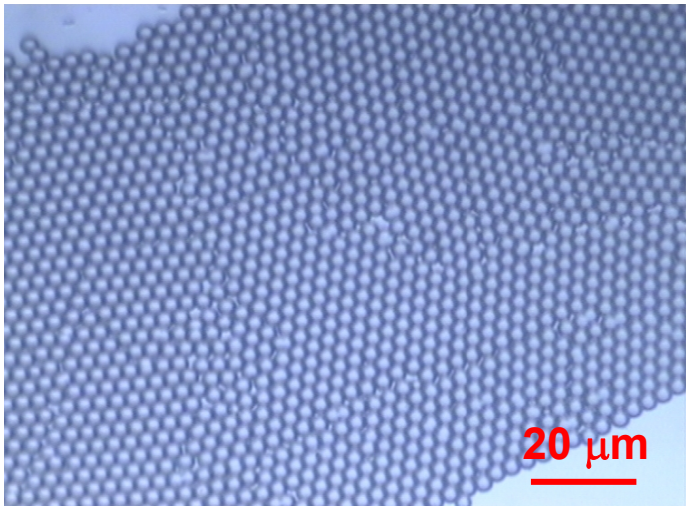

Figure 3.14: Diamond microlenses transferred from 3 μm SiO_2 microspheres.

between diamond and SiO_2 with this recipe.

After ICP etching, the etched samples are immersed in a BOE bath to make sure the resulting structures are indeed from diamond because any residual SiO_2 should be removed by BOE etching. Optical microscopy images of these etched samples were taken and are shown in Figure 3.14. It can be seen that the resulting diamond microlenses are uniform and compact, confirming that the suitability of SiO_2 microspheres as an etch mask for diamond microlens fabrication.

To have a better understanding of the etched structures, AFM measurements was conducted by using a Park Systems XE-100 Research Grade Atomic Force Microscope. Operated with a Non-Contact mode, the XE-100 is able to characterize the surface profile and roughness of the resulting diamond microstructures at nanometer scale. Such an AFM image is shown in Figure 3.15(a). This image demonstrates that the 3-μm SiO_2 microsphere structures have been successfully transferred to diamond to form a compact diamond microlens array. The measurements also show that the surface of the diamond lenses is smooth and that their sizes are uniform. These diamond lenses have a height of over 1 μm and a radius of 2 μm, giving a relatively high aspect ratio. Further optimization of the etching recipe is required however if accurate hemispherical diamond lenses are to be produced. This can be achieved by choosing the proper etching gases and

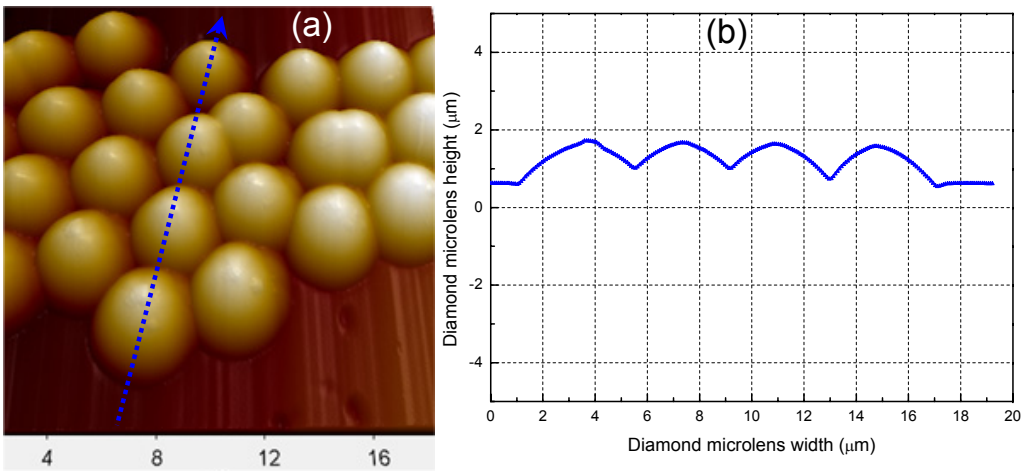

Figure 3.15: (a) AFM image of a diamond microlens array transferred from 3 μm SiO_2 microspheres and (b) a line scan profile along the blue dash line in (a)

adjusting the etch parameters so as to get suitable vertical and lateral etching rates.

3.5 Diamond micropillars

There are several methods that have been pursued to increase the extraction efficiency of a diamond colour centre, such as using a microlens, a nanowire [217] or a micropillar which is aligned properly with the colour centre. However, if such microlenses or nanowires are fabricated by electron beam lithography, the colour centre cannot be identified directly during the fabrication process, making it very difficult for alignment. The alignment can be achieved by first using an optical excitation/detection method to locate and mark a colour centre, then fabricating (e.g. by FIB or e-beam lithography) an aligned microlens or nanowire on it [170]. Clearly, the above process will be much simplified if we could develop an optical technique which combines the colour centre detection, marking and micro/nano fabrication. As similar idea has been realized in a quantum dot system, where micropillars are used to increase light extraction efficiency from the quantum dot single photon emitter which can be identified by an in-situ lithography technique [47, 218]. In this work, we proposed a micropillar fabrication method by using the in-house μLED writing setup. This optical system has capability of fabricating nanostructures and can be upgraded by combing another light source to detect and mark the colour centres in diamond so as to realize the desired alignment and nanofabrication. The writing setup can be seen in Chapter 2.

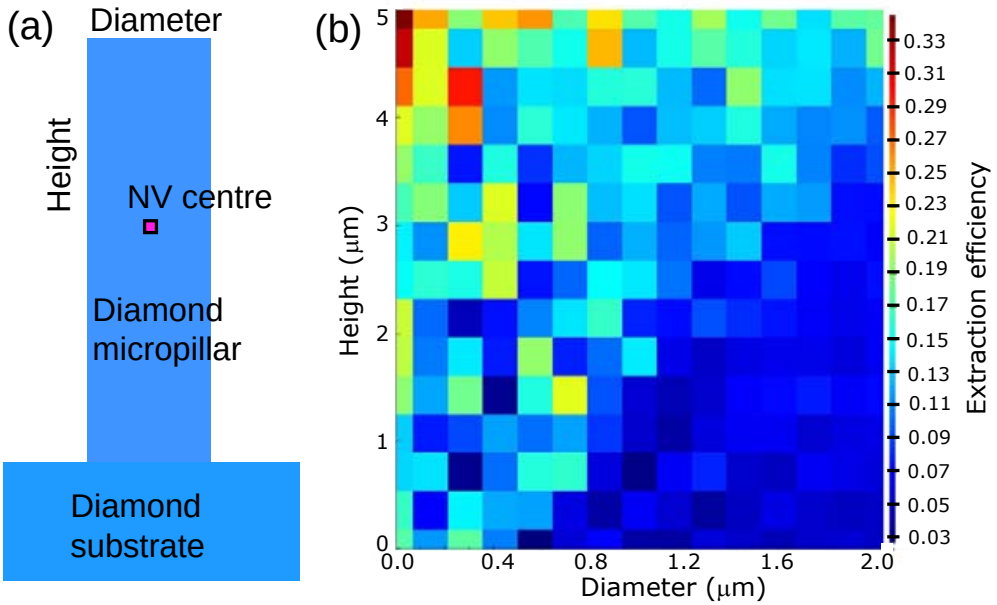

Figure 3.16: (a) Diagram of a diamond micropillar and (b) Light exaction efficiency vs. diameter and height of diamond pillars by 2D FDTD method.

3.5.1 Estimated light extraction efficiency using FDTD

3.5.2 Fabrication of diamond micropillars

We first used a commercial FDTD software (FDTD Solutions, Lumerical, trial version) to simulate the light extraction in diamond micropillars, to provide a guideline for the micropillar design and fabrication. Figure 3.16(a) shows a diagram of a diamond micropillar. In order to find the best micropillar dimensions for maximum light extraction, we mapped out the light extraction efficiency vs. the diameter and height of diamond pillars over a large range (diameter 0.1-2 μm; height 0.1-5 μm). The simulated results are shown in Figure 3.16(b). It can be seen that the larger the diameter and the smaller the height of the pillar, the lower is the light extraction efficiency. These results agree well with expectation. When there is no pillar, namely a flat surface, there won't be any improvement of light extraction efficiency.

As mentioned in Chapter 2, we have used a home-built CMOS-driven μLED writing setup to define photoresist dots on diamond. The emission of the μLED in the setup matches the absorption of negative resist maN 1405. SiO_2 was deposited prior to the writing and used as a hard mask for diamond micropillar etching. The written resist pattern was transferred to SiO_2 by RIE first and subsequently to diamond by ICP etching.

To study the micropillar's diameter as a function of μLED size and expo-

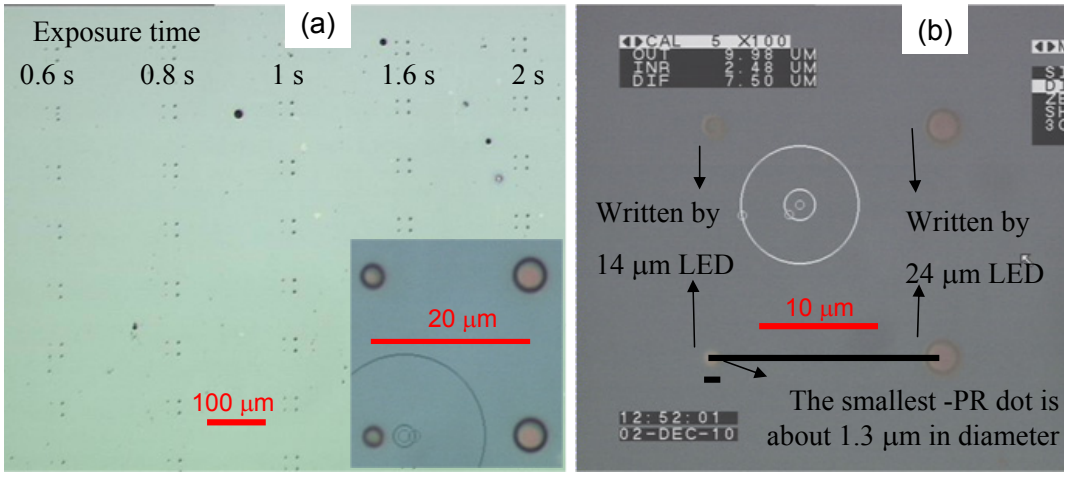

Figure 3.17: (a) Optical microscopy images of μLED written photoresist dots with exposure time ranges from 0.6 s to 2 s and (b) the enlarged image of a group of four photoresist dots using 4 μLEDs under 0.6 s exposure.

sure time, we used 4 μLEDs with two different diameters (14 and 24 μm) named 14μLED1, 14μLED2, 24μLED1 and 24μLED2, respectively. These 4 μLEDs are used for exposure in parallel. Exposure times are 0.6, 0.8, 1, 1.6 and 2 seconds, respectively. For each exposure time, we did 10 exposures to get the average dot size. Figure 3.17 shows the typical resist dots written by these 4 μLEDs with different exposure times. All the photoresist dot images are processed by a home-built Matlab^{TM} code in order to determine the diameter of the individual dots. Based on the processed data, we can get the average diameter and standard derivation of the photoresist dots using the same μLED under the same exposure time. These data are plotted in Figure 3.18. These results show how the average photoresist dot diameter changes with the exposure time. Clearly, the longer the exposure time, the larger the dot size. Pixels 24μLED1 and 24μLED2 give almost identical dot sizes while the photoresist dots generated from 14μLEDs are different. This indicates that the uniformity of 14μLEDs is not yet satisfactory and further improvement of the uniformity of the μLED illumination is required so as to achieve uniform multiple LED beam writing for micro/nano pillar fabrication.

A 0.6s exposure time gives an average pillar diameter of 2.34 μm and 1.72 μm by using 14μLED1 and 14μLED2, respectively. This size is not sufficient for dramatic improvement of NV center light extraction and thus further work is required.

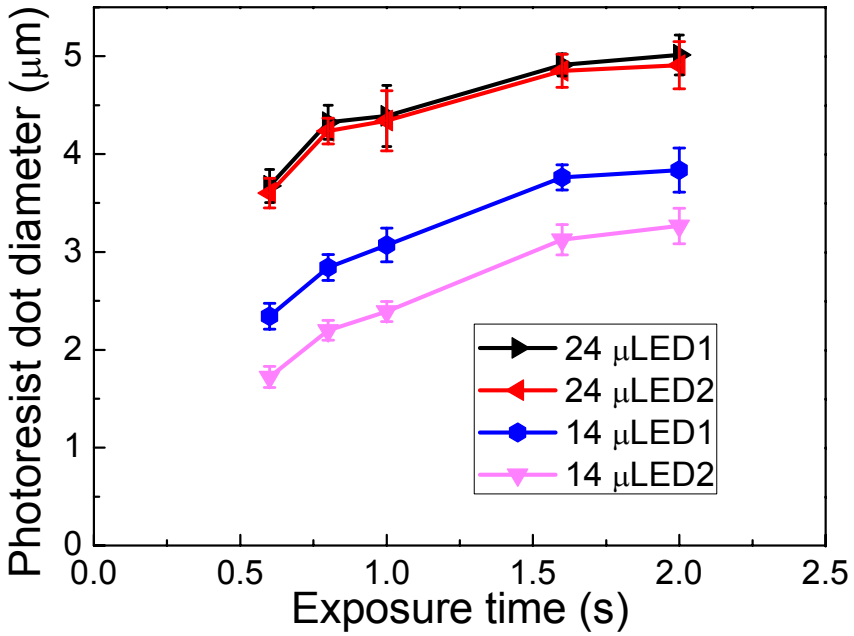

Figure 3.18: μLED written photoresist dots: average diameter vs exposure time. The error bars are shown in the figure.

3.6 Summary

In summary, the main work described in this chapter is to develop novel diamond micro-optical components including diamond microlenses with a high aspect ratio and diamond micropillars. One of important applications of these diamond micro-optical components is to integrate them with diamond colour centre, which is a room-temperature single photon source, to achieve high light extraction. To do so, various micro-fabrication techniques including dual-mask etching, pattern transfer using SiO_2 microspheres and μLED direct writing have been developed. We have proposed and demonstrated that diamond high aspect ratio microlenses can be made using dual-mask and SiO_2 microspheres. The SiO_2 microspheres can make diamond microlens array in a single etching step and could be a strong candidate for diamond microlenses fabrication.

Chapter 4

Diamond waveguides

The objective of the work presented in this chapter is to develop diamond rib waveguides which could be the building blocks of an all-diamond integrated quantum photonic circuit. There are five sections in this chapter. Section 4.1 presents a literature overview of diamond waveguide research and a general introduction and design guideline for large cross-section rib waveguides. We first tried to fabricate diamond waveguides by using standard lithographic processes. However, some fabrication issues occurred and the reason for these issues is analyzed in Section 4.2. To address these issues, photoresist inkjet printing method was developed and in this way, edge coupled diamond rib waveguides were successfully fabricated (see Section 4.3). The diamond rib waveguides underwent optical waveguiding tests which are presented in Section 4.4. Section 4.5 is a brief conclusion.

4.1 Diamond photonic structures

To make a rib waveguide (see Chapter 1), there are two basic conditions that need to be satisfied. First, the waveguide material requires a higher refractive index compared to its surroundings, meaning that there must be a refractive index contrast in order to make a waveguide. Second, a suitable rib structure needs to be designed and etched. In the first subsection, we will review the methods reported in the literature on how to create a refractive index contrast in diamond. Then, the design we used to make rib waveguides is presented in the second subsection.

Table 4.1: Summary of changing refractive index of diamond by ion implantation.

Year	Group	Institution	Material	Fabrication techniques	Structures and references
1965	R. L. Hines	Northwestern University	Diamond from H. B. Dyer	20 KeV C^+, anneal in argon atmosphere	Typical increase in refractive index of 0.1 [223]
2010-2011	E. Vittone	University of Torino	Type IIa E6	2 and 3 MeV protons microbeam	Maximum variation of the refractive index is 0.1 [224, 225]
2010	S. Lagomarsino	University of Firenze	Type IIa E6	2 and 3 MeV proton microbeam	Waveguiding in ion implanted diamond [226]
2012	E. Vittone	University of Torino	Type IIa E6	180 KeV B^+	Up to 5% increase in refractive index [227]

4.1.1 Literature review

There are several methods of creating a refractive index contrast in a diamond photonic structure. Among them, one is to grow diamond on a lower refractive index material (e.g. SiO_2). At the current stage, however, this growth technique can only produce microcrystalline diamond which is not quite suitable for waveguide fabrication and applications (see Section 4.2). Diamond grown on silicon can have a nanocrystalline structure which could have better optical performance than microcrystalline diamond; however, silicon has a higher refractive index than diamond, meaning that light cannot then be confined in a conventional waveguide structure. We note that there are a few reports on the heteroepitaxial growth of single crystalline diamond recently [219] and this will be reviewed at the end of this subsection.

Another method to generate a refractive index contrast is to use an ion implantation process. The ion implantation method can be used to change the physical, chemical, or electrical properties of a solid and has wide applications in the semiconductor industry. Ion implantation has been used in diamond as well and such work was presented in Refs. [220–222] and the references therein. Ion implantation can either change diamond's refractive index directly or make thin diamond membranes for further waveguide fabrication. The reported results on these methods are summarized in the following.

The first approach is to use ion beam to change the diamond refractive index

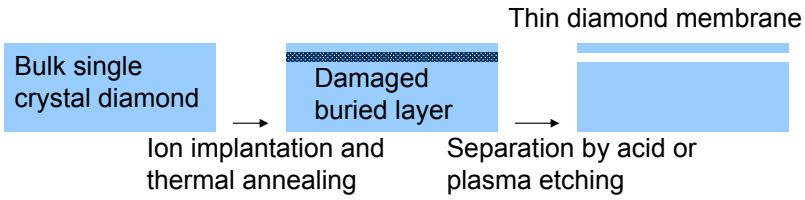

Figure 4.1: Process flow of diamond membrane made by ion implantation.

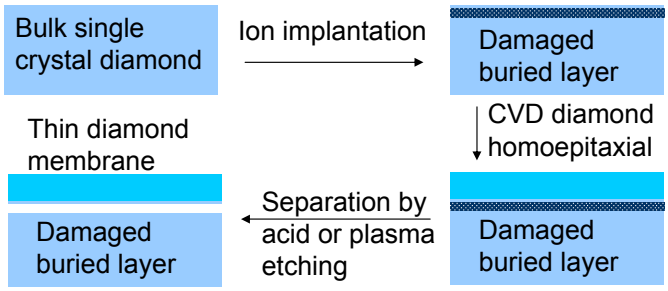

Figure 4.2: Process flow of diamond membrane made by ion implantation and post CVD diamond growth.

directly, a literature review of which is summarized in Table 4.1. The first report is from R. L. Hines who obtained an increase of 0.10 in refractive index of diamond after 20 KeV C^+ ion implantation [223]. A very recent paper is from Ettore Vittone's group, in which they reported that 80 KeV B^+ ion implantation caused considerable increase in refractive index (up to 5%) [227]. Similarly, proton microbeams were also used for diamond refractive index modification [224, 225] and waveguiding has been demonstrated in a diamond channel written by a microbeam [226].

The ion beam can also be used to graphitize diamond at a certain depth so as to make a thin free-standing diamond membrane in the range of several hundred nanometres to a few microns. The general procedure of this method is shown in Figure 4.1. First, MeV C^+ or O^+ ions are used to create a buried damaged layer in a bulk diamond. Then, through thermal annealing and acid/plasma etching, a submicron thick thin membrane can be separated from the bulk diamond. Reported work on this topic is summarized in Table 4.2. Diamond membranes as thin as 210 nm were reported and various structures including microrings [234], rib waveguides [237] and photonic crystal structures [231] have been fabricated on these membranes.

In combination with CVD growth, the above method has been further developed as shown in Figure 4.2. First ion implantation is used to graphitize diamond in a shallow depth in a bulk diamond, followed by CVD homopitaxial diamond

Table 4.2: Summary of photonic structures made on diamond membrane ion implantation.

Year	Group	Institution	Diamond bulk sample	Ion implantation	Separation process	Membrane thickness and structures with references
1988	M. W. Geis	Massachusetts Institute of Technology	Single crystal	Ion implantation	Thermal annealing, hot CrO_3/H_2SO_4 solution or molten KNO_3 etching	Thin membrane [228]
1992	N. R. Parikh	University of North Carolina	Dubbledee Harris type Ia and IIa	4-5 MeV C^+ or O^+	Thermal annealing in vacuum	Curled 1-2 μm $\times$ 4 mm $\times$ 4 mm large area membrane [229]
1995-2011	R. Kalish	Technion, Haifa, Israel	Single crystal	60 KeV B or 320 KeV B; 1.8 MeV or 2 MeV He_+	Wet etching, FIB	Damage threshold [230], 320 nm thick membrane and photonic crystal [231]
1995-2012	S. Prawer	University of Melbourne	Type Ib Sumitomo HPHT	2 MeV He^+	Thermal annealing, FIB with 30 keV Ga^+ ion beam	Diamond transformation [221], 3.0 μm thick membrane [232], 3D multimode waveguide [233], 210 nm thick membranes and microring [234], X-ray study [235]
2008-2011	F. Ladouceur	UNSW, Sydney	Type Ib Sumitomo HPHT	2 MeV He^+	FIB with 30 keV Ga^+ ion beam, Photolithography, RIE	Multimode rib waveguides [236], millimetre length waveguide [237]
2011	E. Bustarret	CNRS Institut Neel	Type Ib Sumitomo HPHT	240 KeV O^+	Acid lift-off, H_2 plasma at 950 ^{o}C	280 nm thick membrane with subnanometer smooth surface [238]

Table 4.3: Summary of photonic structures on thin diamond membrane made by ion implantation and CVD diamond post growth.

Year	Group	Institution	Diamond	Ion implantation	CVD growth	Separation process	Membrane thickness and structures with references
1993	Y. Tzeng	Auburn University	Sumitomo	3.5-5 MeV O^+	MWCVD	Thermal annealing in O_2 at 600 ^oC	Flat 15 μm thick membrane [239]
1993-1994	D. Moses	Naval Research Laboratory	Sumitomo	175 KeV C^+	MWCVD	Thermal annealing, electrochemical etching	15 μm thick membrane [240]
1994	J. D. Hunn	Oak Ridge National Laboratory	Dubbledee Harris type Ia	4-5 MeV C^+, O^+	CVD	Annealing, hot CrO_3/H_2SO_4 solution, 193 nm ArF laser ablation	13 μm thick membrane, 12 tooth gear [241]
1996	J. B. Posthill	Research Triangle Institute	Type Ia natural	190 KeV C^+	CVD	Annealing in N_2, electrochemical etching, hot CrO_3/H_2SO_4 etching	17.5 μm thick membrane [242]
2007	E. Hu	UCSB	Sumitomo HPHT	180 KeV B^+	CVD	Electrochemical etching	300 nm thick diamond with an airgap of 150 nm [243]
2011-2012	E. Hu	Harvard	Type IIa E6	1 MeV He^+	CVD	Electrochemical etching, boiling acid, ebeam, ICP	200 nm thick membrane [244], 500 nm thick membrane and 2.5 μm diameter microdisk [245, 246]
2008-2011	S. Shikata	AIST, Japan	Sumitomo HPHT	180 KeV or 3 MeV C^+	CVD	Electrochemical etching	0.4 mm thick plate [247], 0.47 mm thick diamond [248], 25 mm square plate [249]
2011	B. B. Pate	Naval Research Laboratory	Sumitomo HPHT	180 and 150 KeV C^+	CVD	Electrochemical etching or H_2 plasma, FIB	175 nm thick membrane [250], 75 nm thick membrane [251]
2010-2011	M. Liao	NIMS, Namiki	HPHT	180 KeV O^+	MPCVD	UHV annealing, EBL, RIE, boiling acid etching	Suspended bridge [252], NEMS device [253]

Table 4.4: Summary of photonic structures on commercial thin diamond platelet.

Year	Group	Institution	Diamond	Fabrication process	Structures with references
2011	E. Gu, M. D. Dawson	University of Strathclyde	20 μm thick type Ib DDK	Inkjet printing, Photolithography, ICP	Large cross-section end coupled rib waveguides [127]
2011-2012	A. Faraon	HP Laboratories	5 μm thick type IIa E6	RIE, EBL	280 nm thick membrane, multimode ring resonators [254], photonic crystal [255]
2011	M. Lončar	Harvard University	20 μm thick type Ib E6	ICP etching, EBL	250 nm thick membrane, Ring resonator coupled to an optical waveguide [256]
2012	R. L. Walsworth	Harvard University	0.2 mm thick CVD Apollo	As purchased	TIR between polished planar surfaces [257]

growth. By using thermal annealing and acid/plasma etching, the thin diamond membrane which is mainly the epitaxially grown diamond layer can be separated. Reported work on this topic is summarized in Table 4.3. By this method, the diamond membrane thickness is largely controlled by the post homoepitaxial growth and membranes with varied thicknesses ranging from 75 nm [251] to 0.47 mm [248] have been reported. Diamond micro-disks [245, 246], micro-domes [250, 251] and suspended bridges [252] have been fabricated on these thin membranes as well.

The thin diamond platelets can also be made by mechanical grinding and polishing. Such polished thin diamond platelets (5 to 20 μm thick) are commercially available recently. Rib waveguides [127], diamond micro-rings [254], photonic crystals [255] and integrated diamond photonic circuits [256] made on such diamond platelets have been reported. These works are summarized in Table 4.4.

There are other techniques which can be used for fabricating photonic structures on diamond directly e.g. 3 dimensional FIB milling [258] [259]. By using FIB milling, photonic crystals were also made on heteroepitaxial grown single crystal diamond. Details of this work are shown in Table 4.5.

Table 4.5: Summary of photonic structures made by 3D FIB milling and heteroepitaxial growth.

Year	Group	Institution	Diamond	Fabrication process	Structures with references
2008	Rarity, J.G	Bristol University	E6 diamond	3D FIB milling	L3 photonic crystal [260]
2010-2011	R. Kalish	Technion, Haifa, Israel	Single crystal diamond	3D FIB milling, H_2 plasma	2 μm wide bridge [261], Triangular nanobeam Photonic crystal [258]
2011	M. Loncar	Harvard University	Single crystal diamond	3D FIB milling	150 or 200 nm thick diamond bridge and nanobeam cavity [259]
2012	C. Becher	Saarland University	CVD diamond on Ir/YSZ/Si [262]	DRIE, RIE, FIB milling, acid treatment	300 nm thick membrane and photonic crystal [219]

4.1.2 Diamond rib waveguide design

As presented in Chapter 1, in this work, diamond and GaN waveguides with a large cross-section rib structure were developed. Klaus Petermann investigated the geometrical conditions required to enable the realization of large cross-section single-mode rib waveguides in 1976 [263]. However, it was not generally accepted at that time that a single mode rib waveguide structure can be several microns in lateral dimension. Richard A. Soref *et al.* revisited this topic in 1991 and gave a normalized equation to determine the necessary cross-section dimensions for a single-mode rib waveguide structure [264]. This equation is now widely used:

$$\frac{a}{b} \leq 0.3 + \frac{r}{\sqrt{1-r^2}} \quad (\text{assuming} \quad 2b\sqrt{n_1^2 - n_2^2} \geq 1) \tag{4.1}$$

where a, b, r, n_1 and n_2 are defined in Figure 4.3, (for the case of diamond on Silica) and λ is the free space wavelength of light. There were several following discussions on this topic [265–268]. It is now generally accepted that a large cross-section single mode waveguide is possible and many demonstrations have been made on Silicon-on-Insulator (SOI) [269], Si-Ge system [264], etc .

In this chapter, we first designed rib waveguides based on commercially available 20 μm thick free-standing natural diamond platelets with a 2 mm $\times$ 2 mm

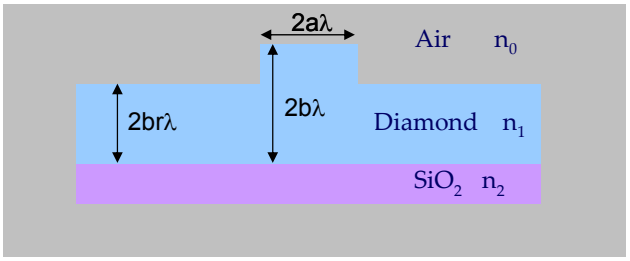

Figure 4.3: Diamond waveguide design schematic. Parameters of a, b and r are used in Equation 4.1. λ is the free space wavelength of light. n_0, n_1 and n_2 are refractive indices of air, diamond and silica, respectively.

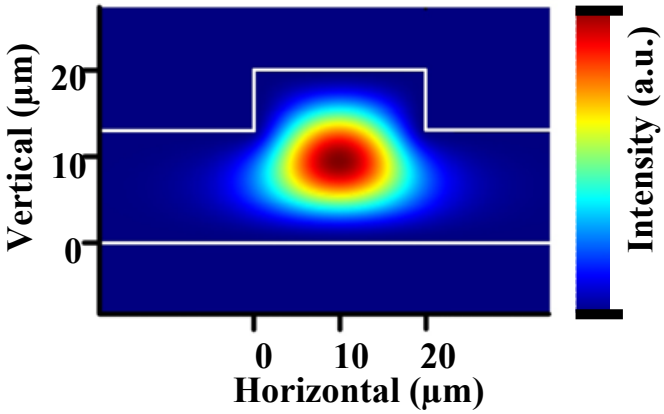

Figure 4.4: FEA simulation of large cross-section diamond rib waveguide

square shape. The thin diamond plates were purchased from *Delaware Diamond Knives (DDK), Inc.* The design of these rib waveguides takes advantages of relaxed dimensional requirements for single mode behaviour following the criteria in Equation 4.1 which have been applied to silicon-based materials [264]. Such a waveguide cross-sectional structure is shown in Figure 4.3.

Our design is based on the following parameters: (i) the upper cladding is air and the lower cladding is SiO_2; (ii) the refractive indices (at 632 nm) of diamond and SiO_2 (lower cladding) are 2.41 and 1.46, respectively; (iii) the operation wavelength is set at 632 nm which is the wavelength of the He-Ne characterisation laser and is also close to the emission wavelength of a diamond NV centre (637 nm).

Two-dimensional finite element analysis (FEA) [270] was carried to calculate the intensity profile of the guided mode in the rib waveguide structure. Based on this 20 μm-thick diamond platelet with rib width of 20 μm and rib etching depth of 6.7 μm, the calculated intensity profile is shown in Figure 4.4. Our simulation

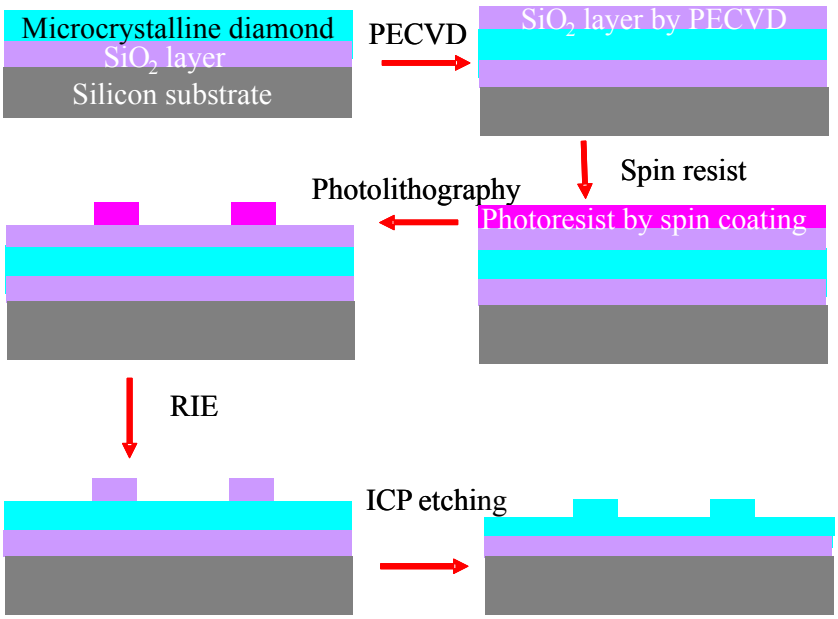

Figure 4.5: Fabrication process of microcrystalline diamond rib waveguides.

confirms that single mode operation can be sustained in the large cross-section diamond waveguide with the designed structure and parameters.

4.2 Microcrystalline diamond waveguide

4.2.1 Fabrication process

As a first attempt, we started diamond waveguide fabrication by using microcrystalline diamond. The microcrystalline diamond sample was grown on a SiO_2/Si substrate by chemical vapour deposition (CVD) technique (purchased from *sp3 Diamond Technologies*). The SiO_2 layer has a lower refractive index, hence providing the confinement in the diamond waveguide.

The waveguide fabrication process is illustrated in Figure 4.5. SiO_2 was chosen as a mask material since it is commonly used for diamond patterning. In particular, SiO_2 permits us to take advantage of the high etching selectivity of diamond over SiO_2 in Ar/O_2 plasma used for diamond etching. A layer of 500 nm thick SiO_2 was first deposited by plasma-enhanced chemical vapour deposition (PECVD) on diamond. Photoresist S1805 was then spin-coated at a speed of 4000 rpm, producing a 500 nm thick photoresist layer. The photoresist exposure time was 2.5 s. Then Reactive Ion Etching (RIE) was used to etch the patterned SiO_2. The typical RIE etching recipe for SiO_2 is summarized in Table 4.6. This RIE recipe gives a suitable selectivity ($\sim$4 between SiO_2 and S1805), the mea-

Table 4.6: RIE recipe for SiO_2 etching and etching rate of SiO_2/S1805.

Pressure	Ar flow	CHF_3 flow	Platen power	SiO_2 etching rate	S1805 etching rate
66 mTorr	15 sccm	5 sccm	200 W	41 nm/min	10 nm/min

Table 4.7: ICP recipe for diamond rib waveguide and etching rate of diamond/SiO_2 .

Pressure	Ar flow	O_2 flow	Coil power	Platen power	Diamond etching rate	SiO_2 etching rate
5 mTorr	15 sccm	40 sccm	1200 W	300 W	280 nm/min	30 nm/min

sured etch rates of SiO_2 and S1805 under these etch conditions are 41 nm/min and 10 nm/min, respectively.

After RIE etching, the photoresist was stripped by dipping the sample into acetone and menthol and a subsequent DI water rinse. After drying, the sample was put into the ICP chamber for diamond etching. The ICP etching recipe is shown in Table 4.7. This ICP recipe gives a suitable selectivity ($\sim$10 between diamond and SiO_2), the etch rates of diamond and SiO_2 under these etch conditions are 280 nm/min and 30 nm/min, respectively.

During each fabrication stage, optical microscopy images were taken. Figure 4.6(a) shows the photolithographic resist lines on SiO_2/diamond/SiO_2/Si. Figure 4.6(b) and inset are the SiO_2 lines on diamond/SiO_2/Si after RIE etching and residual resist stripping. Figure 4.6(c) and its inset are the microcrystalline diamond lines on diamond/SiO_2/Si after ICP etching.

SEM images of etched microcrystalline diamond waveguides are shown in Figure 4.7. The length of the waveguide structure is longer than 4 mm. The space between two waveguides is 500 μm which is big enough for optical measurements. It can be seen from Figure 4.7 (b), however, that the sidewall of the rib structure is rough, which is due to the selective etching at the grain boundaries of the microcrystalline diamond and the zigzag edge of resist pattern is again owing to the roughness of microcrystalline diamond. These structural results show that the microcrystalline diamond waveguides are not suitable for light coupling and propagation.

4.2.2 Challenges and issues using conventional process

From the above results, we considered that single crystal diamond would be required to produce waveguides with good optical quality. Thus, we decided to

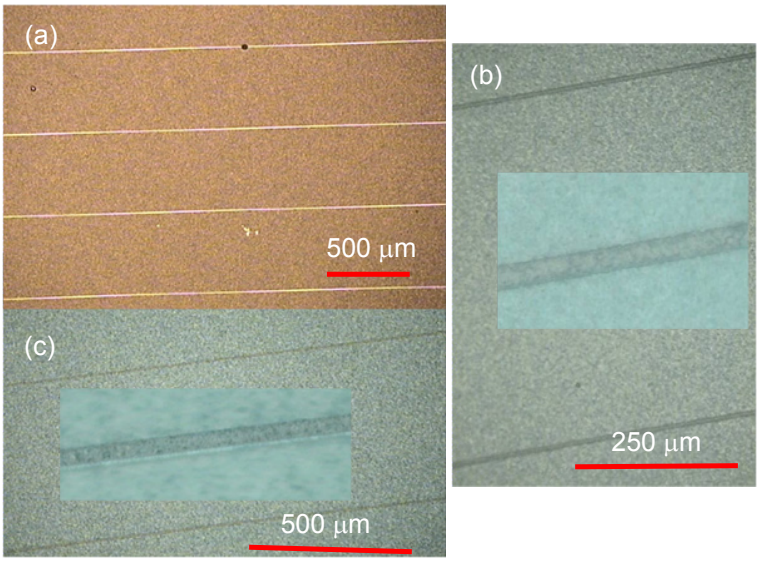

Figure 4.6: Images of microcrystalline diamond rib waveguides during the fabrication process. (a) photolithographic resist lines on SiO_2/diamond/SiO_2/Si, (b) SiO_2 lines on diamond/SiO_2/Si after RIE etching and residual resist stripping with an enlarged image as inset, and (c) microcrystalline diamond lines on diamond/SiO_2/Si after ICP etching with an enlarged image inset.

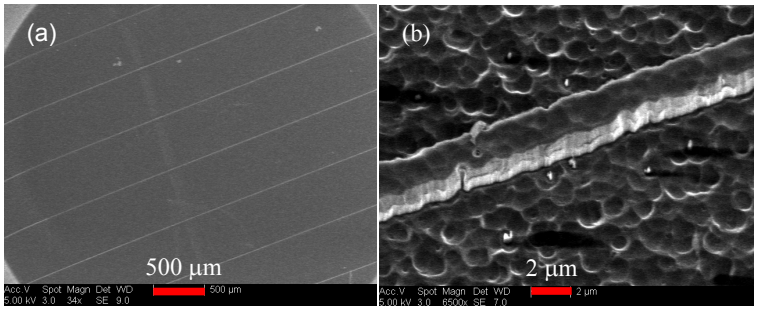

Figure 4.7: SEM images of microcrystalline diamond rib waveguides after the fabrication process: (a) small and (b) large magnifications.

fabricate waveguides on bulk single crystal diamond first to test the fabrication process and to check the structural properties. The fabrication process is similar to that used for the microcrystalline diamond waveguides shown in Figure 4.5.

As shown in Figure 4.8, the sidewall of a single crystal diamond waveguide is much smoother compared to that of a microcrystalline diamond waveguide. This confirms that single crystalline diamond is more suitable for making optical waveguides. However, because of the thickness of the bulk diamond used and lack of lower confinement material, it was not expected that this sample would have a waveguiding effect. There is also a technical issue regarding the optical coupling. There are several ways to couple light into a waveguide, such as

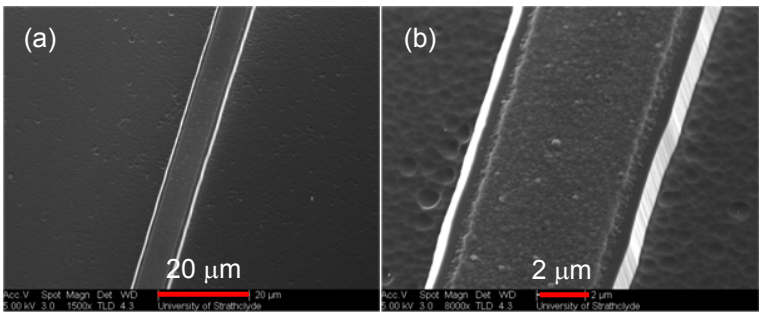

Figure 4.8: SEM images of single crystalline diamond rib waveguides after the fabrication process: (a) small and (b) large magnifications.

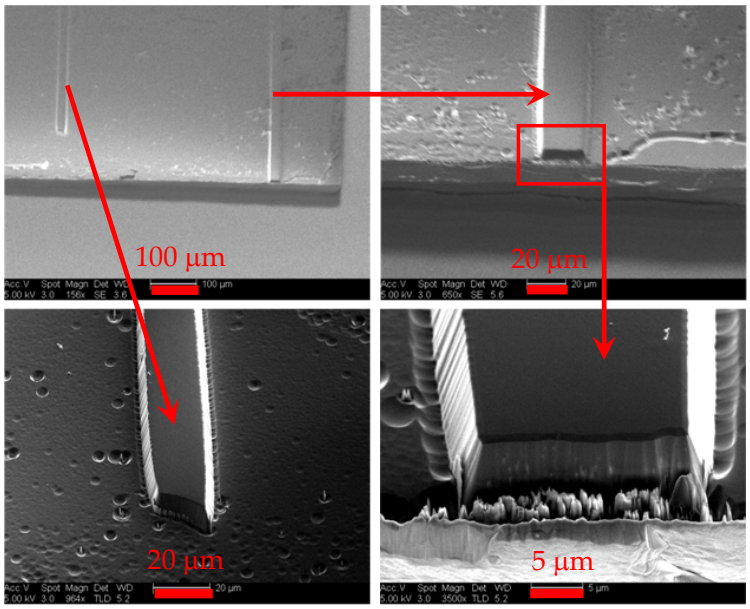

Figure 4.9: SEM images showing edge effect for single crystal thin plate diamond rib waveguides.

prism coupling, grating coupling, and end-coupling. Among them, we chose end-coupling since it is the most steady and straightforward method and is also widely used in integrated quantum photonics measurement. This method requires that all waveguide structures must extend to both ends of the substrate. However, due to the edge bead effect in spin-coated photoresist as described in Chapter 2, the fabricated waveguide structure cannot be extend to the edge of the diamond sample. Using a thin diamond plate could reduce the edge effect. Nevertheless, it was found that the waveguide structure made on a thin diamond plate still cannot reach the real edge of the substrate as shown in Figure 4.9. Another possible way is to cleave the diamond substrate after waveguide fabrication. As diamond is an extremely hard material, it is very difficult to apply this method to realize

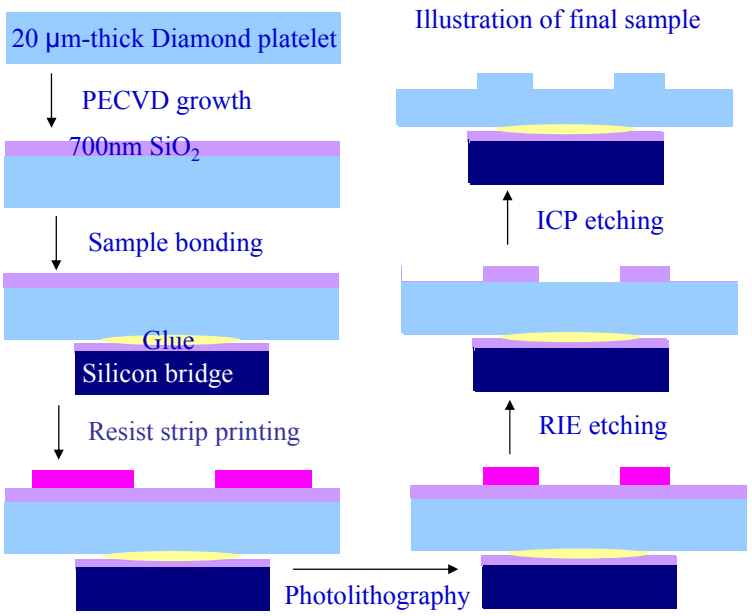

Figure 4.10: The fabrication process flow of the thin (20 μm) diamond waveguides.

an ideal waveguide edge for light coupling.

In this work, an innovative method has been proposed and developed to overcome the problem. This method uses an inkjet printer to deposit photoresist drop by drop to reach the diamond sample edges, thus removing the edge effect caused by spin coating. By this new technique, we have fabricated end-coupled diamond waveguides on a small (2mm x 2 mm) diamond platelet successfully. The detailed fabrication method and process will be introduced in the following section.

4.3 Fabrication of single crystalline diamond waveguides

The fabrication process flow of the diamond waveguides is shown in Figure 4.10. In this section, 2mm x 2mm thin (20 μm) single crystalline diamond platelets were used. A 700-nm-thick SiO_2 mask layer was first deposited using PECVD. After deposition, the diamond thin platelet was glued on a narrow silicon support bridge using Norland 81 optical adhesive. Prior to the bonding, a 700-nm-thick SiO_2 layer was deposited on the surface of the silicon bridge. Both the Norland 81 optical adhesive (with refractive index of 1.56) and the SiO_2 layer on the silicon bridge have a lower refractive index than that of diamond. Thus they can provide vertical light confinement. The narrow silicon bridge gives good lateral access to

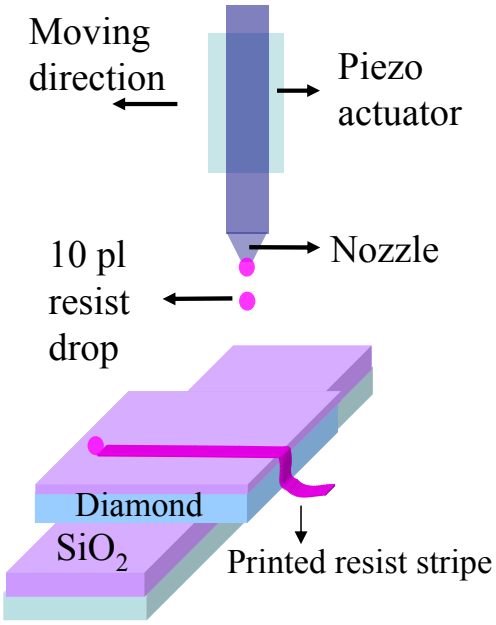

Figure 4.11: A schematic diagram of the inkjet printing setup. The piezo actuator controlled inkjet printing nozzle generated 10-pl resist drops one by one to form a continuous stripe on the PECVD grown SiO_2 mask.

the waveguide ends, allowing us to couple light directly from the sample edges.

4.3.1 Photoresist deposition using an inkjet printer

The next step is to create photoresist patterns on top of the SiO_2 mask layer, which was achieved by inkjet printing and subsequent standard photolithography. The inkjet printing is a droplet-based deposition method [271] and can successfully avoid the edge effect caused by spin coating process. The inkjet printer (Dimatix DMP-2800) was used in this work and this method of deposition have been introduced in Section 2.1.2 of Chapter 2. Photoresist S1805 was used and filled into a 10-pl cartridge of the inkjet printer. A schematic diagram of the specific inkjet printing process used here is shown in Figure 4.11. Under the control of a piezo actuator, the inkjet printing nozzle generated 10-pl photoresist drops one by one. By carefully choosing the spacing of printed photoresist drops, a continuous photoresist stripe was formed on the SiO_2/diamond substrate.

Owing to the 'coffee stain' effect [146] described earlier, the printed photoresist stripes have a cross-section shape with a lower height in the centre which is clearly not suitable for subsequent photolithographic patterning to define the waveguide structure. To overcome this problem, we investigated the dependence of the profile of the printed photoresist stripes with increasing number of the printed

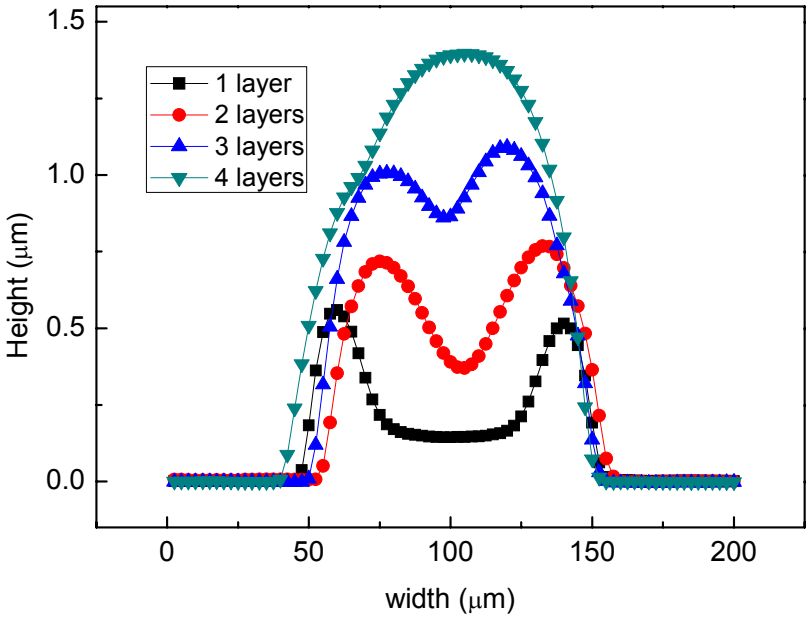

Figure 4.12: The surface profilometer measurements of the cross-section of four samples with 1 to 4 layers of printing photoresist.

layers. A sample with four different stripes consisting of respectively 1, 2, 3 and 4 photoresist layers was produced. After printing, the sample was baked at 130 ^oC for 2.5 min. The cross-sections of the four stripes were measured by a Surface Profile Measuring System and shown in Figure 4.12. We can see that the 1-layer stripe has an obvious lower height at the center and by increasing the printing layer number, the central thickness of the photoresist increases rapidly, eliminating the coffee stain effect successfully.

4.3.2 Diamond waveguide fabrication

Figure 4.13 shows the printed 4-layer photoresist stripes. The stripe is about 1.5 μm high and 100 μm in width. In order to obtain a mask with dimensions consistent with the actual design, the printed resist stripes were subsequently narrowed by standard photolithographic techniques, employing a Karl Suss MA-6 contact mask aligner. In this way, well-defined photoresist stripes with a width ranging from 2 μm to tens of microns could be fabricated. As we can see from the images, these narrow photoresist stripes are well-defined, uniform and they extend to the very edge of the sample.

Reactive ion etching (RIE) was then applied to transfer the photoresist pattern to a SiO_2 mask. Finally, by using ICP etching, the pattern was further transferred into diamond to realise large cross-section edge-coupled diamond waveguides.

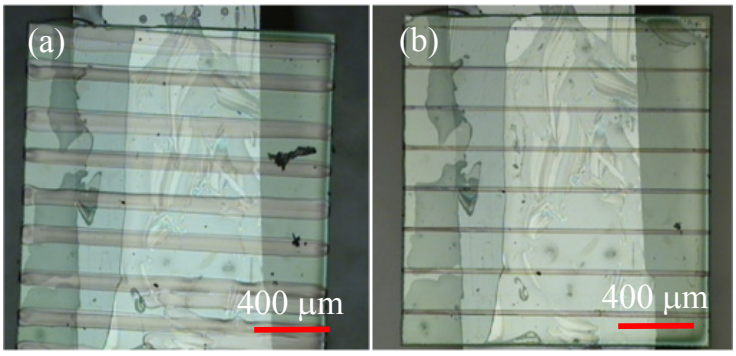

Figure 4.13: Optical microscopy plan-view pictures of (a) the printed resist stripes and (b) the corresponding photolithographic resist lines.

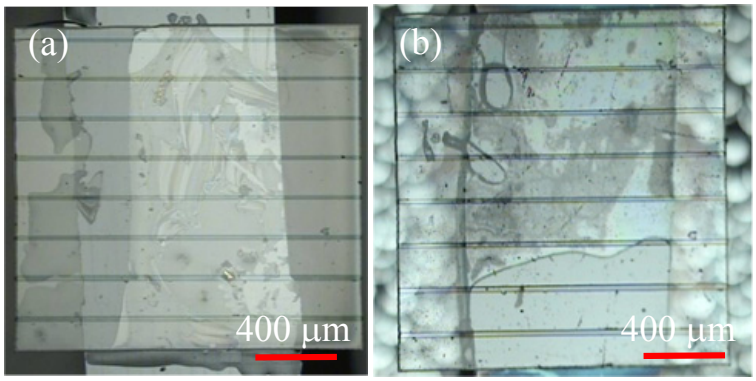

Figure 4.14: Optical microscopy plan-view pictures of diamond waveguide fabrication after (a) RIE and (b) ICP etching.

Figures 4.14(a) and 4.14(b) show the fabricated diamond waveguides after RIE and ICP etching, respectively. A coil power of 1200 W was used to achieve an etched height of 7 μm, consistent with the design parameter, was reached in 25 minutes.

The structures of the fabricated waveguides were measured using a surface profilometer and a Scanning Electron Microscope (SEM). The results are represented respectively in Figure 4.15(a) and its inset. As shown, the waveguide rib extends up to the edges of the sample and its cross-section is in agreement with the chosen design specifications. From the SEM image, the slope angle (as defined in Figure 4.15) of the diamond waveguide was measured to be about 74^o. Additionally, the roughness observed on the edge facet only reflects the quality of the commercially supplied polished platelet since these (side) surfaces remained unaffected by subsequent sample handling and waveguide processing steps. It was noticed that the etched (top) surface presents some common etch pits (highlighted in Figure 4.15(a) inset) and trenches (highlighted in Figure 4.15(b)). These etch-

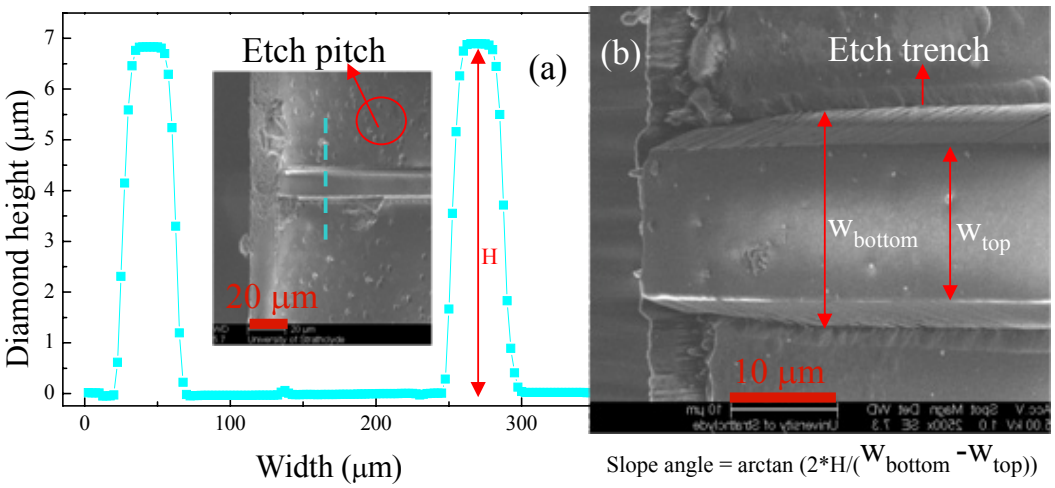

Figure 4.15: (a) Surface profile of fabricated diamond waveguide and inset is a SEM image of the resulted sample. (b) A high magnification SEM image of diamond rib waveguide highlighted the etching trench.

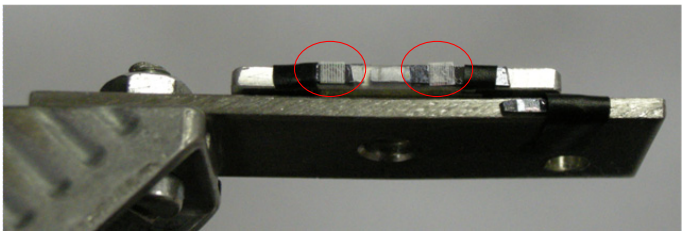

Figure 4.16: Diamond waveguide samples on Al slide (edge view). Two samples are highlighted in red circles in the image.

related defects and surface roughness can be reduced by further optimizing etching parameters and processes [178]. Here again, readily-achievable improvements in the platelet preparation and fabrication process would lead to waveguides of enhanced quality and characteristics.

4.4 Optical characterization of the waveguides

4.4.1 Optical characterization setup

After fabrication, the optical guiding characteristics of these diamond waveguides were tested. To assist optical coupling, the diamond waveguide sample was bonded on the sidewall of thin a Al slide which was connected to a translation stage. Figure 4.16 shows two diamond waveguide samples (highlighted by red circles) sitting on the thin Aluminum (Al) slide. Figure 4.17 is a schematic diagram showing the setup for diamond waveguide characterization. A He-Ne laser

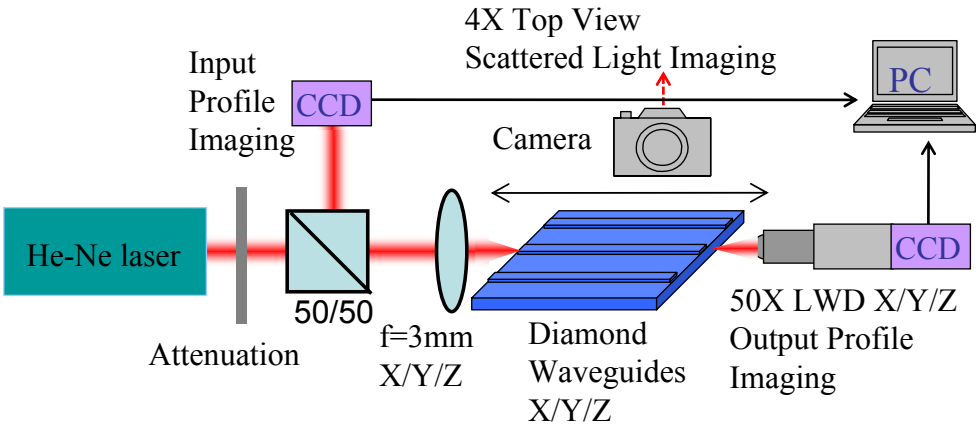

Figure 4.17: A schematic diagram of the diamond waveguide light coupling setup.

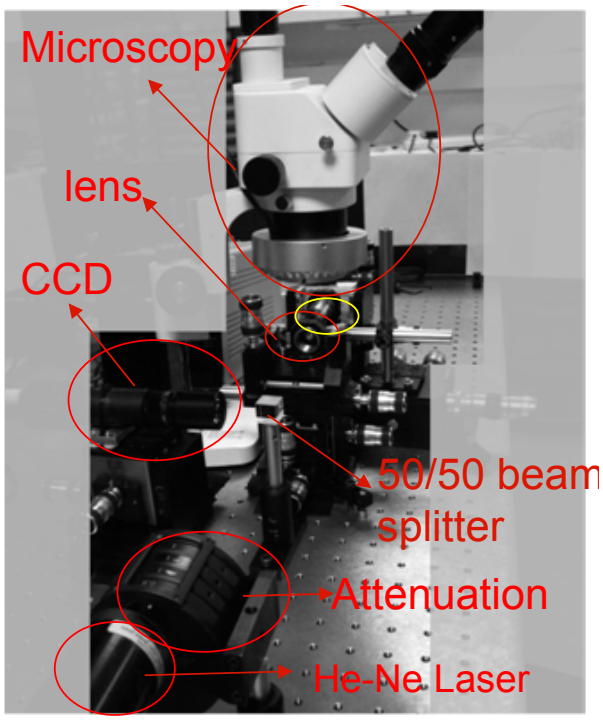

Figure 4.18: Photograph of the waveguide coupling setup. The sample holder with the diamond waveguide sample is highlighted in the yellow circle.

(633 nm) and a lens (focal length: 3 mm) were used to edge-couple light into the waveguide. The diamond waveguide was placed under a microscope so as to monitor the alignment as shown in Figure 4.18. Two CCD cameras were used and connected to a computer in order to observe the input/output end of the waveguide.

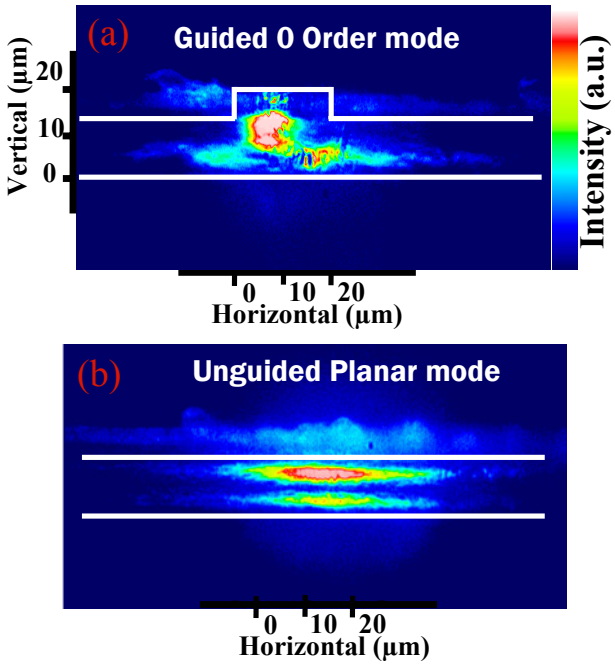

Figure 4.19: Light intensity of the output profile of (a) the guided fundamental mode in the diamond rib waveguides, and (b) the unguided planar mode from the diamond slab. The white line shows the ideal structural outline of the diamond waveguide.

4.4.2 Optical characterization result

The measured output light intensity profiles for the guided fundamental mode of the rib waveguides and an adjacent unguided planar mode from the diamond substrate are shown in Figures 4.19(a) and 4.19(b), respectively. These images show that the light intensity distributions between the waveguide and diamond substrate are clearly different. The light confinement by the rib waveguides is clearly observed, demonstrating the guiding functions of the diamond waveguide. The measured mode profile width and height agrees with theoretical modelling, however we note that the apparent distortion of the measured mode structure here is simply a function of the quality of the polished edge of the diamond samples used, and not of the waveguide processing technique. This also unfortunately prevents the un-equivocal evaluation of the waveguide loss. Improvements in the sample preparation should eliminate these effects.

4.5 Conclusion

In summary, we have successfully used inkjet printing, photolithographic patterning and ICP etching to fabricate large cross-section edge-coupled waveguides on

free-standing thin diamond substrates. By optimizing printing and photolithographic parameters, we achieved well-defined photoresist micro-stripes without any edge or coffee stain effects. Diamond rib waveguides extending to the very edge of the substrate were fabricated successfully. Optical characterisation with edge-coupling showed that these diamond waveguides do provide the expected guiding effects. This new fabrication technique has great potential to produce large length high-quality diamond waveguides and to develop novel diamond microstructures required by photonic quantum computing circuits.

Chapter 5

GaN waveguides and directional couplers

As presented in the previous chapters, integrated quantum photonics is a newly emerging area and the material of choice is still to be determined. In this chapter, we propose a move to a gallium nitride (GaN)-based material system for such applications, because GaN has a high refractive index which can result in a more compact footprint. GaN also benefits from a mature and versatile epitaxial technology which can provide readily available GaN wafers. Additionally, its transparency in the visible and near-infrared regions makes it attractive for use in combination with efficient Si-based single-photon detectors. Finally, it offers the prospects for on-chip integration with single photon sources, either fabricated in GaN itself (such as spontaneous parametric downconverters exploiting the nonlinear properties of GaN) or in the form of the diamond nitrogen-vacancy center, taking advantage of the close refractive index match between diamond and GaN.

In this chapter, we will introduce our work on GaN waveguides and directional couplers (DCs) along with the two-photon interference measurement made on our GaN DCs. In Section 5.1, we will explain briefly the Metalorganic Chemical Vapour Deposition (MOCVD) growth process of GaN materials. In Section 5.2, we will review the development of GaN waveguides in the literature before moving to our GaN rib waveguide design, fabrication and characterization as shown in Section 5.3. The design, fabrication, characterization and two-photon interference measurement of GaN DCs are introduced in Section 5.4. Section 5.5 is a brief summary of this Chapter.

5.1 GaN material growth

In this section, we will start with a brief history of MOCVD and then review the synthetic history of GaN. In the last subsection we introduce the particular MOCVD growth model we used for this work.

5.1.1 MOCVD

MOCVD is the acronym of *Metalorganic Chemical Vapour Deposition*, and some people prefer to name the same process as *Organometallic Vapour-Phase Epitaxy* (OMVPE), or other permutations of the same letters (MOVPE or OMCVD). Stringfellow wrote a book in the title of *Organometallic Vapour-Phase Epitaxy* and insists that '*organometallic should be used to describe the precursor molecules, since it agrees with the general chemical nomenclature*' [272]. However, MOCVD is a much common name in both industry and academic research today, so we will use MOCVD throughout this thesis.

The first patent on MOCVD growth of III-V compound semiconductors was filed by Scott in 1954 [273]. The first scientific paper on the epitaxial growth of GaAs using MOCVD was published by Manasevit in 1968 [274]. In 1975, Seki *et al.* reported a growth of extremely high-purity GaAs [275] which cleared early doubts on the capability of MOCVD. During 1970s and 1980s, many high performance devices were developed from MOCVD grown wafers, including room-temperature GaAlAs-GaAs lasers [276] and light-emitting diodes (LEDs) [277].

5.1.2 GaN growth

The synthesis of GaN was reported by Warren C. Johnson *et al.* 80 years ago [278]. They prepared GaN by reacting metallic gallium with ammonia gas at 900-1000^{o}C and interpreted the reaction expression as follows:

$$2\mathrm{Ga} + 2\mathrm{NH_3} = 2\mathrm{GaN} + 3\mathrm{H_2}$$

This was believed to be the earliest report of GaN synthesis [279]. The early history of single crystalline GaN growth and characteristics can be found in Strite's review paper [279].

In 1968, James Tietjen at Radio Corporation of America (RCA) encouraged Herbert Maruska to start research on single crystal growth of GaN film in the hope of realizing blue LEDs and ultimately developing a flat TV. Later on, they reported the single crystalline GaN grown by a vapour phase growth technique

i.e. HVPE (hydride vapor phase epitaxy) process [280, 281]. In their method, a Ga source was heated up to 900 ^{o}C, an HCl flow was used to carry the Ga vapour and NH_3 was used to provide the N source. During growth, the sapphire substrate was heated at about 825 ^{o}C and the GaN deposition rate was about 0.5 μm/min.

Also at RCA Laboratories, J. I. Pankove *et al.* reported first GaN metal-insulator-semiconductor (MIS) LEDs with green and blue emissions [282]. Owing to unsuccessful p doping attempts, the efficiencies of these LEDs were very low. The external power efficiency was about 10^{-4} and external quantum efficiency was $\sim 1\%$ for the green GaN MIS LED.

In 1989, Hiroshi Amano *et al.* achieved GaN p-type material by low energy electron beam irradiation (LEEBI) of Mg-doped GaN in Isamu Akasaki's group [283]. Based on this material, they fabricated the very first $p-n$ junction GaN blue LED at room temperature. In 1992, Shuji Nakamura reported a more commercially available method to achieve p-type GaN materials by thermal annealing of Mg-doped GaN at Nichia Corporation [284]. In 1993, Shuji Nakamura demonstrated a bright blue GaN LED (1 Candela) [285]. This InGaN/AlGaN double-heterostructure LED featured a Zn-doped InGaN layer with a typical output power of 1.5 mW. The external quantum efficiency was as high as 2.7% at a forward current of 20 mA at room temperature. In 1995, Shuji Nakamura demonstrated the first pulsed violet InGaN multiple quantum well (MQW) LDs [286] and later in the same year he realized the first CW violet InGaN MQW LDs [287].

Today, GaN is one of the most important optoelectronic materials and has been widely used for applications like LEDs, laser diodes, and high electron mobility transistors (HEMTs), etc. These exciting applications have motivated much further research on GaN crystal growth and processing development.

5.1.3 The Aixtron 200/4 RF-S MOCVD reactor

The GaN samples used in this work were home-grown by a horizontal-flow, low-pressure Aixtron 200/4 RF-S single wafer MOCVD reactor as shown in Figure 5.1. Figure 5.2 provides a schematic view of the internal arrangement of the deposition cell, gas inlet and exhaust gas treatment subsystem of the reactor. In this MOCVD system, hydride and metal-organic precursors are injected through two inlet channels separated by a quartz plate, which extends through the cooler zone of the cell. The main precursors used in our GaN growth are supplied from stainless steel containers termed bubblers, which are housed in thermostat baths

Figure 5.1: Image of the AIX 200/4 RF-S MOCVD system. Image courtesy: Ian W. Watson.

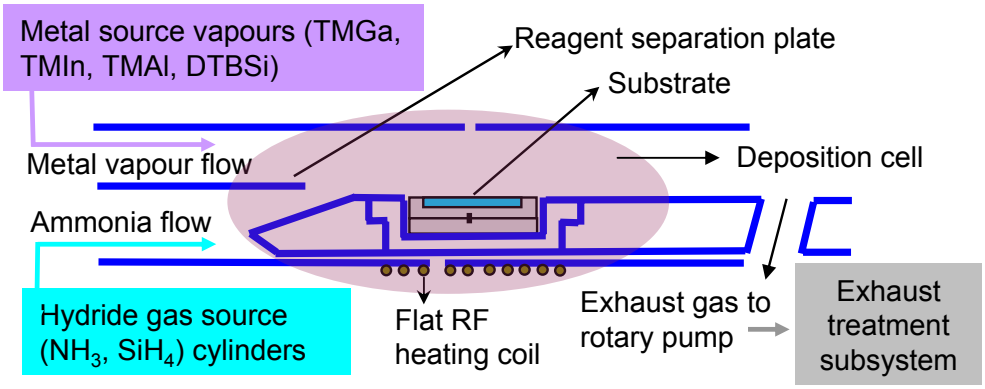

Figure 5.2: Schematic modular representation of the AIX 200/4 RF-S MOCVD reactor.

inside the main cabinets of the MOCVD system. The sources of the group III metals are metal alkyls, specifically trimethyl compounds henceforth given the abbreviations TMGa, TMIn and TMAl. TMGa was first produced about 80 years ago [288] and is now commercially available.

The basic reaction process of GaN MOCVD growth is:

$$Ga(CH_3)_{3(v)} + NH_{3(v)} = GaN_{(s)} + 3CH_{4(v)}$$

where 'v' refers to as vapour and 's' refers to as solid. Detailed growth and structure characteristics of GaN film using this reactor can be found in C. Deatcher's PhD thesis [289].

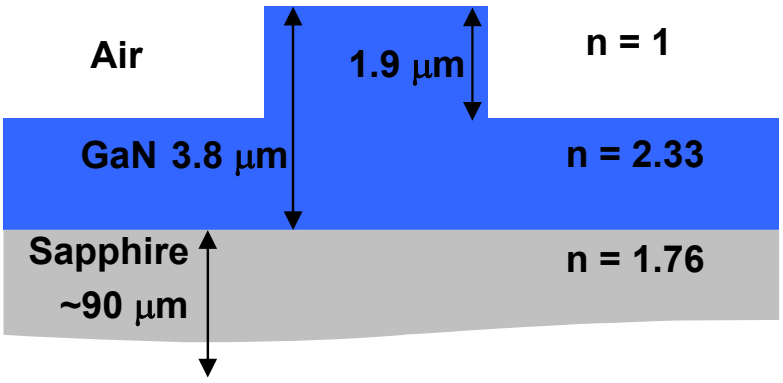

Figure 5.3: Schematic of the rib waveguide design using GaN on sapphire with air cladding. The ordinary index of GaN is used due to the restriction to TE operation [302].

5.2 Review of GaN waveguide structures

The historical developments of GaN waveguides are summarized in Table 5.1. Though our interest of GaN waveguides is mainly for applications in integrated quantum photonics which are somewhat different from the research listed in the table, it is still useful for us to understand the current research trends of GaN waveguides and the relevant material improvements. It is noticed that the focus of GaN waveguide research has currently shifted from the material properties investigation [290] to communications applications [291].

5.3 GaN rib waveguides

5.3.1 Design details

In this section, we will show our results on the design, fabrication and characterization of GaN rib waveguides. First, the waveguide structures were designed on a 3.8 μm thick GaN layer grown on *c*-plane sapphire by MOCVD. Figure 5.3 shows the cross-sectional schematic structure of a GaN rib waveguide with a etch depth of 1.9 μm. It is worth mentioning here that the sapphire substrate has a lower refractive index (1.76) than GaN (2.33) and thus it serves as a natural cladding layer. This is one of the advantages of using GaN over diamond for waveguide applications.

The designed structure of the GaN-on-sapphire used in this study complied with the fabrication procedure involving standard optical contact lithography and

Table 5.1: Summary of GaN waveguides in literature.

Year / Group / Institution	Growth / Measurement / Loss / structure / wavelength / references
2001-2011, E. Dogheche, Universit de Valenciennes	MOCVD heterostructures, prism coupling, 1.2 dB/cm for AlGaN/GaN, 1.8 dB/cm for AlGaN/AlN at 632.8 nm [292]; Waveguiding GaN on AlN/GaN SPS on silicon at 632.8 nm, no loss measurement [293]; GaN on AlN/GaN SPS on sapphire, 0.65 dB/cm at 1.55 μm, GaN on classical AlN nucleation layer, 4 dB/cm at 1.55 μm [294]
2002, A. J. Steckl, University of Cincinnati	MOCVD growth GaN, MBE growth GaN:Er channel waveguide, out-scattering technique, 5.4 dB/cm at 633 nm, 5.4 dB/cm at 1307 nm, 4.1 dB/cm at 1500 nm [290]
2003-2011, Rongqing Hui, University of Kansas	MOCVD GaN/$Al_xGa_{(1-x)}N$ heterostructures rib waveguide on sapphire, Fabry-Perot interference measurement give a loss of 34.4 dB/cm, 2×2 GaN/AlGaN heterostructure optical waveguide coupler, AWG-based WDM coupler [295, 296]
2004, J. Salzman, Technion, Israel Institute of Technology	Selective area MOCVD growth GaN multimode ridge waveguide, outscattering technique gives an internal optical loss ∼19 dB/cm, 1550 nm [297]
2005, R. Geiss, Bell Laboratories	HVPE growth free standing GaN, average of 2.41dB/cm and 1.85dB/cm for Transverse Electric (TE) and Transverse Magnetic (TM) polarizations, minimum loss values 0.82 dB/cm (TE) and 0.61 dB/cm (TM) at 1550 nm[298]
2005, N. Suzuki, Toshiba Corporation	MOCVD grown GaN, polarization dependent loss (PDL) 10-20 dB/cm, MBE growth GaN PDL 100 dB/cm [299]
2008, F. H. Julien, Universite Paris-Sud	GaNInAlN ridge waveguides by MOCVD, photolithography and ICP, FabryPerot measurements gave a propagation loss of 18 (TE) and 49 dB/cm (TM), slab waveguide 30 dB/cm [300]
2009, H. Jiang, Texas Tech University	Er-doped AlGaN/GaN:Er/AlGaN heterostructures strip waveguides by MOCVD, photolithography and ICP, propagation loss 15 dB/cm at 1540 nm [291]
2011, Y. Nakano, University of Tokyo	MOCVD AlN rib waveguide on GaN/AlN multiple quantum wells, supercontinuum light measurement give a loss of 40 dB/cm [301]

a single etching step [291]. The waveguide designs were based on the large cross-section rib waveguide single-mode criteria [127, 264, 303] with near-circular beam profiles (numerically evaluated to be 95.8% with a circularly symmetric Gaussian beam) as presented in Chapter 4.

The beam propagation method (BPM) and finite element analysis (FEA)

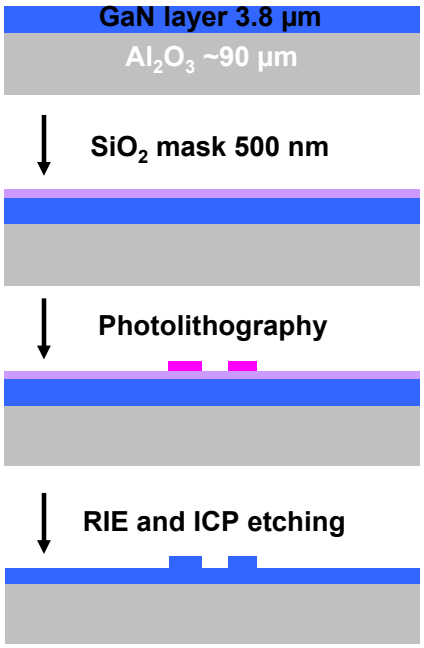

Figure 5.4: Process flow of the GaN rib waveguide fabrication.

simulations were used to design all the waveguide devices. The design method is similar as that used in the Chapter 4 for diamond waveguide design. Rib waveguides were designed based on 3.8 μm-thick GaN film on sapphire. Etching depth of 1.9 μm and a rib width of 4 μm will give single mode operation for wavelength range of 600 nm-1300 nm.

5.3.2 Waveguide fabrication

Standard photolithography methods and dry etching including reactive ion etching (RIE) and inductively coupled plasma (ICP) etching were used to fabricate the GaN waveguides. The process flow of making GaN waveguides is shown in Figure 5.4. First, 500 nm-thick SiO_2 was deposited on the GaN/sapphire substrate. Then photoresist was spin-coated and standard photolithography applied. SiO_2 was etched by RIE using the Ar/CH_3 recipe shown in Table 4.6 of Chapter 4. After resist stripping, the SiO_2 mask was transferred to GaN by ICP etching using the recipe shown in Table 5.2. The GaN waveguide etching depths were determined by simulation and could be controlled by simply changing the etching time. For a 1.9 μm GaN depth, the ICP etching took 126 seconds. Residual SiO_2 mask was removed by buffered oxide etch (BOE).

After the waveguide structures were transferred to the GaN layer, the sample was then manually cleaved to achieve two parallel optical quality facets for optical coupling. As 'normal' GaN does not have a cubic crystal structure, it is very

Table 5.2: ICP recipe for GaN etching and etching rate of GaN and SiO_2.

Pressure	Cl_2 flow	Coil power	Platen power	GaN etching rate	SiO_2 etching rate
7 mTorr	50 sccm	700 W	300 W	905 nm/min	175 nm/min

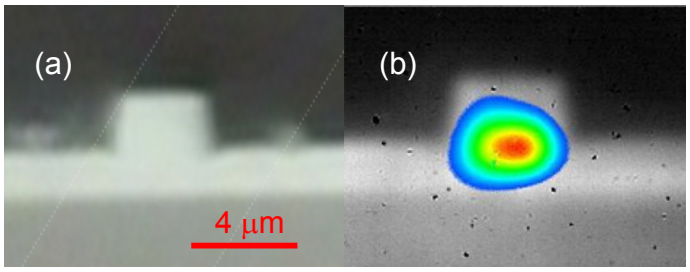

Figure 5.5: Optical images of the output facet (a) without and (b) with an overlay of the measured intensity profile (using false colour) of the guided mode.

hard to cleave the sample to get an intended edge. R. K. Sink made extensive investigations on GaN cleavage [304]. The first method he used is wafer fusion, He first bonded a GaN laser structure to an InP substrate and then cleaved the sample along the cleave planes of InP to obtain optically flat GaN facets [305]. To facilitate the cleaving, he thinned down the sample to less than 50 μm thick. By that way, he fabricated the laser structure successfully [304]. We adopted this thin substrate method for our GaN waveguide work. By thinning down our GaN/sapphire substrates to about 90 μm, we were able to cleave the sample after the waveguide fabrication to obtain optical quality GaN facets. The sample at that thickness is also strong enough for handling during the fabrication and optical measurement.

5.3.3 Characterization

The GaN rib waveguides were characterized by using a similar setup to that shown in Figure 4.17. The optical image of a GaN waveguide facet structure is shown in Fig. 5.5(a) and the waveguide facet in combination of an overlay of the measured light intensity profile using false colour is shown in Fig. 5.5(b). This measured mode profile remained stable throughout a range of coupling positions confirming the single-mode nature of the fabricated GaN waveguide.

Using a narrow-linewidth wavelength-tunable laser source (HP 8167B) and the well established Fabry-Pérot (F-P) loss measurement technique [306], the upper limit of propagation loss at a wavelength of 1300 nm was evaluated for the fabricated GaN rib waveguides. The measured F-P fringe and fitted data are

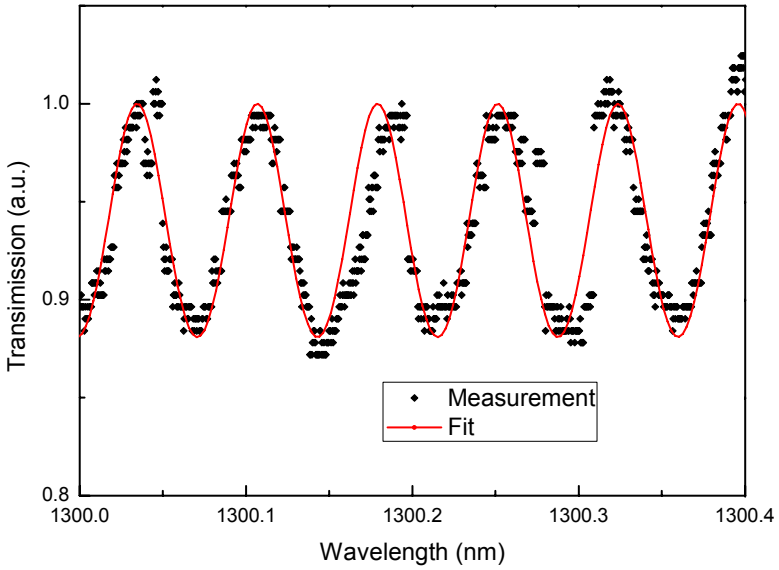

Figure 5.6: Measured F-P fringe and fitted data of GaN rib waveguide.

plotted in Figure 5.6. The fitting was based on the Airy transmission function [307]:

$$T(\lambda) = \frac{(1-R)^2 e^{-\alpha L}}{(1-r)^2 + 4r(sin\phi)^2} \tag{5.1}$$

where combined loss-reflection coefficient $r = Re^{-\alpha L}$ and phase accumulated over a round trip $\phi = \frac{2\pi nL}{\lambda}$. Fitting parameters are as follows: end-facet reflectivity R=0.17, length of GaN rib waveguide L=7 mm, refractive index n=2.32@1330 nm and waveguide propagation loss α=0.240 /mm=10.4 dB/cm. This loss can be reduced through improvements of film quality such as using an AlN/GaN short period-superlattice (SPS) buffer layer system during growth [294] as well as optimization of etching to achieve better sidewall smoothness.

After confirming the suitability of fabricating rib waveguides from these home-grown GaN materials, we proceeded to the design and fabrication of GaN directional couplers (DCs) which can be used to replace bulk beam splitters for two-photon interference measurements.

5.4 GaN directional couplers

DCs (plan view and 3D diagram shown in Figure 5.7(a-b)) are one of the key components for integrated optics, and are a fundamental building block in emerging topics such as integrated quantum photonic circuits [308]. As summarized in Chapter 1, quantum photonic circuits have been demonstrated in low-index-

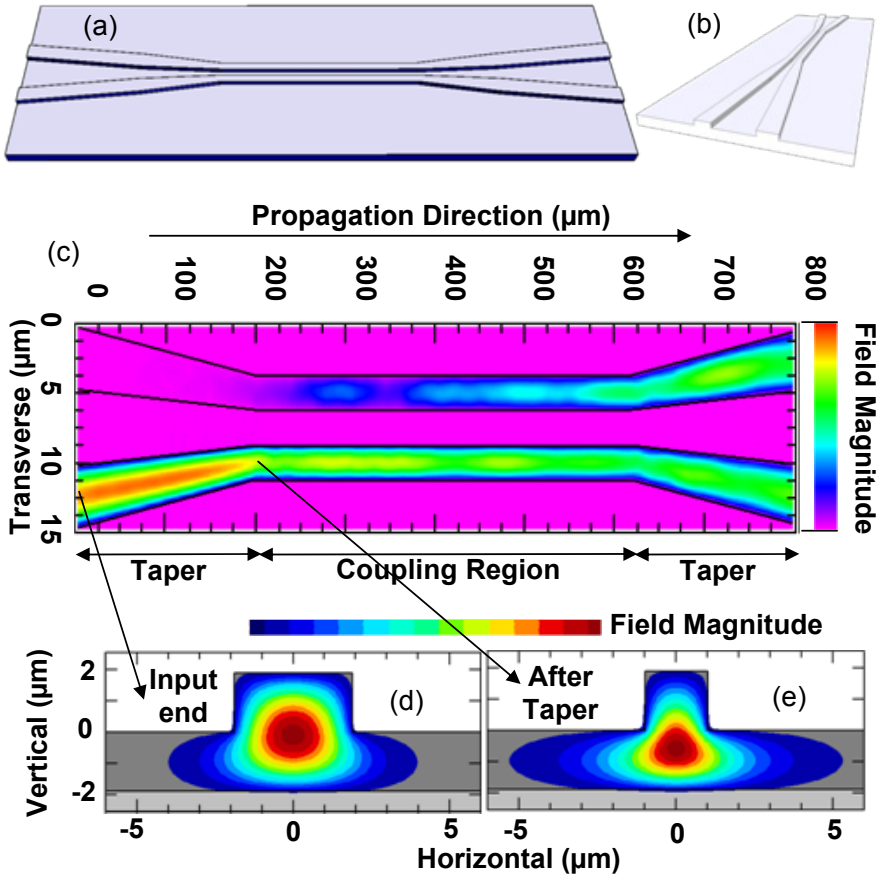

Figure 5.7: Plan view (a) and 3D diagram (b) of a GaN DC; (c) Plan view BPM simulation of GaN DC design with a 2-μm gap; (d) TE field profile of guided mode at the device input end, and (e) TE field profile of guided mode in the coupling region.

contrast waveguide materials including silica-on-silicon and glass [104, 108, 112]. In the following sections, we will show the design and fabrication of GaN DCs and a particular application for two-photon interference.

5.4.1 Design and optimization

Considering a free-space wavelength of 800 nm and TE (ordinary ray) operation, the GaN DCs were designed and simulated. The key design features of our GaN DCs are the optimized waveguide cross-sections and inverse tapers [309] in order to enhance coupling efficiency and minimize device footprint..

Figure 5.7(c) presents a plan view of BPM simulation of GaN DC design with a 2-μm gap. For this design, the rib width varies from 4 μm (Figs. 5.7(d)) in the input end to 2 μm (Fig. 5.7(e)) in the coupler region. The calculated TE field profiles with different rib widths are shown in Figure 5.7. It can be seen that

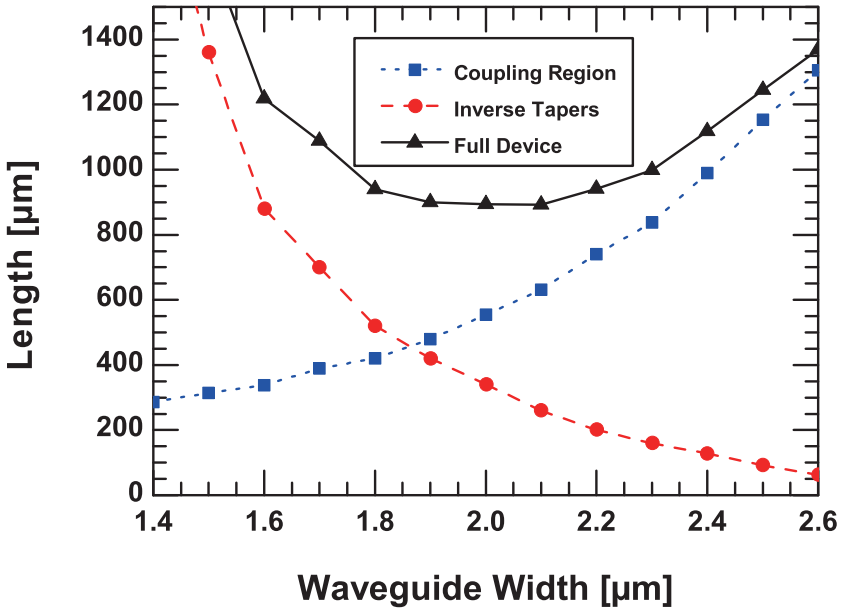

Figure 5.8: Device length optimization when changing rib width in the coupling region. It shows the minimum device length required to connect a 3.8-μm wide rib waveguide to the coupling region with a rib width between 1.4 and 2.6 μm for a 0.05 dB taper loss.

the mode spreads further horizontally into the underlying slab with reducing rib width which, in turn, leads to an increased mode overlap and shorter coupling length.

However, when using inverse tapers to connect the input/output straight sections to the coupling region, the larger the rib width difference, the longer the taper needs to be in order to limit the amount of induced radiation loss. By optimizing the width of the waveguide at the coupling section which is a trade-off between a short coupler and short inverse tapers [310], a minimized overall device footprint can be achieved. The full device length is calculated by BPM and is the summation of the constituent inverse taper and coupling region length. Fig. 5.8 shows the length change of the coupling section, inverse taper and full device versus waveguide width in the coupling section. This calculation show that a minimized device length of 900 μm can be achieved at a waveguide width of 2 μm in the coupling section, which is more than four times shorter in device length compared with a similar DC at a 2-μm separation without inverse tapers.

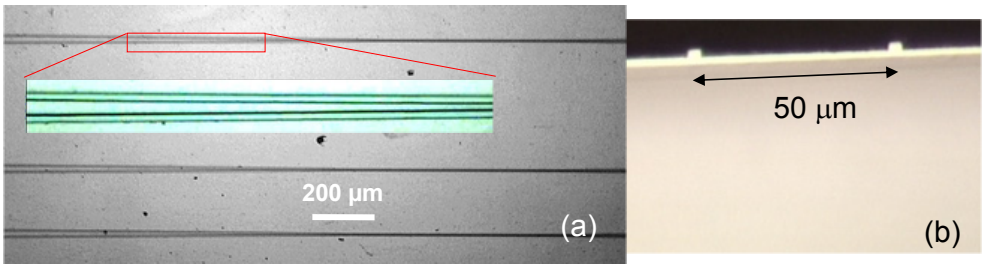

Figure 5.9: (a) Optical plan view micrograph of GaN DCs with (inset) high magnification image of coupling region; (b) optical image of cleaved GaN DC facet.

5.4.2 Fabrication and structural inspection

To fabricate the GaN DCs, the GaN/sapphire substrate was thinned down to 90 μm to assist cleaving and also to provide smooth facets perpendicular to the guide for the end coupling. The DC structures were defined by first patterning S1805 photoresist. The DC pattern was then transferred to a 500-nm SiO_2 hard mask by reactive ion etching and subsequently into GaN by inductively-coupled plasma etching using Cl_2/Ar gases, following the process flow of Fig. 5.4. To ease arm discrimination with free space optics, the device was positioned in the center of a 5-mm-long chip with ~2 mm sections at either end of the device providing additional separation between the arms with an angular separating rate of 1.1^o. Stylus profilometer measurement confirmed that the etching depth of the GaN coupler is 1.9 μm. After the sample was cleaved, an optical microscope was used to inspect the input and output facets of the GaN DCs. The optical images of the DCs are shown in Fig. 5.9(a). The inset of the figure is a high magnification image at the coupling region. Figure 5.9(b) shows an optical image of the cleaved GaN DC facets.

SEM inspection was conducted and confirmed the high quality facets of the DCs (Figure 5.10) and a well defined coupling region gap (Figure 5.11). The sloped sidewalls of the waveguide rib were measured to be 7^o off verticality. The BPM simulations were performed to confirm that this feature does not substantially change the device coupling characteristics compared to ideal vertical sidewalls [311]. It is in fact possible to further optimize and fine tune the coupling length by accurately controlling the sidewall angle with particular GaN etching recipes [312].

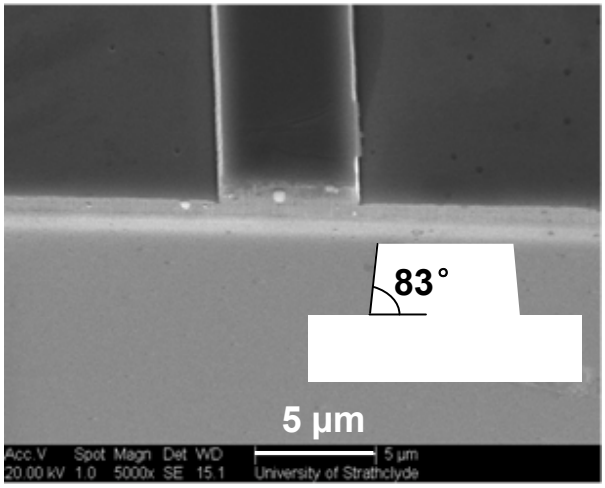

Figure 5.10: Oblique SEM image of cleaved facet with (inset) inferred facet etch profile.

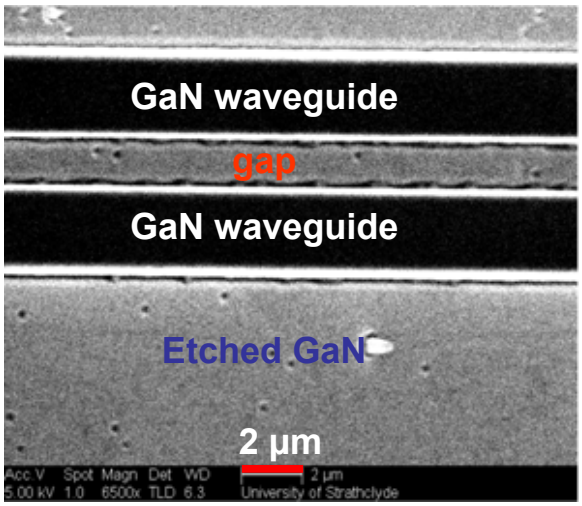

Figure 5.11: SEM plan view image of coupling region. Black regions indicate the waveguides. The coupler gap and waveguide sidewalls are clearly visible.

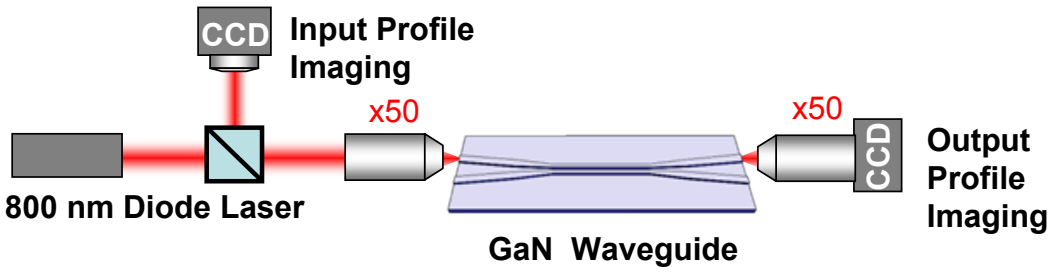

Figure 5.12: Optical setup for GaN DC measurement.

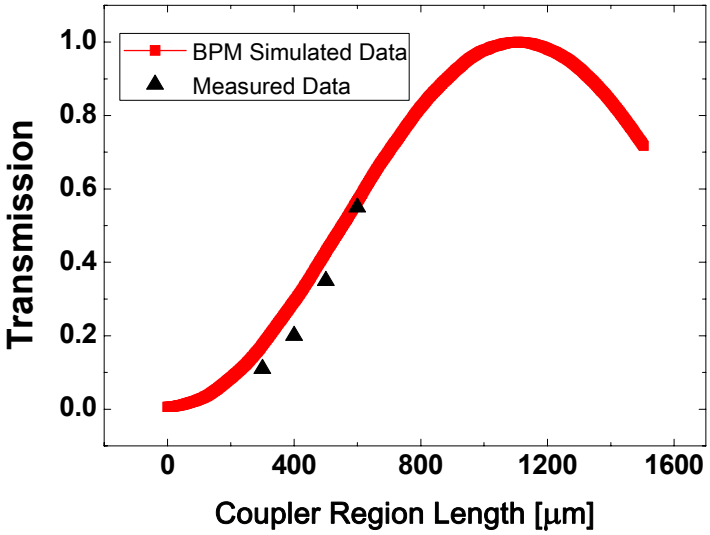

Figure 5.13: Measured transmission for fabricated GaN DCs with varying coupling length. The curve is a BPM simulation of the transmission using the parameters shown in Fig. 5.7(c) at a wavelength of 800 nm.

5.4.3 Optical characterization

The guided mode profiles of the GaN straight waveguides and DCs were characterized by using a diode-laser emitting at a wavelength of 800 nm. Laser light was coupled into the waveguides using free-space optics and the output from the waveguide was imaged onto a charged coupled device (CCD) with a 50X microscope objective as shown in Figure 5.12.

The transmission of the DCs was measured by injecting a fixed power (2 mW) into each arm of the DC and measuring the power at both waveguide output ports. This method mitigates the potential loss differences between the different arms of the DC. The range of measured transmission was found to vary between 0.1:0.9 to 0.55:0.45 (Fig. 5.13). As shown in Figure 5.13, the measured transmission dependence on coupling length agrees well with the simulation predictions.

5.4.4 Two-photon interference in GaN DCs

Remark: The work in this Subsection is completed in collaboration with Prof. Jeremy L. OBrien's group at the University of Bristol.

Finally, to confirm the suitability of such GaN DC structures for integrated quantum photonic circuits, a two-photon quantum interference experiment was carried out with a DC with a 55:45 splitting ratio in the University of Bristol. Using a setup as shown in Figure 5.14, degenerate photon pairs at a wavelength of 804 nm were produced by spontaneous parametric down conversion (SPDC)

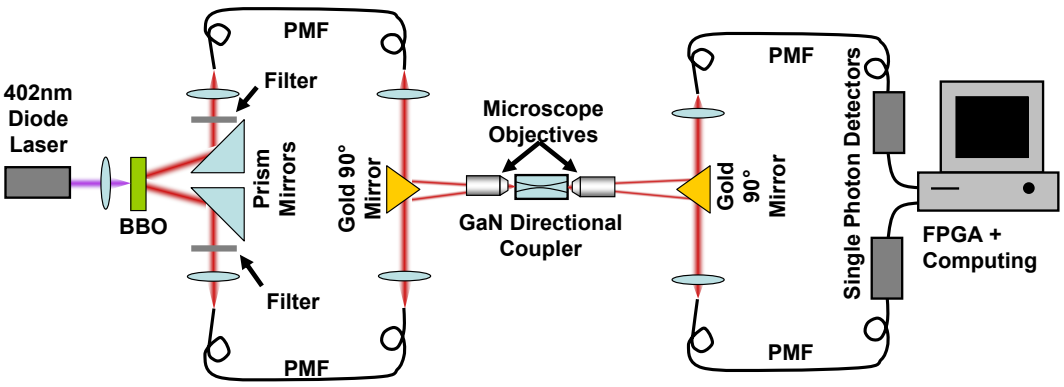

Figure 5.14: The setup of Hong-Ou-Mandel quantum interference

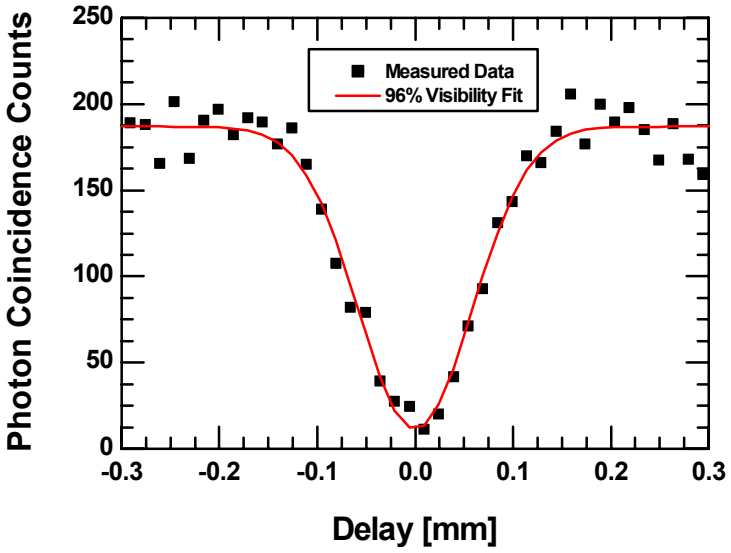

Figure 5.15: The Hong-Ou-Mandel dip observed for a 45:55 GaN rib waveguide DC, the signature of quantum interference between two degenerate photons. The fitted visibility is 96%.

using a GaN-laser-diode and a β-barium borate type-I crystal. The principle of SPDC has been described in Chapter 1. These photon pairs were fibre-coupled to separate polarization maintaining fibers (PMF) after going through narrow band filters and relayed using free-space optics to the input waveguides of the GaN DC. Output photons were collected in a similar manner and coupled to avalanche photo diodes. Photon counting and coincidence logic were then performed with field programmable gate array circuitry with computer control.

Fig. 5.15 shows the measured Hong-Ou-Mandel dip, the signature of quantum interference between two degenerate photons [15]. The fitted visibility of 96% demonstrates high quality interference and confirms single-mode propagation. Theoretical visibility is determined by the transmission (T) of GaN DCs using

formula 5.2 [313].

$$V = 1 - \frac{(2T-1)^2}{T^2 + (T-1)^2} \tag{5.2}$$

For T=0.55, theoretical visibility V=98%. This means the experimental visibility is very close to the theoretical one.

5.5 Conclusion

In summary, GaN-on-sapphire rib waveguides and DCs have been designed, fabricated and characterized with applications as quantum information circuits in mind. DCs design exploiting optimized waveguide cross-sections and inverse tapers for low-loss and minimal footprint structures has been proposed and experimentally validated. Single-mode devices with coupling splitting ratios varying between 10:90 and 55:45 have been studied and two-photon interference was demonstrated in these structures. This work opens up new ways for developing more sophisticated quantum photonic circuits based on GaN.

Chapter 6

Summary and perspectives

6.1 Summary

This thesis presents a study on the design, fabrication and characterization of diamond and GaN photonic structures for applications in integrated quantum photonics. In this chapter, we will summarize the work briefly and propose some future work on integrated quantum photonics, particularly relevant to diamond and other compound semiconductor materials.

In this thesis work, we have first demonstrated the fabrication of diamond microlenses with a high aspect ratio by using two novel methods presented in Chapter 3. One is a dual-mask method that utilizes the different selectivities between resist and SiO_2 in Ar/Cl_2 plasma and SiO_2/diamond in Ar/O_2 plasma. To improve the smoothness of diamond microlenses, SiO_2 colloidal microspheres were also used as a mask to realize diamond microlenses in Ar/Cl_2 plasma. The diamond microlenses fabricated by this one step etching method could be used to increase the light extraction efficiency of diamond colour centres for various applications.

In Chapter 4, we first give a full survey on how to make a refractive index contrast in single crystalline bulk diamond. To develop the edge coupled diamond waveguides, we chose commercially available thin diamond chips. Given the thickness of the chip, we have found that large cross-section rib waveguides can sustain single mode operation. The big obstacle for making edge coupled waveguides on the small diamond chip has been overcame by the combination of using photoresist inkjet printing, photolithographic patterning and ICP etching. By optimising printing and photolithographic parameters, we achieved well-defined photoresist micro-stripes without any edge and coffee stain effects. Diamond rib waveguides extending to the very edge of the substrate were successfully fabri-

cated. Optical characterisation with edge-coupling indicated that these diamond waveguides do provide the expected guiding effects. To the best of our knowledge, this is the first ever report on edge coupled diamond rib waveguide. The new fabrication technique has great potential for developing large length high-quality diamond waveguides and other novel diamond microstructures required by integrated quantum photonics.

As described in Chapter 5, GaN-on-sapphire rib waveguides and directional couplers have been designed, fabricated and characterised with applications as quantum information circuits in mind. Single-mode directional couplers with reflectivity varying between 0.1 and 0.55 have been studied and two-photon interference was demonstrated in these microstructures. This is the first demonstration of two-photon interference realized on a compound semiconductor chip. Our work opens up a new way to achieve sophisticated integrated quantum photonic circuits based on GaN and other suitable compound semiconductors and demonstrates the potential to integrate source, circuit and detector in one chip.

6.2 Future works

Integrated quantum photonics has been a hot research topic since 2008 when this PhD began. Amazing progress has been made in this area over the last four years. In the following section, a few possible directions of integrated quantum photonics relevant to our work will be highlighted.

6.2.1 All-diamond platform

For diamond integrated photonic circuits, the realization of a Hanbury Brown and Twiss (HBT) circuit would be logically the next step. It is worth pointing out that it is not possible to achieve more complex photonic structures like directional couplers on the diamond plates used for the diamond waveguide fabrication as shown in Chapter 4. Even thinner and larger diamond plates are needed for such work but they were not quite ready when this work was conducted. However, recently, we found out that Element 6 (Holland) can now provide off-the-shelf 5 μm thick 3×3 mm diamond plates. These diamond plates have been used to develop diamond micro-rings. The resonant enhancement of the zero-phonon emission in such a diamond ring cavity has thus been recently demonstrated [254]. The lift-off homoepitaxial diamond membranes made by ion implanted, post CVD growth and separation can be another strong candidate for developing

more complex photonic structures since the membrane thickness can be controlled by CVD growth.

It is also possible to integrate a diamond directional coupler with the diamond colour (NV) centre. For such device, the emission from the colour centre can be coupled to the waveguide directional coupler.

The second step along this line would be the realization of two-photon interference on diamond chip. Using the method developed by David D. Awschalom [314], Ronald Hanson [59] and Mikhail D. Lukin [60], it should be feasible to realize the an HBT circuit first. Edge coupled diamond rib waveguides developed in this work (Chapter 4) would be very useful for achieving such devices.

6.2.2 A III-V semiconductor platform

III-V semiconductors provide another strong material candidate for integrated quantum photonics. Similar to the suggestion for diamond integrated quantum photonic circuits, the ability to incorporate semiconductor a quantum dot single photon source with a photonic circuit is logically the next step. The mature epitaxial growth and readily developed photonics fabrication capability of III-V semiconductors will be a huge advantage. It is thus possible to integrate single photon sources and detectors with quantum circuits on a single chip.

6.2.3 A hybrid integrated quantum circuit

Another idea would be the hybrid integration of various components made from different materials, e.g. coupling diamond NV centres to silica microspheres [315–319], metal nanoparticles [320, 321], toroidal microresonators [322], GaP waveguides [323], GaP microcavities [324], GaP nanocavities [325], photonic crystals [326–329], etc. It is also noticed that this hybrid method can utilize existing semiconductor fabrication technology that is not directly applicable for diamond processing.

A hybrid photonic circuits of diamond/GaN would be the next step for our group. In fact, we have started to build a GaN undercut microdisk for future integration with a diamond NV center.

6.3 Final remark

Integrated quantum photonics is a widespread research topic, currently undergoing explosive developments. Throughout this PhD study and thesis writing, I

have been constantly amazed by the progress of integrated quantum photonics around the world. I am glad that I witnessed the rapid development in this area and am proud of being part of it.

Bibliography

[1] E. Knill, R. Laflamme, G. Milburn *et al.*, "A scheme for efficient quantum computation with linear optics," Nature **409**, 46–52 (2001).

[2] J. Michel, Y. Shen, A. Aiden, A. Veres, M. Gray, J. Pickett, D. Hoiberg, D. Clancy, P. Norvig, J. Orwant *et al.*, "Quantitative analysis of culture using millions of digitized books," Science **331**, 176 (2011).

[3] M. Planck, "On the law of distribution of energy in the normal spectrum," Annalen der Physik **4**, 1 (1901).

[4] M. Planck, *The theory of heat radiation*, 11 (Amer Inst of Physics, 1906).

[5] A. Einstein, "Über einen die erzeugung und verwandlung des lichtes betreffenden heuristischen gesichtspunkt," Annalen der Physik **322**, 132–148 (1905).

[6] A. Fox, *Quantum optics: an introduction*, vol. 15 (Oxford University Press, USA, 2006).

[7] R. Millikan, "A direct photoelectric determination of plancks h," Physical Review **7**, 355–388 (1916).

[8] A. Zeilinger, G. Weihs, T. Jennewein, and M. Aspelmeyer, "Happy centenary, photon," Nature **433**, 230–238 (2005).

[9] A. Compton, "The spectrum of scattered x-rays," Physical Review **22**, 409 (1923).

[10] R. Brown and R. Twiss, "Correlation between photons in two coherent beams of light," Nature **177**, 27–29 (1956).

[11] T. Maiman, "Stimulated optical radiation in ruby," Nature **187**, 493–494 (1960).

[12] R. Glauber, "Photon correlations," Physical Review Letters **10**, 84–86 (1963).

[13] R. Glauber, "Coherent and incoherent states of the radiation field," Physical Review **131**, 2766 (1963).

[14] H. Kimble, M. Dagenais, and L. Mandel, "Photon antibunching in resonance fluorescence," Physical Review Letters **39**, 691–695 (1977).

[15] C. K. Hong, Z. Y. Ou, and L. Mandel, "Measurement of subpicosecond time intervals between two photons by interference," Phys. Rev. Lett. **59**, 2044–2046 (1987).

[16] R. Feynman, "Simulating physics with computers," International journal of theoretical physics **21**, 467–488 (1982).

[17] D. Deutsch, "Quantum theory, the church-turing principle and the universal quantum computer," Proceedings of the Royal Society of London. A. Mathematical and Physical Sciences **400**, 97 (1985).

[18] P. Shor, "Algorithms for quantum computation: discrete logarithms and factoring," in "Foundations of Computer Science, 1994 Proceedings., 35th Annual Symposium on," (IEEE, 1994), pp. 124–134.

[19] L. Grover, "A fast quantum mechanical algorithm for database search," in "Proceedings of the twenty-eighth annual ACM symposium on Theory of computing," (ACM, 1996), pp. 212–219.

[20] L. Grover, "Quantum mechanics helps in searching for a needle in a haystack," Physical Review Letters **79**, 325–328 (1997).

[21] R. Cleve, A. Ekert, C. Macchiavello, and M. Mosca, "Quantum algorithms revisited," Proceedings of the Royal Society of London. Series A: Mathematical, Physical and Engineering Sciences **454**, 339 (1998).

[22] A. Childs and W. Van Dam, "Quantum algorithms for algebraic problems," Reviews of Modern Physics **82**, 1 (2010).

[23] I. Chuang, L. Vandersypen, X. Zhou, D. Leung, and S. Lloyd, "Experimental realization of a quantum algorithm," Arxiv preprint quant-ph/9801037 (1998).

[24] J. Jones, M. Mosca, and R. Hansen, "Implementation of a quantum search algorithm on a quantum computer," Nature **393**, 344–346 (1998).

[25] T. Ladd, F. Jelezko, R. Laflamme, Y. Nakamura, C. Monroe, and J. OBrien, "Quantum computers," Nature **464**, 45–53 (2010).

[26] J. O'Brien, "Optical quantum computing," Science **318**, 1567 (2007).

[27] P. Kok, W. Munro, K. Nemoto, T. Ralph, J. Dowling, and G. Milburn, "Linear optical quantum computing with photonic qubits," Reviews of Modern Physics **79**, 135 (2007).

[28] R. Okamoto, J. OBrien, H. Hofmann, and S. Takeuchi, "Realization of a knill-laflamme-milburn controlled-not photonic quantum circuit combining effective optical nonlinearities," Proceedings of the National Academy of Sciences **108**, 10067 (2011).

[29] N. Gisin, G. Ribordy, W. Tittel, and H. Zbinden, "Quantum cryptography," Reviews of Modern Physics **74**, 145–195 (2002).

[30] R. Glauber, "The quantum theory of optical coherence," Physical Review **130**, 2529 (1963).

[31] M. Eisaman, J. Fan, A. Migdall, and S. Polyakov, "Invited review article: Single-photon sources and detectors," Review of Scientific Instruments **82**, 071101 (2011).

[32] F. Diedrich and H. Walther, "Nonclassical radiation of a single stored ion," Physical Review Letters **58**, 203–206 (1987).

[33] T. Basché, W. Moerner, M. Orrit, and H. Talon, "Photon antibunching in the fluorescence of a single dye molecule trapped in a solid," Physical Review Letters **69**, 1516–1519 (1992).

[34] A. Imamoglu and Y. Yamamoto, "Turnstile device for heralded single photons: Coulomb blockade of electron and hole tunneling in quantum confined pin heterojunctions," Physical Review Letters **72**, 210–213 (1994).

[35] A. Shields, "Semiconductor quantum light sources," Nature Photonics **1**, 215–223 (2007).

[36] C. Murray, D. Norris, and M. Bawendi, "Synthesis and characterization of nearly monodisperse CdE (E= sulfur, selenium, tellurium) semiconductor

nanocrystallites," Journal of the American Chemical Society **115**, 8706–8715 (1993).

[37] M. Hines and P. Guyot-Sionnest, "Synthesis and characterization of strongly luminescing zns-capped cdse nanocrystals," The Journal of Physical Chemistry **100**, 468–471 (1996).

[38] A. P Michler *et al.*, "Quantum correlation among photons from a single quantum dot at room temperature," Nature **406**, 968–970 (2000).

[39] M. De Vittorio, F. Pisanello, L. Martiradonna, A. Qualtieri, T. Stomeo, A. Bramati, and R. Cingolani, "Recent advances on single photon sources based on single colloidal nanocrystals," Opto-Electronics Review **18**, 1–9 (2010).

[40] P. Michler, A. Kiraz, C. Becher, W. Schoenfeld, P. Petroff, L. Zhang, E. Hu, and A. Imamoglu, "A quantum dot single-photon turnstile device," Science **290**, 2282 (2000).

[41] C. Becher, A. Kiraz, P. Michler, A. Imamoğlu, W. Schoenfeld, P. Petroff, L. Zhang, and E. Hu, "Nonclassical radiation from a single self-assembled inas quantum dot," Physical Review B **63**, 121312 (2001).

[42] C. Santori, M. Pelton, G. Solomon, Y. Dale, and Y. Yamamoto, "Triggered single photons from a quantum dot," Physical Review Letters **86**, 1502–1505 (2001).

[43] V. B. Verma, M. J. Stevens, K. L. Silverman, N. L. Dias, A. Garg, J. J. Coleman, and R. P. Mirin, "Photon antibunching from a single lithographically defined InGaAs/GaAs quantum dot," Opt. Express **19**, 4182–4187 (2011).

[44] Z. Yuan, B. Kardynal, R. Stevenson, A. Shields, C. Lobo, K. Cooper, N. Beattie, D. Ritchie, and M. Pepper, "Electrically driven single-photon source," Science **295**, 102 (2002).

[45] C. Santori, D. Fattal, J. Vuckovic, G. Solomon, and Y. Yamamoto, "Indistinguishable photons from a single-photon device," Nature **419**, 594–597 (2002).

[46] R. Stevenson, R. Young, P. Atkinson, K. Cooper, D. Ritchie, and A. Shields, "A semiconductor source of triggered entangled photon pairs," Nature **439**, 179–182 (2006).

[47] A. Dousse, J. Suffczyński, A. Beveratos, O. Krebs, A. Lemaître, I. Sagnes, J. Bloch, P. Voisin, and P. Senellart, "Ultrabright source of entangled photon pairs," Nature **466**, 217–220 (2010).

[48] R. Patel, A. Bennett, K. Cooper, P. Atkinson, C. Nicoll, D. Ritchie, and A. Shields, "Postselective two-photon interference from a continuous nonclassical stream of photons emitted by a quantum dot," Physical Review Letters **100**, 207405 (2008).

[49] K. Sanaka, A. Pawlis, T. Ladd, K. Lischka, and Y. Yamamoto, "Indistinguishable photons from independent semiconductor nanostructures," Physical Review Letters **103**, 53601 (2009).

[50] E. Flagg, A. Muller, S. Polyakov, A. Ling, A. Migdall, and G. Solomon, "Interference of single photons from two separate semiconductor quantum dots," Phys. Rev. Lett. **104**, 137401 (2010).

[51] S. Kako, C. Santori, K. Hoshino, S. Götzinger, Y. Yamamoto, and Y. Arakawa, "A gallium nitride single-photon source operating at 200 k," Nature Materials **5**, 887–892 (2006).

[52] A. Jarjour, R. Oliver, and R. Taylor, "Nitride-based quantum dots for single photon source applications," Physica Status Solidi (a) **206**, 2510–2523 (2009).

[53] K. Sebald, J. Kalden, H. Lohmeyer, and J. Gutowski, "Optical properties of single InGaN quantum dots and their devices," Physica Status Solidi (b) **248**, 1777–1786 (2011).

[54] I. Aharonovich, S. Castelletto, D. Simpson, C. Su, A. Greentree, and S. Prawer, "Diamond-based single-photon emitters," Reports on Progress in Physics **74**, 076501 (2011).

[55] R. Brouri, A. Beveratos, J. Poizat, and P. Grangier, "Photon antibunching in the fluorescence of individual color centers in diamond," Optics Letters **25**, 1294–1296 (2000).

[56] C. Kurtsiefer, S. Mayer, P. Zarda, and H. Weinfurter, "Stable solid-state source of single photons," Physical Review Letters **85**, 290–293 (2000).

[57] A. Beveratos, R. Brouri, T. Gacoin, J. Poizat, and P. Grangier, "Nonclassical radiation from diamond nanocrystals," Physical Review A **64**, 061802 (2001).

[58] A. Lohrmann, S. Pezzagna, I. Dobrinets, P. Spinicelli, V. Jacques, J. Roch, J. Meijer, and A. Zaitsev, "Diamond based light-emitting diode for visible single-photon emission at room temperature," Applied Physics Letters **99**, 251106–251106 (2011).

[59] H. Bernien, L. Childress, L. Robledo, M. Markham, D. Twitchen, and R. Hanson, "Two-photon quantum interference from separate nitrogen vacancy centers in diamond," Phys. Rev. Lett. **108**, 043604 (2012).

[60] A. Sipahigil, M. Goldman, E. Togan, Y. Chu, M. Markham, D. Twitchen, A. Zibrov, A. Kubanek, and M. Lukin, "Quantum interference of single photons from remote nitrogen-vacancy centers in diamond," Arxiv preprint arXiv:1112.3975 (2011).

[61] W. Louisell, A. Yariv, and A. Siegman, "Quantum fluctuations and noise in parametric processes. I." Physical Review **124**, 1646 (1961).

[62] B. Zel'Dovich and D. Klyshko, "Field statistics in parametric luminescence," ZhETF Pis ma Redaktsiiu **9**, 69 (1969).

[63] D. Burnham and D. Weinberg, "Observation of simultaneity in parametric production of optical photon pairs," Physical Review Letters **25**, 84–87 (1970).

[64] R. Byer, "Nonlinear optics and solid-state lasers: 2000," IEEE Journal of Selected Topics in Quantum Electronics **6**, 911–930 (2000).

[65] Y. Shih, "Entangled biphoton source-property and preparation," Reports on Progress in Physics **66**, 1009 (2003).

[66] R. Rangarajan, A. U'Ren, and P. Kwiat, "Polarization dependence on downconversion emission angle: investigation of the 'Migdall effect'," J. Mod. Opt. **58**, 312–317 (2011).

[67] P. Kwiat, K. Mattle, H. Weinfurter, A. Zeilinger, A. Sergienko, and Y. Shih, "New high-intensity source of polarization-entangled photon pairs," Physical Review Letters **75**, 4337–4341 (1995).

[68] P. H. Shun, "Towards a high quality polarization-entangled multi-photon source," (2009).

[69] D. Nikogosyan, *Nonlinear optical crystals: a complete survey* (Springer, 2005).

[70] C. Chen, B. Wu, A. Jiang, and G. You, "A new-type ultraviolet SHG crystal: β-BaB_2O_4," Sci. Sin. Ser. B **28**, 235 (1985).

[71] D. Nikogosyan, "Beta barium borate (BBO)," Applied Physics A: Materials Science & Processing **52**, 359–368 (1991).

[72] J. Armstrong, N. Bloembergen, J. Ducuing, and P. Pershan, "Interactions between light waves in a nonlinear dielectric," Physical Review **127**, 1918 (1962).

[73] L. Myers, R. Eckardt, M. Fejer, R. Byer, W. Bosenberg, and J. Pierce, "Quasi-phase-matched optical parametric oscillators in bulk periodically poled $LiNbO_3$," Journal of the Optical Society of America B **12**, 2102–2116 (1995).

[74] E. Lim, M. Fejer, and R. Byer, "Second-harmonic generation of green light in periodically poled planar Lithium Niobate waveguide," Electronics Letters **25**, 174–175 (1989).

[75] M. Bortz, M. Arbore, and M. Fejer, "Quasi-phase-matched optical parametric amplification and oscillation in periodically poled $LiNbO_3$ waveguides," Optics Letters **20**, 49–51 (1995).

[76] G. Magel, M. Fejer, and R. Byer, "Quasi-phase-matched second-harmonic generation of blue light in periodically poled $LiNbO_3$," Applied Physics Letters **56**, 108–110 (1990).

[77] Y. Lu, L. Mao, and N. Ming, "Blue-light generation by frequency doubling of an 810-nm cw GaAlAs diode laser in a quasi-phase-matched $LiNbO_3$ crystal," Optics Letters **19**, 1037–1039 (1994).

[78] M. Angell, R. Emerson, J. Hoyt, J. Gibbons, L. Eyres, M. Bortz, and M. Fejer, "Growth of alternating $< 100 > / < 111 >$-oriented II-VI regions for quasi-phase-matched nonlinear optical devices on GaAs substrates," Applied Physics Letters **64**, 3107–3109 (1994).

[79] L. Eyres, P. Tourreau, T. Pinguet, C. Ebert, J. Harris, M. Fejer, L. Becouarn, B. Gerard, and E. Lallier, "All-epitaxial fabrication of thick, orientation-patterned GaAs films for nonlinear optical frequency conversion," Applied Physics Letters **79**, 904 (2001).

[80] K. Vodopyanov, O. Levi, P. Kuo, T. Pinguet, J. Harris, M. Fejer, B. Gerard, L. Becouarn, and E. Lallier, "Optical parametric oscillation in quasi-phase-matched GaAs," Optics Letters **29**, 1912–1914 (2004).

[81] M. Yamada, N. Nada, M. Saitoh, and K. Watanabe, "First-order quasi-phase matched $LiNbO_3$ waveguide periodically poled by applying an external field for efficient blue second-harmonic generation," Applied Physics Letters **62**, 435–436 (1993).

[82] Q. Zhang, H. Takesue, C. Langrock, X. Xie, M. Fejer, and Y. Yamamoto, "Hong–Ou–Mandel dip using degenerate photon pairs from a single periodically poled Lithium Niobate waveguide with integrated mode demultiplexer," Japanese Journal of Applied Physics **49**, 4401 (2010).

[83] A. S. Solntsev, A. A. Sukhorukov, D. N. Neshev, and Y. S. Kivshar, "Spontaneous parametric down-conversion and quantum walks in arrays of quadratic nonlinear waveguides," Phys. Rev. Lett. **108**, 023601 (2012).

[84] M. Aspelmeyer, "Quantum optics: Enlightened chips," Nature Photonics **1**, 94–95 (2007).

[85] L. Lanco, S. Ducci, J. Likforman, X. Marcadet, J. van Houwelingen, H. Zbinden, G. Leo, and V. Berger, "Semiconductor waveguide source of counterpropagating twin photons," Physical Review Letters **97**, 173901 (2006).

[86] X. Caillet, A. Orieux, A. Lemaître, P. Filloux, I. Favero, G. Leo, and S. Ducci, "Two-photon interference with a semiconductor integrated source at room temperature," Optics Express **18**, 9967–9975 (2010).

[87] C. Santori, "Generation of nonclassical light using semiconductor quantum dots," Ph.D. thesis, stanford university (2003).

[88] L. Mandel, "Quantum effects in one-photon and two-photon interference," Reviews of Modern Physics **71**, 274–282 (1999).

[89] D. Colladon, "On the reflections of a ray of light inside a parabolic liquid stream," Comptes Rendus **15**, 800–802 (1842).

[90] J. Hecht, "Illuminating the origin of light guiding," Optics and Photonics News **10**, 26 (1999).

[91] W. Bond, B. Cohen, R. Leite, and A. Yariv, "Observation of the dielectric-waveguide mode of light propagation in pn junctions," Applied Physics Letters **2**, 57–59 (1963).

[92] R. Shubert and J. Harris, "Optical surface waves on thin films and their application to integrated data processors," IEEE Transactions on Microwave Theory and Techniques **16**, 1048–1054 (1968).

[93] A. Yariv, "The beginnings of optoelectronic integrated circuitsa personal perspective," Journal of Lightwave Technology **26**, 1172–1175 (2008).

[94] S. Miller, "Integrated optics- an introduction," Bell System Technical Journal **48**, 2059–2069 (1969).

[95] S. Miller, "This week's citation classic," Current Contents **5**, 141 (1979).

[96] R. V. Pole, S. E. Miller, J. H. Harris, and P. K. Tien, "Integrated optics and guided waves-a report of the topical meeting." Applied Optics **11**, 1675–1685 (1972).

[97] R. Hunsperger, *Integrated Optics: Theory and Technology*, Advanced texts in physics (Springer, 2009).

[98] T. Izawa and H. Nakagome, "Optical waveguide formed by electrically induced migration of ions in glass plates," Applied Physics Letters **21**, 584–586 (1972).

[99] R. Ramaswamy and R. Srivastava, "Ion-exchanged glass waveguides: a review," Journal of Lightwave Technology **6**, 984–1000 (1988).

[100] P. Townsend, P. Chandler, and L. Zhang, *Optical effects of ion implantation*, vol. 13 (Cambridge Univ Press, 2006).

[101] K. Davis, K. Miura, N. Sugimoto, and K. Hirao, "Writing waveguides in glass with a femtosecond laser," Optics Letters **21**, 1729–1731 (1996).

[102] S. Nolte, M. Will, J. Burghoff, and A. Tuennermann, "Femtosecond waveguide writing: a new avenue to three-dimensional integrated optics," Applied Physics A: Materials Science & Processing **77**, 109–111 (2003).

[103] J. E. Goell, "Rib waveguide for integrated optical circuits," Appl. Opt. **12**, 2797–2798 (1973).

[104] A. Politi, M. Cryan, J. Rarity, S. Yu, and J. O'Brien, "Silica-on-silicon waveguide quantum circuits," Science **320**, 646 (2008).

[105] J. Matthews, A. Politi, A. Stefanov, and J. O'Brien, "Manipulation of multiphoton entanglement in waveguide quantum circuits," Nature Photonics **3**, 346–350 (2009).

[106] A. Peruzzo, A. Laing, A. Politi, T. Rudolph, and J. O'Brien, "Multimode quantum interference of photons in multiport integrated devices," Nature communications **2**, 224 (2011).

[107] P. Shadbolt, M. Verde, A. Peruzzo, A. Politi, A. Laing, M. Lobino, J. Matthews, and J. O'Brien, "Generating, manipulating and measuring entanglement and mixture with a reconfigurable photonic circuit," Nature Photonics **6**, 45–49 (2012).

[108] G. Marshall, A. Politi, J. Matthews, P. Dekker, M. Ams, M. Withford, and J. O'Brien, "Laser written waveguide photonic quantum circuits," Optics Express **17**, 12546–12554 (2009).

[109] G. Marshall, A. Jesacher, A. Thayil, M. Withford, and M. Booth, "Three-dimensional imaging of direct-written photonic structures," Optics Letters **36**, 695–697 (2011).

[110] B. Smith, D. Kundys, N. Thomas-Peter, P. Smith, and I. Walmsley, "Phase-controlled integrated photonic quantum circuits." Optics Express **17**, 13516 (2009).

[111] N. Thomas-Peter, N. Langford, A. Datta, L. Zhang, B. Smith, J. Spring, B. Metcalf, H. Coldenstrodt-Ronge, M. Hu, J. Nunn *et al.*, "Integrated photonic sensing," New Journal of Physics **13**, 055024 (2011).

[112] L. Sansoni, F. Sciarrino, G. Vallone, P. Mataloni, A. Crespi, R. Ramponi, and R. Osellame, "Polarization entangled state measurement on a chip," Physical Review Letters **105**, 200503 (2010).

[113] A. Crespi, R. Ramponi, R. Osellame, L. Sansoni, I. Bongioanni, F. Sciarrino, G. Vallone, and P. Mataloni, "Integrated photonic quantum gates for polarization qubits," Nature Communications **2**, 566 (2011).

[114] L. Sansoni, F. Sciarrino, G. Vallone, P. Mataloni, A. Crespi, R. Ramponi, and R. Osellame, "Two-particle bosonic-fermionic quantum walk via integrated photonics," Phys. Rev. Lett. **108**, 010502 (2012).

[115] A. Peruzzo, M. Lobino, J. Matthews, N. Matsuda, A. Politi, K. Poulios, X. Zhou, Y. Lahini, N. Ismail, K. Wörhoff *et al.*, "Quantum walks of correlated photons," Science **329**, 1500 (2010).

[116] J. Owens, M. Broome, D. Biggerstaff, M. Goggin, A. Fedrizzi, T. Linjordet, M. Ams, G. Marshall, J. Twamley, M. Withford *et al.*, "Two-photon quantum walks in an elliptical direct-write waveguide array," New Journal of Physics **13**, 075003 (2011).

[117] D. Bonneau, M. Lobino, P. Jiang, C. M. Natarajan, M. G. Tanner, R. H. Hadfield, S. N. Dorenbos, V. Zwiller, M. G. Thompson, and J. L. O'Brien, "Fast path and polarization manipulation of telecom wavelength single photons in Lithium Niobate waveguide devices," Phys. Rev. Lett. **108**, 053601 (2012).

[118] Y. Zhang, L. McKnight, E. Engin, I. Watson, M. Cryan, E. Gu, M. Thompson, S. Calvez, J. OBrien, and M. Dawson, "GaN directional couplers for integrated quantum photonics," Applied Physics Letters **99**, 161119 (2011).

[119] D. Bonneau, E. Engin, K. Ohira, N. Suzuki, H. Yoshida, N. Iizuka, M. Ezaki, C. M. Natarajan, M. G. Tanner, R. H. Hadfield, S. N. Dorenbos, V. Zwiller, J. L. O'Brien, and M. G. Thompson, "Quantum interference and manipulation of entanglement in silicon wire waveguide quantum circuits," Arxiv preprint arXiv:1201.6537v1 (2012).

[120] A. Martin, O. Alibart, M. De Micheli, D. Ostrowsky, and S. Tanzilli, "A quantum relay chip based on telecommunication integrated optics technology," New Journal of Physics **14**, 25002–25014 (2012).

[121] H. Hertz, "Ueber einen einfluss des ultravioletten lichtes auf die electrische entladung," Annalen der Physik **267**, 983–1000 (1887).

[122] L. Austin and H. Starke, "Ueber die reflexion der kathodenstrahlen und eine damit verbundene neue erscheinung secundärer emission," Annalen der Physik **314**, 271–292 (1902).

[123] G. Morton, "Photomultipliers for scintillation counting," RCA Rev. **10**, 525 (1949).

[124] R. Hadfield, "Single-photon detectors for optical quantum information applications," Nature Photonics **3**, 696–705 (2009).

[125] J. P. Sprengers, A. Gaggero, D. Sahin, S. Jahanmirinejad, G. Frucci, F. Mattioli, R. Leoni, J. Beetz, M. Lermer, M. Kamp, S. Hofling, R. Sanjines, and A. Fiore, "Waveguide superconducting single-photon detectors for integrated quantum photonic circuits," Applied Physics Letters **99**, 181110 (2011).

[126] T. Gerrits, N. Thomas-Peter, J. Gates, A. Lita, B. Metcalf, B. Calkins, N. Tomlin, A. Fox, A. Linares, J. Spring *et al.*, "On-chip, photon-number-resolving, telecommunication-band detectors for scalable photonic information processing," Physical Review A **84**, 060301 (2011).

[127] Y. Zhang, L. McKnight, Z. Tian, S. Calvez, E. Gu, and M. Dawson, "Large cross-section edge-coupled diamond waveguides," Diamond and Related Materials **20**, 564–567 (2011).

[128] K. Kuhn, C. Kenyon, A. Kornfeld, M. Liu, A. Maheshwari, W. Shih, S. Sivakumar, G. Taylor, P. VanDerVoorn, and K. Zawadzki, "Managing process variation in Intels 45 nm CMOS technology," Intel Technology Journal **12**, 93–109 (2008).

[129] P. Naulleau, C. Anderson, L. Baclea-An, P. Denham, S. George, K. Goldberg, G. Jones, B. McClinton, R. Miyakawa, I. Mochi *et al.*, "Using synchrotron light to accelerate EUV resist and mask materials learning," in *Proceedings of SPIE* **7985**, 798509 (2011).

[130] T. Brunner, "Why optical lithography will live forever," Journal of Vacuum Science & Technology B: Microelectronics and Nanometer Structures **21**, 2632 (2003).

[131] D. Meyerhofer, "Characteristics of resist films produced by spinning," Journal of Applied Physics **49**, 3993–3997 (1978).

[132] J. Pettinato and D. Pillai, "Technology decisions to minimize 450-mm wafer size transition risk," IEEE Transactions on Semiconductor Manufacturing **18**, 501–509 (2005).

[133] C. Chien, J. Wang, T. Chang, and W. Wu, "Economic analysis of 450mm wafer migration," in "International Symposium on Semiconductor Manufacturing," (IEEE, 2007), pp. 1–4.

[134] M. Chan, "Another look at edge bead," Proceedings Kodak Microelectronics Seminar pp. 16–32 (1979).

[135] H. Choi, P. Edwards, C. Liu, C. Jeon, R. Martin, I. Watson, M. Dawson, S. Tripathy, and S. Chua, "Sub-micron InGaN ring structures for high-efficiency LEDs," Physica Status Solidi (c) **1**, 202–205 (2004).

[136] M. Häfner, C. Pruss, and W. Osten, "Laser direct writing," Optik & Photonik **6**, 40–43 (2011).

[137] C. Rensch, S. Hell, M. Schickfus, and S. Hunklinger, "Laser scanner for direct writing lithography," Applied optics **28**, 3754–3758 (1989).

[138] H. Sun and S. Kawata, "Two-photon laser precision microfabrication and its applications to micro-nano devices and systems," Journal of lightwave technology **21**, 624 (2003).

[139] M. Deubel, G. Von Freymann, M. Wegener, S. Pereira, K. Busch, and C. Soukoulis, "Direct laser writing of three-dimensional photonic-crystal templates for telecommunications," Nature Materials **3**, 444–447 (2004).

[140] R. Krchnavek, G. Lalk, and D. Hartman, "Laser direct writing of channel waveguides using spin-on polymers," Journal of Applied Physics **66**, 5156–5160 (1989).

[141] M. Svalgaard, "Direct writing of planar waveguide power splitters and directional couplers using a focused ultraviolet laser beam," Electronics Letters **33**, 1694–1695 (1997).

[142] D. Elfström, B. Guilhabert, J. McKendry, S. Poland, Z. Gong, D. Massoubre, E. Richardson, B. Rae, G. Valentine, G. Blanco-Gomez *et al.*, "Mask-less ultraviolet photolithography based on CMOS-driven micro-pixel light emitting diodes," Optics Express **17**, 23522–23529 (2009).

[143] M. Wu, Z. Gong, D. Massoubre, Y. Zhang, E. Richardson, E. Gu, and M. Dawson, "Inkjet printed conductive silver tracks applied to GaN-based microstructured light emitting diodes," Applied Physics A: Materials Science and Processing **104**, 1003–1009 (2011).

[144] M. Wu, Z. Gong, A. Kuehne, A. Kanibolotsky, Y. Chen, I. Perepichka, A. Mackintosh, E. Gu, P. Skabara, R. Pethrick *et al.*, "Hybrid GaN/organic microstructured light-emitting devices via ink-jet printing," Optics Express **17**, 16436–16443 (2009).

[145] K. Lien and G. Lee, "Miniaturization of molecular biological techniques for gene assay," Analyst **135**, 1499–1518 (2010).

[146] R. Deegan, O. Bakajin, and T. Dupont, "Capillary flow as the cause of ring stains from dried liquid drops," Nature **389**, 827–829 (1997).

[147] J. Batchelor, E. Parker, J. Miller, V. Sanchez-Romaguera, and S. Yeates, "Inkjet printing of frequency selective surfaces," Electronics Letters **45**, 7–8 (2009).

[148] H. Conrads and M. Schmidt, "Plasma generation and plasma sources," Plasma Sources Science and Technology **9**, 441 (2000).

[149] S. O'Brein, "The chemistry of the semiconductor industry," Chem. Soc. Rev. **25**, 393–400 (1996).

[150] J. Wang, *Modern Thermodynamics: Based on the Extended Carnot Theorem* (Springer, 2011).

[151] J. Hershey, *The book of diamonds: their curious lore, properties, tests and synthetic manufacture* (Hearthside Press, 1940).

[152] P. Lu, N. Yao, J. So, G. Harlow, J. Lu, G. Wang, and P. Chaikin, "The earliest use of corundum and diamond, in prehistoric china," Archaeometry **47**, 1–12 (2005).

[153] E. Erlich and W. Hausel, *Diamond deposits: origin, exploration, and history of discovery* (Society for Mining Metallurgy, 2002).

[154] K. Hughen, S. Lehman, J. Southon, J. Overpeck, O. Marchal, C. Herring, and J. Turnbull, "14C activity and global carbon cycle changes over the past 50,000 years," Science **303**, 202 (2004).

[155] M. J. Walter, S. C. Kohn, D. Araujo, G. P. Bulanova, C. B. Smith, E. Gaillou, J. Wang, A. Steele, and S. B. Shirey, "Deep mantle cycling of oceanic crust: Evidence from diamonds and their mineral inclusions," Science **334**, 54–57 (2011).

[156] J. Hannay, "On the artificial formation of the diamond," Proceedings of the Royal Society of London **30**, 450–461 (1879).

[157] J. Hannay, "Artificial diamonds," Nature **22**, 241–241 (1880).

[158] R. Hazen, *The diamond makers* (Cambridge Univ Pr, 1999).

[159] F. Bundy, H. Hall, H. Strong, and R. Wentorf, "Man-made diamonds," Nature **176**, 51–55 (1955).

[160] H. Bovenkerk, F. Bundy, H. Hall, H. Strong, and R. Wentorf, "Preparation of diamond," Nature **184**, 1094–8 (1959).

[161] S. Ferro, "Synthesis of diamond," J. Mater. Chem. **12**, 2843–2855 (2002).

[162] W. Eversole, "Synthesis of diamond by deposition on seed crystals," US patent No. 3030187 (1962).

[163] J. Angus, H. Will, and W. Stanko, "Growth of diamond seed crystals by vapor deposition," Journal of Applied Physics **39**, 2915–2922 (1968).

[164] J. Angus, A. Argoitia, R. Gat, Z. Li, M. Sunkara, L. Wang, and Y. Wang, "Chemical vapour deposition of diamond," Philosophical Transactions of the Royal Society of London. Series A: Physical and Engineering Sciences **342**, 195–208 (1993).

[165] V. Spitsyn Boris, L. Bouilov Leonid, and E. Alexenko Alexander, "Origin, state of the art and some prospects of the diamond cvd," Brazilian Journal of Physics **30**, 471–481 (2000).

[166] Y. Meng, C. Yan, S. Krasnicki, Q. Liang, J. Lai, H. Shu, T. Yu, A. Steele, H. Mao, and R. Hemley, "High optical quality multicarat single crystal diamond produced by chemical vapor deposition," Physica Status Solidi (a) **209**, 100–100 (2012).

[167] W. Nelissen, H. Godfried, E. Houwman, P. Kriele, J. Lamers, G. Pels, B. Van Oerle, P. Spaay, M. McClymont, C. Wort *et al.*, "Single crystal diamond elements having convex surfaces and methods of its fabrication," (2006). US Patent App. 11/995,067.

[168] P. Siyushev, F. Kaiser, V. Jacques, I. Gerhardt, S. Bischof, H. Fedder, J. Dodson, M. Markham, D. Twitchen, F. Jelezko *et al.*, "Monolithic diamond optics for single photon detection," Applied Physics Letters **97**, 241902–241902 (2010).

[169] J. Hadden, J. Harrison, A. Stanley-Clarke, L. Marseglia, Y. Ho, B. Patton, J. OBrien, and J. Rarity, "Strongly enhanced photon collection from diamond defect centers under microfabricated integrated solid immersion lenses," Applied Physics Letters **97**, 241901 (2010).

[170] L. Marseglia, J. Hadden, A. Stanley-Clarke, J. Harrison, B. Patton, Y. Ho, B. Naydenov, F. Jelezko, J. Meijer, P. Dolan *et al.*, "Nanofabricated solid

immersion lenses registered to single emitters in diamond," Applied Physics Letters **98**, 133107 (2011).

[171] L. Robledo, L. Childress, H. Bernien, B. Hensen, P. Alkemade, and R. Hanson, "High-fidelity projective read-out of a solid-state spin quantum register," Nature **477**, 574–578 (2011).

[172] A. Pritchard, C. Goring, and W. Kelsall, *The Microscopic Cabinet of Select Animated Objects: With a Description of the Jewel and Doublet Microscope, Test Objects, &c. to which are Subjoined, Memoirs on the Verification of Microscopic Phenomena, and an Exact Method of Appreciating the Quality of Microscopes and Engiscopes by CR Goring* (Whittaker, Treacher, and Arnot, Ave-Maria-Lane, 1832).

[173] E. Woerner, C. Wild, W. Mueller-Sebert, and P. Koidl, "CVD-diamond optical lenses," Diamond and Related Materials **10**, 557–560 (2001).

[174] M. Karlsson and F. Nikolajeff, "Diamond micro-optics: microlenses and antireflection structured surfaces for the infrared spectral region," Optics Express **11**, 502–507 (2003).

[175] E. Gu, H. Choi, C. Liu, C. Griffin, J. Girkin, I. Watson, M. Dawson, G. McConnell, and A. Gurney, "Reflection/transmission confocal microscopy characterization of single-crystal diamond microlens arrays," Applied Physics Letters **84**, 2754 (2004).

[176] H. Choi, E. Gu, C. Liu, C. Griffin, J. Girkin, I. Watson, and M. Dawson, "Fabrication of natural diamond microlenses by plasma etching," Journal of Vacuum Science & Technology B: Microelectronics and Nanometer Structures **23**, 130–132 (2005).

[177] C. Lee, H. Choi, E. Gu, M. Dawson, and H. Murphy, "Fabrication and characterization of diamond micro-optics," Diamond and Related Materials **15**, 725–728 (2006).

[178] C. Lee, E. Gu, M. Dawson, I. Friel, and G. Scarsbrook, "Etching and micro-optics fabrication in diamond using chlorine-based inductively-coupled plasma," Diamond Relat. Mater. **17**, 1292–1296 (2008).

[179] M. Shinoda, K. Saito, T. Kondo, A. Nakaoki, M. Furuki, M. Takeda, M. Yamamoto, T. Schaich, B. van Oerle, H. Godfried *et al.*, "High-density near-field readout using a diamond solid immersion lens," in "International Sym-

posium on Optical Memory and Optical Data Storage," (Optical Society of America, 2005).

[180] V. Zwiller and G. Björk, "Improved light extraction from emitters in high refractive index materials using solid immersion lenses," Journal of Applied Physics **92**, 660 (2002).

[181] S. Castelletto, J. Harrison, L. Marseglia, A. Stanley-Clarke, B. Gibson, B. Fairchild, J. Hadden, Y. Ho, M. Hiscocks, K. Ganesan *et al.*, "Diamond-based structures to collect and guide light," New Journal of Physics **13**, 025020 (2011).

[182] M. Born, E. Wolf, and A. Bhatia, *Principles of optics: electromagnetic theory of propagation, interference and diffraction of light* (Cambridge Univ Pr, 1999).

[183] Z. Popovic, R. Sprague, and G. Connell, "Technique for monolithic fabrication of microlens arrays," Applied optics **27**, 1281–1284 (1988).

[184] D. Daly, R. Stevens, M. Hutley, and N. Davies, "The manufacture of microlenses by melting photoresist," Measurement Science and Technology **1**, 759 (1990).

[185] D. Daly, *Microlens arrays* (CRC, 2001).

[186] C. Jones, B. Matthews, D. Purdy, and N. Metcalfe, "Fabrication and assessment of optically immersed CdHgTe detector arrays," Semiconductor Science and Technology **6**, C110 (1991).

[187] P. Savander, "Microlens arrays etched into glass and silicon," Optics and Lasers in Engineering **20**, 97–107 (1994).

[188] M. Stern and T. Jay, "Dry etching: path to coherent refractive microlens arrays," Proceedings of SPIE **283**, 1993 (1992).

[189] M. Stern and T. Jay, "Dry etching for coherent refractive microlens arrays," Optical Engineering **33**, 3547–3551 (1994).

[190] M. Eisner and J. Schwider, "Transferring resist microlenses into silicon by reactive ion etching," Optical Engineering **35**, 2979 (1996).

[191] M. Severi and P. Mottier, "Etching selectivity control during resist pattern transfer into silica for the fabrication of microlenses with reduced spherical aberration," Optical engineering **38**, 146 (1999).

[192] P. Nussbaum and H. Herzig, "Low numerical aperture refractive microlenses in fused silica," Optical Engineering **40**, 1412 (2001).

[193] R. Voelkel, M. Eisner, and K. Weible, "Fabrication of aspherical microlenses in fused silica and silicon," Proceedings of SPIE **4440**, 40 (2001).

[194] D. Fletcher, K. Crozier, K. Guarini, S. Minne, G. Kino, C. Quate, and K. Goodson, "Microfabricated silicon solid immersion lens," Journal of Microelectromechanical Systems **10**, 450–459 (2001).

[195] E. Strzelecka, G. Robinson, L. Coldren, and E. Hu, "Fabrication of refractive microlenses in semiconductors by mask shape transfer in reactive ion etching," Microelectronic engineering **35**, 385–388 (1997).

[196] T. Oder, J. Shakya, J. Lin, and H. Jiang, "Nitride microlens arrays for blue and ultraviolet wavelength applications," Applied Physics Letters **82**, 3692–3694 (2003).

[197] Y. Song, S. Bae, J. Yu, and Y. Lee, "Closely packed and aspect-ratio-controlled antireflection subwavelength gratings on GaAs using a lenslike shape transfer," Optics Letters **34**, 1702–1704 (2009).

[198] J. Leem, Y. Song, and J. Yu, "Six-fold hexagonal symmetric nanostructures with various periodic shapes on GaAs substrates for efficient antireflection and hydrophobic properties," Nanotechnology **22**, 485304 (2011).

[199] S. Wu, S. Yu, D. Ding, S. Johnson, and Y. Zhang, "Ultrahigh luminescence extraction via the monolithic integration of a light emitting active region with a semiconductor hemisphere," Journal of Vacuum Science & Technology B: Microelectronics and Nanometer Structures **29**, 031213 (2011).

[200] S. Park, H. Jeon, Y. Sung, and G. Yeom, "Refractive sapphire microlenses fabricated by chlorine-based inductively coupled plasma etching," Applied Optics **40**, 3698–3702 (2001).

[201] H. Choi, C. Liu, E. Gu, G. McConnell, J. Girkin, I. Watson, and M. Dawson, "GaN micro-light-emitting diode arrays with monolithically integrated sapphire microlenses," Applied Physics Letters **84**, 2253 (2004).

[202] M. Khizar, Z. Fan, K. Kim, J. Lin, and H. Jiang, "Nitride deep-ultraviolet light-emitting diodes with microlens array," Applied Physics Letters **86**, 173504 (2005).

[203] Y. Ando, Y. Nishibayashi, K. Kobashi, T. Hirao, and K. Oura, "Smooth and high-rate reactive ion etching of diamond," Diamond and Related Materials **11**, 824–827 (2002).

[204] W. Stober, A. Fink, and E. Bohn, "Controlled growth of monodisperse silica spheres in the micron size range," Journal of colloid and interface science **26**, 62–69 (1968).

[205] U. Fischer and H. Zingsheim, "Submicroscopic pattern replication with visible light," Journal of Vacuum Science and Technology **19**, 881–885 (1981).

[206] H. Deckman and J. Dunsmuir, "Natural lithography," Applied Physics Letters **41**, 377–379 (1982).

[207] J. Hulteen and R. Van Duyne, "Nanosphere lithography: A materials general fabrication process for periodic particle array surfaces," Journal of Vacuum Science & Technology A: Vacuum, Surfaces, and Films **13**, 1553–1558 (1995).

[208] V. Astratov, Y. Vlasov, O. Karimov, A. Kaplyanskii, Y. Musikhin, N. Bert, V. Bogomolov, and A. Prokofiev, "Photonic band gaps in 3D ordered fcc silica matrices," Physics Letters A **222**, 349–353 (1996).

[209] H. Míguez, F. Meseguer, C. López, Á. Blanco, J. Moya, J. Requena, A. Mifsud, and V. Fornés, "Control of the photonic crystal properties of fcc-packed submicrometer SiO_2 spheres by sintering," Advanced Materials **10**, 480–483 (1998).

[210] C. Hsu, S. Connor, M. Tang, and Y. Cui, "Wafer-scale silicon nanopillars and nanocones by Langmuir–Blodgett assembly and etching," Applied Physics Letters **93**, 133109 (2008).

[211] P. Jiang and M. McFarland, "Large-scale fabrication of wafer-size colloidal crystals, macroporous polymers and nanocomposites by spin-coating," Journal of the American Chemical Society **126**, 13778–13786 (2004).

[212] J. Huang, F. Kim, A. Tao, S. Connor, and P. Yang, "Spontaneous formation of nanoparticle stripe patterns through dewetting," Nature Materials **4**, 896–900 (2005).

[213] S. Jeong, L. Hu, H. Lee, E. Garnett, J. Choi, and Y. Cui, "Fast and scalable printing of large area monolayer nanoparticles for nanotexturing applications," Nano Lett **10**, 2989–2994 (2010).

[214] D. Erenso, A. Shulman, J. Curtis, and S. Elrod, "Formation of synthetic structures with micron size silica beads using optical tweezer," Journal of Modern Optics **54**, 1529–1536 (2007).

[215] Á. Marín, H. Gelderblom, D. Lohse, and J. Snoeijer, "Order-to-disorder transition in ring-shaped colloidal stains," Physical Review Letters **107**, 85502 (2011).

[216] D. Flamm, *Mechanisms of silicon etching in fluorine-and chlorine-containing plasmas* (Electronics Research Laboratory, College of Engineering, University of California, 1990).

[217] T. Babinec, B. Hausmann, M. Khan, Y. Zhang, J. Maze, P. Hemmer, and M. Loncar, "A diamond nanowire single-photon source." Nature Nanotechnology **5**, 195 (2010).

[218] A. Dousse, L. Lanco, J. Suffczyński, E. Semenova, A. Miard, A. Lemaître, I. Sagnes, C. Roblin, J. Bloch, and P. Senellart, "Controlled light-matter coupling for a single quantum dot embedded in a pillar microcavity using far-field optical lithography," Physical Review Letters **101**, 267404 (2008).

[219] J. Riedrich-Möller, L. Kipfstuhl, C. Hepp, E. Neu, C. Pauly, F. Mücklich, A. Baur, M. Wandt, S. Wolff, M. Fischer, S. Gsell, M. Schreck, and C. Becher, "One-and two-dimensional photonic crystal microcavities in single crystal diamond," Nature Nanotechnology **7**, 69 (2012).

[220] M. Dresselhaus and R. Kalish, *Ion implantation in diamond, graphite, and related materials*, vol. 15 (Springer-Verlag Berlin, 1992).

[221] S. Prawer, "Ion implantation of diamond and diamond films," Diamond and Related Materials **4**, 862–872 (1995).

[222] R. Kalish, "The role of ion-implantation in the realization of spintronic devices in diamond," Nuclear Instruments and Methods in Physics Research Section B: Beam Interactions with Materials and Atoms **272**, 42–48 (2011).

[223] R. Hines, "Radiation damage of diamond by 20-kev Carbon ions," Physical Review **138**, 1747–1751 (1965).

[224] P. Olivero, S. Calusi, L. Giuntini, S. Lagomarsino, A. Lo Giudice, M. Massi, S. Sciortino, M. Vannoni, and E. Vittone, "Controlled variation of the refractive index in ion-damaged diamond," Diamond and Related Materials **19**, 428–431 (2010).

[225] F. Bosia, N. Argiolas, M. Bazzan, P. Olivero, F. Picollo, A. Sordini, M. Vannoni, and E. Vittone, "Modification of the structure of diamond with MeV ion implantation," Diamond and Related Materials **20**, 774–778 (2011).

[226] S. Lagomarsino, P. Olivero, F. Bosia, M. Vannoni, S. Calusi, L. Giuntini, and M. Massi, "Evidence of light guiding in ion-implanted diamond," Physical Review Letters **105**, 233903 (2010).

[227] A. Battiato, F. Bosia, S. Ferrari, P. Olivero, A. Sytchkova, and E. Vittone, "Spectroscopic measurement of the refractive index of ion-implanted diamond," Optics Letters **37**, 671–673 (2012).

[228] M. W. Geis, D. D. Rathman, and M. Rothschild, Diamond Technology Initiative (Arlington, VA, 1213 July 1988).

[229] N. Parikh, J. Hunn, E. McGucken, M. Swanson, C. White, R. Rudder, D. Malta, J. Posthill, and R. Markunas, "Single-crystal diamond plate liftoff achieved by ion implantation and subsequent annealing," Applied Physics Letters **61**, 3124–3126 (1992).

[230] C. Uzan-Saguy, C. Cytermann, R. Brener, V. Richter, M. Shaanan, and R. Kalish, "Damage threshold for ion-beam induced graphitization of diamond," Applied Physics Letters **67**, 1194–1196 (1995).

[231] I. Bayn, B. Meyler, A. Lahav, J. Salzman, R. Kalish, B. Fairchild, S. Prawer, M. Barth, O. Benson, T. Wolf *et al.*, "Processing of photonic crystal nanocavity for quantum information in diamond," Diamond and Related Materials **20**, 937–943 (2011).

[232] P. Lai, S. Prawer, and L. Bursill, "Recovery of diamond after irradiation at high energy and annealing," Diamond and Related Materials **10**, 82–86 (2001).

[233] P. Olivero, S. Rubanov, P. Reichart, B. Gibson, S. Huntington, J. Rabeau, A. Greentree, J. Salzman, D. Moore, D. Jamieson *et al.*, "Ion-beam-assisted lift-off technique for three-dimensional micromachining of freestanding single-crystal diamond," Advanced Materials **17**, 2427–2430 (2005).

[234] B. Fairchild, P. Olivero, S. Rubanov, A. Greentree, F. Waldermann, R. Taylor, I. Walmsley, J. Smith, S. Huntington, B. Gibson *et al.*, "Fabrication of ultrathin single-crystal diamond membranes," Advanced Materials **20**, 4793–4798 (2008).

[235] A. Stacey, V. Drumm, B. Fairchild, K. Ganesan, S. Rubanov, R. Kalish, B. Cowie, S. Prawer, and A. Hoffman, "Improved diamond surfaces following lift-off and plasma treatments as observed by x-ray absorption spectroscopy," Applied Physics Letters **98**, 181907 (2011).

[236] M. Hiscocks, K. Ganesan, B. Gibson, S. Huntington, F. Ladouceur, and S. Prawer, "Diamond waveguides fabricated by reactive ion etching," Optics Express **16**, 19512–19519 (2008).

[237] M. Hiscocks, K. Ganesan, W. McKenzie, B. Gibson, F. Ladouceur, and S. Prawer, "Towards characterisation of millimetre length waveguides and new fabrication method for nanoscale diamond photonic structures," Diamond and Related Materials **20**, 556–559 (2011).

[238] T. Thi, B. Fernandez, D. Eon, E. Gheeraert, J. Härtwig, T. Lafford, A. Perrat-Mabilon, C. Peaucelle, P. Olivero, and E. Bustarret, "Ultrasmooth single crystal diamond surfaces resulting from implantation and lift-off processes," Physica status solidi. A, Applications and materials science **208**, 2057–2061 (2011).

[239] Y. Tzeng, J. Wei, J. Woo, and W. Lanford, "Free-standing single-crystalline chemically vapor deposited diamond films," Applied Physics Letters **63**, 2216–2218 (1993).

[240] M. Marchywka, P. Pehrsson, D. Vestyck, and D. Moses, "Low energy ion implantation and electrochemical separation of diamond films," Applied Physics Letters **63**, 3521–3523 (1993).

[241] J. Hunn, S. Withrow, C. White, R. Clausing, L. Heatherly, and C. Christensen, "Fabrication of single-crystal diamond microcomponents," Applied Physics Letters **65**, 3072–3074 (1994).

[242] J. Posthill, D. Malta, T. Humphreys, G. Hudson, R. Thomas, R. Rudder, and R. Markunas, "Method of fabricating a free-standing diamond single crystal using growth from the vapor phase," Journal of Applied Physics **79**, 2722–2727 (1996).

[243] C. Wang, E. Hu, J. Yang, and J. Butler, "Fabrication of suspended single crystal diamond devices by electrochemical etch," Journal of Vacuum Science & Technology B: Microelectronics and Nanometer Structures **25**, 730 (2007).

[244] A. Magyar, J. Lee, A. Limarga, I. Aharonovich, F. Rol, D. Clarke, M. Huang, and E. Hu, "Fabrication of thin, luminescent, single-crystal diamond membranes," Applied Physics Letters **99**, 081913 (2011).

[245] J. Lee, I. Aharonovich, A. Magyar, F. Rol, and E. Hu, "Coupling of silicon-vacancy centers to a single crystal diamond cavity," Arxiv preprint arXiv:1111.6852 (2011).

[246] I. Aharonovich, J. Lee, A. Magyar, B. Buckley, C. Yale, D. Awschalom, and E. Hu, "Homoepitaxial growth of single crystal diamond membranes for quantum information processing," Arxiv preprint arXiv:1109.5634 (2011).

[247] Y. Mokuno, A. Chayahara, and H. Yamada, "Synthesis of large single crystal diamond plates by high rate homoepitaxial growth using microwave plasma CVD and lift-off process," Diamond and Related Materials **17**, 415–418 (2008).

[248] Y. Mokuno, A. Chayahara, H. Yamada, and N. Tsubouchi, "Improving purity and size of single-crystal diamond plates produced by high-rate CVD growth and lift-off process using ion implantation," Diamond and Related Materials **18**, 1258–1261 (2009).

[249] H. Yamada, A. Chayahara, Y. Mokuno, N. Tsubouchi, S. Shikata, and N. Fujimori, "Developments of elemental technologies to produce inch-size single-crystal diamond wafers," Diamond and Related Materials **20**, 616–619 (2011).

[250] M. Ray, T. Feygelson, J. Butler, J. Baldwin, B. Houston, B. Pate, and M. Zalalutdinov, "Dissipation in single crystal diamond micromechanical annular plate resonators," Diamond and Related Materials **20**, 1204–1207 (2011).

[251] M. Zalalutdinov, M. Ray, D. Photiadis, J. Robinson, J. Baldwin, J. Butler, T. Feygelson, B. Pate, and B. Houston, "Ultrathin single crystal diamond nanomechanical dome resonators," Nano Letters **11**, 4304–4308 (2011).

[252] M. Liao, S. Hishita, E. Watanabe, S. Koizumi, and Y. Koide, "Suspended single-crystal diamond nanowires for high-performance nanoelectromechanical switches," Advanced materials **22**, 5393–5397 (2010).

[253] M. Liao, Z. Rong, S. Hishita, M. Imura, S. Koizumi, and Y. Koide, "Nanoelectromechanical switch fabricated from single crystal diamond: Experiments and modeling," Diamond and Related Materials **24**, 69–73 (2011).

[254] A. Faraon, P. Barclay, C. Santori, K. Fu, and R. Beausoleil, "Resonant enhancement of the zero-phonon emission from a colour centre in a diamond cavity," Nature Photonics **5**, 301–305 (2011).

[255] A. Faraon, C. Santori, Z. Huang, V. Acosta, and R. Beausoleil, "Coupling of nitrogen-vacancy centers to photonic crystal cavities in monocrystalline diamond," Arxiv preprint arXiv:1202.0806 (2012).

[256] B. Hausmann, B. Shields, Q. Quan, P. Maletinsky, M. McCutcheon, J. Choy, T. Babinec, A. Kubanek, A. Yacoby, M. Lukin *et al.*, "Integrated diamond networks for quantum nanophotonics," Nano Letters **12**, 1578–1582 (2012).

[257] D. Sage, L. Pham, N. Bar-Gill, C. Belthangady, M. Lukin, A. Yacoby, and R. Walsworth, "Efficient photon detection from color centers in a diamond optical waveguide," Arxiv preprint arXiv:1201.0674 (2012).

[258] I. Bayn, B. Meyler, J. Salzman, and R. Kalish, "Triangular nanobeam photonic cavities in single-crystal diamond," New Journal of Physics **13**, 025018 (2011).

[259] T. Babinec, J. Choy, K. Smith, M. Khan, and M. Lončar, "Design and focused ion beam fabrication of single crystal diamond nanobeam cavities," Journal of Vacuum Science & Technology B: Microelectronics and Nanometer Structures **29**, 010601 (2011).

[260] J. Rarity, J. O'Brien, Y. Ho, R. Gibson, J. Harrison, A. Stanley-Clarke, and L. Marseglia, "Photonic crystal defect cavities coupled to N-V centres in diamond," in Proceedings of *CLEO Europe-EQEC*, Munich(2010) .

[261] I. Bayn, A. Bolker, C. Cytermann, B. Meyler, V. Richter, J. Salzman, and R. Kalish, "Diamond processing by focused ion beam—surface damage and recovery," Applied Physics Letters **99**, 183109 (2011).

[262] M. Fischer, R. Brescia, S. Gsell, M. Schreck, T. Brugger, T. Greber, J. Osterwalder, and B. Stritzker, "Growth of twin-free heteroepitaxial diamond on Ir/YSZ/Si (111)," Journal of Applied Physics **104**, 123531–123531 (2008).

[263] K. Petermann, "Properties of optical rib-guides with large cross-section," Archiv fur Electronik und Ubertragungstechnik **30**, 139–140 (1976).

[264] R. Soref, J. Schmidtchen, and K. Petermann, "Large single-mode rib waveguides in GeSi-Si and Si-on-SiO_2," IEEE Journal of Quantum Electronics **27**, 1971–1974 (1991).

[265] S. Pogossian, L. Vescan, and A. Vonsovici, "The single-mode condition for semiconductor rib waveguides with large cross section," Journal of Lightwave Technology **16**, 1851–1853 (1998).

[266] O. Powell, "Single-mode condition for silicon rib waveguides," Journal of Lightwave Technology **20**, 1851–1855 (2002).

[267] J. Xia and J. Yu, "Single-mode condition for silicon rib waveguides with trapezoidal cross-section," Optics communications **230**, 253–257 (2004).

[268] J. Lousteau, D. Furniss, A. Seddon, T. Benson, A. Vukovic, and P. Sewell, "The single-mode condition for silicon-on-insulator optical rib waveguides with large cross section," Journal of Lightwave Technology **22**, 1923–1929 (2004).

[269] A. Rickman, G. Reed, and F. Namavar, "Silicon-on-insulator optical rib waveguide loss and mode characteristics," Journal of Lightwave Technology **12**, 1771–1776 (1994).

[270] L. McKnight, M. Dawson, and S. Calvez, "Diamond raman waveguide lasers: Completely analytical design optimization incorporating scattering losses," IEEE J. Quantum Electron. **47**, 1069–1077 (2011).

[271] U. Demirci, "Droplet-based photoresist deposition," Appl. Phys. Lett. **88**, 144104 (2006).

[272] G. Stringfellow, *Organometallic vapor-phase epitaxy: theory and practice* (Academic Press, 1998).

[273] T. Scott, G. King, and J. Wilson, "Uk patent 778,383.8," (1954).

[274] H. Manasevit, "Single-crystal gallium arsenide on insulating substrates," Applied Physics Letters **12**, 156–159 (1968).

[275] Y. Seki, K. Tanno, K. Iida, and E. Ichiki, "Properties of epitaxial GaAs layers from a Triethyl Gallium and Arsine system," Journal of The Electrochemical Society **122**, 1108 (1975).

[276] R. Dupuis, P. Dapkus, N. Holonyak, E. Rezek, and R. Chin, "Room-temperature laser operation of quantum-well Ga_{1-x} Al_xAs-GaAs laser diodes grown by metalorganic chemical vapor deposition," Applied Physics Letters **32**, 295–297 (1978).

[277] R. Bradley, "MOCVD growth and characterisation of GaAlAs/GaAs double heterostructures for opto-electronic devices," Journal of Crystal Growth **55**, 223–228 (1981).

[278] W. Johnson, J. Parson, and M. Crew, "Nitrogen compounds of Gallium. III," The Journal of Physical Chemistry **36**, 2651–2654 (1932).

[279] S. Strite and H. Morkoc, "GaN, AlN, and InN: a review," Journal of Vacuum Science & Technology B: Microelectronics and Nanometer Structures **10**, 1237–1266 (1992).

[280] H. Maruska and J. Tietjen, "The preparation and properties of vapor-deposited single-crystal GaN," Applied Physics Letters **15**, 327–329 (1969).

[281] R. Jain and H. Maruska, "How it really happened: The history of p-type doping of gallium nitride," Physica Status Solidi (a) **204**, 1970–1976 (2007).

[282] J. Pankove, E. Miller, and J. Berkeyheiser, "GaN blue light-emitting diodes," Journal of Luminescence **5**, 84–86 (1972).

[283] H. Amano, M. Kito, K. Hiramatsu, and I. Akasaki, "P-type conduction in Mg-doped GaN treated with low-energy electron beam irradiation (LEEBI)," Jpn. J. Appl. Phys **28**, L2112–L2114 (1989).

[284] S. Nakamura, T. Mukai, M. Senoh, and N. Iwasa, "Thermal annealing effects on p-type Mg-doped GaN films," Jpn. J. Appl. Phys **31**, 139–142 (1992).

[285] S. Nakamura, T. Mukai, and M. Senoh, "Candela-class high-brightness InGaN/AlGaN double-heterostructure blue-light-emitting diodes," Applied Physics Letters **64**, 1687–1689 (1994).

[286] S. Nakamura, M. Senoh, S. Nagahama, N. Iwasa, T. Yamada, T. Matsushita, H. Kiyoku, and Y. Sugimoto, "InGaN multi-quantum-well-structure laser diodes with cleaved mirror cavity facets," Japanese Journal of Applied Physics **35**, 217–220 (1996).

[287] S. Nakamura, M. Senoh, S. Nagahama, N. Iwasa, T. Yamada, T. Matsushita, Y. Sugimoto, and H. Kiyoku, "Room-temperature continuous-wave operation of InGaN multi-quantum-well structure laser diodes," Applied Physics Letters **69**, 4056 (1996).

[288] L. Dennis and W. Patnode, "Gallium triethyl monoetherate, gallium triethyl, gallium triethyl ammine," Journal of the American Chemical Society **54**, 182–188 (1932).

[289] C. Deatcher, *Growth and characterisation of gallium nitride and indium gallium nitride by MOVPE for photonic applications* (PhD thesis, University of Strathclyde, 2004).

[290] A. Steckl, J. Heikenfeld, D. Lee, M. Garter, C. Baker, Y. Wang, and R. Jones, "Rare-earth-doped GaN: growth, properties, and fabrication of electroluminescent devices," IEEE Journal of Selected Topics in Quantum Electronics **8**, 749–766 (2002).

[291] R. Dahal, C. Ugolini, J. Y. Lin, H. X. Jiang, and J. M. Zavada, "Erbium-doped GaN optical amplifiers operating at 1.54 μm," Applied Physics Letters **95**, 111109 (2009).

[292] E. Dogheche, P. Ruterana, G. Nouet, F. Omnes, and P. Gibart, "Investigation of refractive index and optical propagation loss in gallium nitride based waveguides," Physica Status Solidi (b) **228**, 429–432 (2001).

[293] H. Schenk, E. Feltin, M. Laügt, O. Tottereau, P. Vennéguès, and E. Doghèche, "Realization of waveguiding epitaxial GaN layers on Si by low-pressure metalorganic vapor phase epitaxy," Applied Physics Letters **83**, 5139 (2003).

[294] A. Stolz, E. Cho, E. Dogheche, Y. Androussi, D. Troadec, D. Pavlidis, and D. Decoster, "Optical waveguide loss minimized into gallium nitride based structures grown by metal organic vapor phase epitaxy," Applied Physics Letters **98**, 161903 (2011).

[295] R. Hui, S. Taherion, Y. Wan, J. Li, S. X. Jin, J. Y. Lin, and H. X. Jiang, "GaN-based waveguide devices for long-wavelength optical communications," Appl. Phys. Lett. **82**, 1326–1328 (2003).

[296] R. Hui, Y. Wan, J. Li, S. Jin, J. Lin, and H. Jiang, "III-nitride-based planar lightwave circuits for long wavelength optical communications," IEEE Journal of Quantum Electronics **41**, 100–110 (2005).

[297] O. Skorka, B. Meyler, and J. Salzman, "Propagation loss in GaN-based ridge waveguides," Applied Physics Letters **84**, 3801 (2004).

[298] R. Geiss, A. Chowdhury, C. Staus, H. Ng, S. Park, and J. Han, "Low loss GaN at 1550 nm," Applied Physics Letters **87**, 132107 (2005).

[299] N. Iizuka, K. Kaneko, and N. Suzuki, "Polarization dependent loss in iii-nitride optical waveguides for telecommunication devices," Journal of Applied Physics **99**, 093107 (2006).

[300] A. Lupu, F. Julien, S. Golka, G. Pozzovivo, G. Strasser, E. Baumann, F. Giorgetta, D. Hofstetter, S. Nicolay, M. Mosca *et al.*, "Lattice-matched GaN–InAlN waveguides at λ= 1.55 μm grown by Metal–Organic Vapor Phase Epitaxy," IEEE Photonics Technology Letters **20**, 102–104 (2008).

[301] H. Sodabanlu, J. Yang, T. Tanemura, M. Sugiyama, Y. Shimogaki, and Y. Nakano, "Intersubband absorption saturation in AlN-based waveguide with GaN/AlN multiple quantum wells grown by metalorganic vapor phase epitaxy," Applied Physics Letters **99**, 151102 (2011).

[302] N. A. Sanford, L. H. Robins, A. V. Davydov, A. Shapiro, D. V. Tsvetkov, A. V. Dmitriev, S. Keller, U. K. Mishra, and S. P. DenBaars, "Refractive index study of $Al_xGa_{1-x}N$ films grown on sapphire substrates," J. Appl. Phys. **94**, 2980 –2991 (2003).

[303] E. A. J. Marcatili, "Slab-coupled waveguides," Bell Systems Technical Journal **53**, 645 (1974).

[304] R. Sink, "Cleaved-facet group-iii nitride lasers," Ph.D. thesis, University of California, Santa Barbara (2000).

[305] R. Sink, S. Keller, B. Keller, D. Babić, A. Holmes, D. Kapolnek, S. DenBaars, J. Bowers, X. Wu, and J. Speck, "Cleaved GaN facets by wafer fusion of GaN to InP," Applied Physics Letters **68**, 2147 (1996).

[306] R. Walker, "Simple and accurate loss measurement technique for semiconductor optical waveguides," Electron. Lett. **21**, 581 –583 (1985).

[307] A. De Rossi, V. Ortiz, M. Calligaro, L. Lanco, S. Ducci, V. Berger, and I. Sagnes, "Measuring propagation loss in a multimode semiconductor waveguide," Journal of Applied Physics **97**, 073105 (2005).

[308] M. Thompson, A. Politi, J. Matthews, and J. O'Brien, "Integrated waveguide circuits for optical quantum computing," IET Circuits, Devices & Systems **5**, 94–102 (2011).

[309] I. Moerman, P. Van Daele, and P. Demeester, "A review on fabrication technologies for the monolithic integration of tapers with III-V semiconductor devices," IEEE J. Sel. Top. Quantum Electron. **3**, 1308 –1320 (1997).

[310] L. McKnight, Y. Zhang, I. Watson, E. Gu, S. Calvez, and M. Dawson, "Optimised gan directional couplers with mode converters," in "Frontiers in Optics," (Optical Society of America, 2011).

[311] A. Llobera, I. Salinas, I. Garcés, A. Merlos, and C. Domínguez, "Effect of wall tilt on the optical properties of integrated directional couplers," Opt. Lett. **27**, 601–603 (2002).

[312] H. Choi, C. Jeon, and M. Dawson, "Tapered sidewall dry etching process for GaN and its applications in device fabrication," Journal of Vacuum Science & Technology B: Microelectronics and Nanometer Structures **23**, 99 (2005).

[313] H. Li, S. Przeslak, A. Niskanen, J. Matthews, A. Politi, P. Shadbolt, A. Laing, M. Lobino, M. Thompson, and J. O'Brien, "Reconfigurable controlled two-qubit operation on a quantum photonic chip," New Journal of Physics **13**, 115009 (2011).

[314] L. C. Bassett, F. J. Heremans, C. G. Yale, B. B. Buckley, and D. D. Awschalom, "Electrical tuning of single nitrogen-vacancy center optical transitions enhanced by photoinduced fields," Phys. Rev. Lett. **107**, 266403 (2011).

[315] Y. Park, A. Cook, and H. Wang, "Cavity qed with diamond nanocrystals and silica microspheres," Nano Letters **6**, 2075–2079 (2006).

[316] S. Schietinger, T. Schroder, and O. Benson, "One-by-one coupling of single defect centers in nanodiamonds to high-Q modes of an optical microresonator," Nano Letters **8**, 3911–3915 (2008).

[317] S. Schietinger and O. Benson, "Coupling single nv-centres to high-q whispering gallery modes of a preselected frequency-matched microresonator," Journal of Physics B: Atomic, Molecular and Optical Physics **42**, 114001 (2009).

[318] M. Larsson, K. Dinyari, and H. Wang, "Composite optical microcavity of diamond nanopillar and silica microsphere," Nano Letters **9**, 1447–1450 (2009).

[319] R. Barbour, K. Dinyari, and H. Wang, "A composite microcavity of diamond nanopillar and deformed silica microsphere with enhanced evanescent decay length," Optics Express **18**, 18968–18974 (2010).

[320] M. Barth, S. Schietinger, T. Schröder, T. Aichele, and O. Benson, "Controlled coupling of NV defect centers to plasmonic and photonic nanostructures," Journal of Luminescence **130**, 1628–1634 (2010).

[321] M. Lončar, J. Choy, B. Hausmann, T. Babinec, I. Bulu, P. Maletinsky, M. Khan, and A. Yacoby, "Enhanced single-photon emission from a diamond-silver aperture," Nature Photonics **5**, 738–743 (2011).

[322] M. Gregor, R. Henze, T. Schröder, and O. Benson, "On-demand positioning of a preselected quantum emitter on a fiber-coupled toroidal microresonator," Applied Physics Letters **95**, 153110 (2009).

[323] K. Fu, C. Santori, P. Barclay, I. Aharonovich, S. Prawer, N. Meyer, A. Holm, and R. Beausoleil, "Coupling of nitrogen-vacancy centers in diamond to a GaP waveguide," Applied Physics Letters **93**, 234107 (2008).

[324] P. Barclay, K. Fu, C. Santori, and R. Beausoleil, "Chip-based microcavities coupled to nitrogen-vacancy centers in single crystal diamond," Applied Physics Letters **95**, 191115–191115 (2009).

[325] P. Barclay, K. Fu, C. Santori, A. Faraon, and R. Beausoleil, "Hybrid nanocavities for resonant enhancement of color center emission in diamond," Arxiv preprint arXiv:1105.5137 (2011).

[326] M. Barth, N. Nüsse, B. Löchel, and O. Benson, "Controlled coupling of a single-diamond nanocrystal to a photonic crystal cavity," Optics Letters **34**, 1108–1110 (2009).

[327] J. Wolters, A. Schell, G. Kewes, N. Nusse, M. Schoengen, H. Doscher, T. Hannappel, B. Lochel, M. Barth, and O. Benson, "Enhancement of the zero phonon line emission from a single nitrogen vacancy center in a nanodiamond via coupling to a photonic crystal cavity," Applied Physics Letters **97**, 141108–141108 (2010).

[328] D. Englund, B. Shields, K. Rivoire, F. Hatami, J. Vuckovic, H. Park, and M. Lukin, "Deterministic coupling of a single nitrogen vacancy center to a photonic crystal cavity," Nano Letters (2010).

[329] T. Van der Sar, J. Hagemeier, W. Pfaff, E. Heeres, S. Thon, H. Kim, P. Petroff, T. Oosterkamp, D. Bouwmeester, and R. Hanson, "Deterministic nanoassembly of a coupled quantum emitter–photonic crystal cavity system," Applied Physics Letters **98**, 193103 (2011).

Publications

Papers

Drafted/Submitted

1. **Y. Zhang**, Y. Chen, B. Guilhabert, I. M. Watson, E. Gu, and M. D. Dawson, Diamond lens-like arrays for increasing light collection of colour centre, In preparation.

Accepted/Published

1. Y. Chen, B. Guilhabert, J. Herrnsdorf, **Y. Zhang**, A. R. Mackintosh, R. A. Pethrick, E. Gu, N. Laurand, and M. D. Dawson, Flexible distributed-feedback colloidal quantum dot laser, Applied Physics Letters 99, 241103 (2011).

2. B. R. Patton, P. R. Dolan, F. Grazioso, M. B. Wincott, J. M. Smith, M. L. Markham, D. J. Twitchen, **Y. Zhang**, E. Gu, M. D. Dawson, B. A. Fairchild, A. D. Greentree, and S. Prawer, Optical properties of single crystal diamond microfilms fabricated by ion implantation and lift-off processing, Diamond and Related Materials, 21, 16 (2011).

3. **Y. Zhang**, L. McKnight, E. Engin, I. M. Watson, M. J. Cryan, M. G. Thompson, E. Gu, S. Calvez, J. L. O'Brien, and M. D. Dawson, GaN directional couplers for integrated quantum photonics, Applied Physics Letters, 99, 161119 (2011).

4. **Y. Zhang**, L. McKnight, Z. Tian, S. Calvez, E. Gu, and M. D. Dawson, Large cross-section edge-coupled diamond waveguides, Diamond and Related Materials 20, 564 (2011).

5. M. Wu, Z. Gong, D. Massoubre, **Y. Zhang**, E. Richardson, E. Gu, and M. D. Dawson, Inkjet-printed silver nanoparticle electrodes on GaN-based

micro-structured light-emitting diodes, Applied Physics A: Materials Science & Processing 104, 1003 (2011).

6. Z. Gong, **Y. Zhang**, P. Kelm, I. M. Watson, E. Gu, and M. D. Dawson, InGaN micro-pixellated light-emitting diodes with nano-textured surfaces and modified emission profiles, Applied Physics A: Materials Science & Processing 103, 389 (2011).

7. L. Wang, C. Lu, J. Lu, L. Liu, N. Liu, Y. Chen, **Y. Zhang**, E. Gu, and X. Hu, Influence of carrier screening and band filling effects on efficiency droop of InGaN light emitting diodes, Optics Express 19, 14182 (2011).

8. Y. Chen, J. Herrnsdorf, B. Guilhabert, **Y. Zhang**, I. M. Watson, E. Gu, N. Laurand, and M. D. Dawson, Colloidal quantum dot random laser, Optics Express 19, 2996 (2011).

Conference presentations

Note: presenters underlined.

1. L. McKnight, **Y. Zhang**, I. M. Watson, E. Gu, S. Calvez, and M. D. Dawson, Optimised GaN Directional Couplers with Mode Converters, Frontiers in Optics (FiO) (San Jose, California, 2011), Oral presentation..

2. **Y. Zhang**, L. McKnight, I. M. Watson, E. Gu, S. Calvez, and M. D. Dawson, Large cross section compact GaN directional coupler, IEEE Photonics 2011 (Arlington, Virginia, USA, October 2011), Oral presentation.

3. Y. Chen, J. Herrnsdorf, B. Guilhabert, **Y. Zhang**, A. L. Kanibolotsky, P. J. Skabara, E. Gu, N. Laurand, and M. D. Dawson, Tunable random laser action in a -conjugated polymer-based photonic glass gain medium, IEEE Nano 2011 (Portland, USA, August 2011), Poster presentation.

4. Y. Chen, J. Herrnsdorf, B. Guilhabert, **Y. Zhang**, A. R. Mackintosh, R. A Pethrick, E. Gu, N. Laurand, and M. D. Dawson, Fabrication and optical characterization of a flexible colloidal quantum dot laser, IEEE Nano 2011 (Portland, USA, August 2011), Oral presentation.

5. L. McKnight, **Y. Zhang**, I. M. Watson, E. Gu, S. Calvez, and M. D. Dawson, GaN Waveguides: towards a New Platform for Integrated Quantum

Photonics, The 9th International Conference on Nitride Semiconductors (Glasgow, United Kingdom, July 2011), Poster presentation

6. E. Xie, Z. Chen, P. Edwards, Z. Gong, **Y. Zhang**, Y. Chen, I. Watson, E. Gu, R. Martin, G. Zhang, and M. D. Dawson, Strain relaxation in InGaN/GaN micro-pillars evidenced by high resolution cathodoluminescence spectral mapping, The 9th International Conference on Nitride Semiconductors (Glasgow, United Kingdom, July 2011), Oral presentation.

7. Y. Tao, Z. Chen, Z. Gong, E. Xie, Y. Chen, **Y. Zhang**, J. McKendry, D. Massoubre, E. Gu, and G. Zhang, Size effect on efficiency droop of blue light emitting diode, The 9th International Conference on Nitride Semiconductors (Glasgow, United Kingdom, July 2011), Poster presentation.

8. Y. Chen, B. Guilhabert, J. Herrnsdorf, **Y. Zhang**, A. R. Mackintosh, R. A. Pethrick, N. Laurand and M. D. Dawson, Flexible distributed feedback colloidal quantum dot laser patterned by a submicron grating structure, CLEO/Europe-IQEC 2011 (Munich, Germany, May 2011), Oral presentation.

9. **Y. Zhang**, L. McKnight, S. Calvez, E. Gu, and M. D. Dawson, Large cross-section diamond waveguides, Diamond 2010, (Budapest, Hungary, September 2010), Oral presentation.

10. L. McKnight, **Y. Zhang**, Z. Tian, E. Gu, S. Calvez, and M. Dawson, Large cross-section diamond waveguides, Photon10 Conference (Southampton, United Kingdom, August 2010), Oral presentation.

11. Y. Chen, J. Herrnsdorf, B. Guilhabert, A. Kanibolotsky, **Y. Zhang**, E. Gu, P. Skabara, N. Laurand, and M. Dawson, Random laser action in -conjugated polymer-based photonic glasses system, Photon10 Conference (Southampton, United Kingdom, August 2010), Oral presentation.

12. R. B. Birch, P. Millar, **Y. Zhang**, E. Gu, A. J. Kemp, M. D. Dawson, and D. Burns, Progress Towards Monolithic Microchip Lasers Incorporating Diamond, in Advanced Solid-State Photonics, OSA Technical Digest Series (CD) (Optical Society of America, 2010), paper AWB4.

13. **Y. Zhang**, L. McKnight, S. Calvez, E. Gu, and M. D. Dawson, Photonic microstructures in diamond, Rank Prize Funds Symposium on Diamond Photonics (Storrs Hall, Windermere, United Kingdom, March 2010), Oral presentation.